Florian Olivier Penzel

**Automated measurement of bolometer line of sight alignment and characteristics for application in ITER**

# Automated measurement of bolometer line of sight alignment and characteristics for application in ITER

**Dipl.-Ing. Univ. Florian Olivier Penzel**

*'After all, beauty is in the eye of the beholder,*
*and what we see is scattered light'*

Stover, J. C.

Optical scattering: Measurement and analysis.

Bellingham, Wash: SPIE Press (2012).

**Abstract**

The bolometer diagnostic is used in fusion experiments to derive the total radiated power of the plasma and its spatial distribution. The line of sight (LOS) alignment and characteristic of a bolometer camera is a crucial parameter for the measurement accuracy of the diagnostic as it is an input to the tomographic reconstruction for determining the radiation profile. Therefore, a robot based LOS measurement device has been developed which allows the fully automatic measurement of the two dimensional transmission function of a bolometer camera. It has been used to assess the performance of different collimator prototypes being developed for the future tokamak fusion experiment ITER. Measures to mitigate stray light have been identified and differences from the transmission expected due to the design parameters could be evaluated. Additionally, the measurement device has been integrated in the tokamak ASDEX Upgrade during a maintenance shutdown to measure the LOS alignment and characteristic of the integrated bolometer cameras. As a result, internal camera reflections causing systematically elevated values of the radiation measurements and misalignments of the LOS in the order of 2°-3° from the theoretical alignment have been determined. The misalignments are not a major problem for ASDEX Upgrade, but for ITER the LOS will have to pass through narrow gaps (10-20 mm) between the plasma facing components and therefore have to be aligned about one order of magnitude better than in ASDEX Upgrade. Alternatively a similiar in-situ LOS calibration device will be needed to determine the final bolometer LOS characteristic in ITER.

# Contents

# 1. Introduction

The United Nations are predicting a significant world population growth from 7.2 billion in 2014 to 9.6 billion by 2050 and a further increase to 10.9 billion by 2100 [1]. A growing world population will obviously result in an increasing demand for energy. The U.S. Energy Information Administration predicts, that especially the demand for the electric energy will increase twice as fast and is likely to rise from $E_{2010} = 20.2\,\text{PWh/year}$ in 2010 to $E_{2040} = 39\,\text{PWh/year}$ in 2040 [2].

This increasing energy demand is primarily driven by the developing countries, mainly led by China, India and other Asian countries. Furthermore, the per capita consumption of energy is linked to the development index of a society: The more developed - the higher the energy consumption. Due to the constantly improving standard of living in these countries, the increasing wealth of the global world and the continuous industrialization, the world will need more energy sources then ever before. In the future, electric energy will play an ever greater role. Technological developments such as the use of electric vehicles will introduce a major shift in the overall energy value chain.

The energy consumption of the industrial societies and the developing world nowadays is based on using geologic resources such as fossil fuels, natural gas, oil, coal, plutonium and uranium, which are limited in supply on Earth. They each come with their own environmental problems: The greenhouse effect, pollution during mining and the risks of nuclear fission. Unfortunately, current political conflicts in Ukraine between Russia and the western world reminds the world once more of the local dependence and problems of geologic resources. The search for alternative energy sources due to the need to limit carbon emissions and greenhouse gases because of global warming and climate change issues poses one of the most important challenges of the coming decades.

Renewable energies such as photo-voltaic and wind turbines are on the rise, but will provide no ideal solution due to the inherent unpredictability of the environmental conditions. Currently, an equivalent amount of backup power has to be provided by conventional power plants. The fact, that the European Energy Exchange electricity prices turn negative on a regular basis clearly illustrates that problem. A solution for the storage of this huge amount of energy, which could balance these fluctuations, is not yet in sight. Therefore, a baseload compatible and non-varying source of electricity is needed.

Recreating the power production of the sun - nuclear fusion - on earth, could potentially help the world to solve their future energy needs. When two light atomic nuclei fuse to a heavier nucleus they release a vast amount of energy. Performed in a controlled manner, the thermal energy produced in a fusion reactor can be transported via a cooling water cycle into a turbine generating electrical energy.

The advantages of fusion energy are that no greenhouse gas emissions are released, that it is easily integratable in the existing power grid and that it would take up relatively little space, compared with the amount of energy it can produce. Another important point is, that it has no potential of disastrous consequences for the environment. Fusion has no risk of an uncontrolled chain reaction, it is inherently safe - the atoms only merge if they collide with a sufficient high energy. If an error occurs, the reaction is stopped automatically and no external cooling or additional power is required in the event of system shutdown. Low-level nuclear waste is generated [3], but no long-lived radioactive waste. Using reduced activation ferritic/martensitic (RAFM) steels as structural material, the waste can be recyclable within 100 years [4].

But most importantly, the fusion fuels lithium and deuterium, are more or less virtually limitless available because their supplies on earth correspond to a few million years [5]. Their sources are independent of the political or social situation, thus could prevent future wars over energy sources. The supply of helium, which is currently required as cryogenic coolant during operation, could be possibly more problematic for the large-scale expansion of fusion power plants [6]. The quantity of helium produced by the fusion reaction is not adequate to meet the needs of a future fusion power station. However, sufficient amounts can be extracted from the atmosphere.

Producing commercially competitive energy from nuclear fusion is still a long way off. But in a world ever more dependent on energy it is important to follow all promising options. The future energy mix should be compromised of a mixture of different sources - and fusion could be one of it.

## 1.1   Nuclear fusion

The German physicist and Nobel price laureate Hans Bethe firstly explained in 1939 how nuclear fusion powers the stars [7]. Since the first attempts in the 1950s, there have been world-wide intense efforts to harness the potential of fusion with a steady increase of performance.

The most easily achievable and cost effective nuclear fusion reaction on earth is the fusion of the hydrogen isotopes deuterium ($D$) and tritium ($T$) due to its high cross-section at low ion kinetic energies and the greatest yield of energy per reaction [8]:

$$D + T \longrightarrow {}^{4}He\,(3.517\,\text{MeV}) + n\,(14.069\,\text{MeV}) \tag{1.1}$$
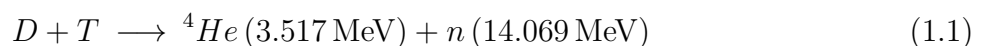
A total of 17.6 MeV of energy is released during each fusion reaction which is about a million times more than classic chemical reactions for burning fossil fuels which are usually in the range of a few eV. The products helium (He) and neutron (n) carry the energy as kinetic energy, distributed according to the inverse of their masses.

The big advantage in fusion is, that deuterium is a naturally occurring isotope, which can be easily extracted by electrolysis from sea water with a natural abundance of $15\,g/m^3$. Tritium, a radioactive isotope with a half-life of 12.32 years is extremely rare on Earth, but can be breeded from widely available lithium in the Earth's crust by exposing it to neutrons: $n + {}^7Li \longrightarrow {}^4He + T + n$. The amount of Tritium extracted from one old laptop battery with the deuterium from a bath tub full of sea water can provide at least enough energy for the lifetime consumption of a single first world citizen [9].

To enable the nuclear fusion reaction, the two hydrogen nuclei $D$ and $T$ have to come very close together, exceeding the repulsive electrostatic force of the Coulomb barrier. The most efficient way to provide the required energy is by confining and heating the particles within a volume until they are ionized and reach the forth state of matter known as plasma. Once the particles have sufficient kinetic energy, respectively are moving at very high velocities, enough to overcome the Coulomb barrier or enable quantum-mechanical tunneling through the barrier, they undergo the nuclear reaction. In stars such as the Sun, the powerful effects of gravity provides the necessary confinement.

On Earth, two leading approaches are under development: The magnetic and the inertial confinement of the plasma. In the magnetically confined plasma strong magnetic fields are used to keep the hot plasma away from the vessel walls [8]. The plasma is heated using ohmic heating, neutral beam injection (NBI) and high frequency waves in the cyclotron resonance frequencies of ions (ICRH) and electrons (ECRH). Inertial confinement fusion compresses a solid pellet target containing a mixture of D and T to high density and temperature by focusing intense laser beams on the particles [10].

The tokamak[1], which confines the plasma in the shape of a torus, is currently the most advanced magnetic device. A toroidal and poloidal field is generating helically wound magnetic field lines which are forming the plasma volume [11] and guiding the plasma particles. JET[2], the largest tokamak in operation, holds the world record in peak fusion power of 16.1 MW [12] with a fusion gain (ratio of produced fusion power to the net input power) of $Q \approx 0.62$ [13].

The work of this thesis has been conducted at the Max Planck Institute of Plasma Physics (IPP) in Garching, near Munich, which is operating tokamaks since 1973. The current experiment ASDEX[3] Upgrade is operating since 1991. ASDEX Upgrade is the largest German fusion experiment being in operation for more than 20 years and has conducted over 30000 experimen-

---

[1]Acronym of the Russian word - "toroidal chamber with axial magnetic field".
[2]JET, the Joint European Torus is an European tokamak experiment.
[3]Acronym of the German word - "Axially Symmetric Divertor Experiment".

tal plasma discharges. The H-Mode, an operational regime with high confinement, has been discovered on the predecessor experiment ASDEX in 1982 [14]. The divertor, an important component usually at the bottom of the experiment which diverts the confined plasma from the direct interaction with the walls and is responsible for exhausting the helium ash, has been developed at IPP as well.

Unfortunately, current experiments are too small to take further big steps in fusion research, but the knowledge has reached the point where it becomes possible of demonstrating breakeven plasma conditions ($Q = 1$). Scaling laws reveal a dependence of the size of the machine with the ability of generating enough power to sustain the fusion reaction itself. This is why a new state of the art tokamak machine is being built in international cooperation: ITER, which is latin for "the way".

ITER will be the world's largest experimental nuclear fusion reactor in the tokamak design. It is currently under construction in Cadarache, France. It is designed to produce $Q \geq 10$, generating up to $500\,\mathrm{MW}$ of output power for $t = 400\,\mathrm{s}$ and thus allowing plasma physics research with a burning plasma heated mainly by fusion reactions rather than by external heating. Therefore, it will be the first machine demonstrating the principle of producing more energy than necessary to initiate the fusion reaction. It is a huge international research and engineering project, 35 nations (27 of which are from the EU) are collaborating and represent more than half the world's population. It's main mission will be *"to demonstrate the scientific and technological feasibility of fusion power"*[1] of a large scale fusion reactor and to test crucial reactor technologies. However, the generated heat will not yet be used to generate electric power. For this purpose, the European community has developed a fusion roadmap within which this step is planned to be shown with a subsequent machine, a power plant prototype known as DEMO.

But despite the continuous advancement of important physical parameters of the plasma, fusion research is still facing many scientific and technological challenges. Therfore, the work to build ITER is distributed worldwide in different tasks and work packages. One part of the tasks of the EU, which holds as host of ITER an overall share of 46%, will be the development of 11 measurement systems.

## 1.2  Diagnostic requirements for ITER

The success of ITER will be judged mainly by two points: Firstly, reaching burning plasma conditions and demonstrate alpha particle heating and secondly, demonstrating long pulse ($t_{pulse} = 1000\,\mathrm{s}$ with $Q \geq 5$) operation in a steady state scenario. The measurement of many physical properties in order to characterize the parameters of the plasma and to study their

---

[1]This is the mission statement of ITER which is widely used.

interactions are mandatory for the operation of any device. ITER will need a large set of approximately 40-50 [15, 16] individual measurement systems respectively diagnostics, as denominated in the fusion community for a measurement system [17]. They will provide machine protection, the advanced plasma control and of course, support key physics studies. For a safe operation of the planned life-cycle of 30 years all ITER parts are challenged with an unprecedented level of complexity and reliability requirements.

A simple up scaling of the current tokamak diagnostic technologies is not possible, new approaches are necessary. Many constraints due to the physical nature of a reactor grade tokamak plasma have to be taken into account. In the following, a brief overview of the numerous challenges arising and significantly impacting the engineering design of diagnostics for ITER will is given:

- **Hostile radiation environment:** High neutron flux of up to $10^{14}$ n/cm²s, a possible radiation displacement damage of 0.1 dpa over the life time [18] and an additional frontal broadband radiant heat flux out of the plasma of several $MW/m^2$ raise the limits for the acceptable materials in the vessel. It has to be considered, that the neutron values are 100.000 times higher than in the currently largest operating experiment, JET [19]. The radiation fluxes have influence on the fatigue or yield strength and can generate microstructure instability of certain materials which therefore call for an oversizing of the design [20]. Worst-case scenarios in a tokamak, such as plasma disruptions and loss of plasma confinement events during off-normal operations, have to be taken into account for the determination of the possible conditions, too [21]. Generally, the whole radiation issue is considered being one of the most challenging of all. Some diagnostics have to rethink all past material choices due to embrittlement of the materials if used under ITER conditions [22].

- **Electromagnetic loads:** In order to keep the generated nuclear heating of auxiliary systems low, it is encouraged to build as small and as highly integrated as possible [23], which is completely opposed to the constraints posed by electromagnetic loads. During certain effects, such as a Vertical Displacement Event, large eddy currents are generated which enforce the construction of rigid and massive structures. Especially diagnostic components have to cope with magnetic fields of up to 8 T. Alternatively, large components with a fixed and unavoidable location, have to be split in slices in order to reduce the forces.

- **Material choices:** Many First Wall (FW) material components in a tokamak suffer under net erosion and sputtering due to the harsh particle fluxes: Charge exchange neutrals, ultraviolet (UV) radiation, deuterium plasma exposure (ion fluence $3 \cdot 10^{20}$ ions/cm²), X-Ray and Gamma radiation are severly affecting certain materials [25]. The materials have to survive multi-scale phenomenons through erosion and re-deposition. Hydrogen and helium implantation is coupled with intense heat fluxes and thermal gradients [26].

Most of them have to be suitable to high vacuum environments, e.g. with respect to impurity concentrations or impurity outgassing down to a vessel pressure of $10^{-7}$ Pa. The safety requirements for material compositions limit the content of certain materials, such as cobalt, in order to limit the activated products [20]. Thus, due to the particular requirements of ITER, bulk materials such as tungsten, beryllium and low-activation steels have to be used.

- **Remote handling compatibility:** All components need to have an extremely high reliability. Firstly due to replacement cost reasons and secondly and most importantly due to the limited access, in particular during the DT campaign of ITER. Human access will be totally prohibited. Consequently, parts requiring modification and maintenance activities have to provide remote handling compatibility and respect standardization policies in order to minimize compatibility issues [27].

- **Enhanced diagnostic specific requirements:** Generally spoken, the more data gathered from diagnostics with a simultaneous increase in accuracy, the better and more reliable physics studies can be conducted. Moreover, the demand for real-time capability of diagnostics in order to integrate and connect them to the plasma control, data access and communication (CODAC) system increased in the past as well [16, 28]. The degree of automation will have to be enhanced. ITER differs also from the maximum possible pulse length compared to existing experiments like JET or ASDEX Upgrade. Therefore, all diagnostics will have to be less susceptible to signal drifts. Water cooling will have to be considered for the first time for certain parts, which are prone to high heat loads. Most of the systems will be even more distributed, components will be located in different locations or even buildings. Some systems will require an unprecedented wide range of responsivity, such as the neutron camera, which will have to cover seven orders of magnitude. Due to the safety requirements during the tritium operation phase, all safety relevant diagnostics will have to think about redundancy or other reliability guaranteeing solutions. More detailed information about measurement requirements for each diagnostic can be found in publications from the ITER Diagnostic Expert Group [15, 29, 30].

Summarized, it can be stated that ITER and its individual components will have to operate in an unprecedented parameter space. However, many developments addressing these problems are already under progress and several technological solutions are already available. From the diagnostics point of view, in particular optical systems will be challenged from these constraints. For example, due to the intense sputtering of internal components, all mirrors close to the plasma will have to be cleaned on a regular basis to maintain their optical throughput. Thus, fully automatic in situ cleaning procedures are under development. Another example is, that optical diagnostics which up to now were using optical fibers directly in the vessel, e.g. spectrometers [31], or surrounding the vessel, e.g. force and strain sensors [32], have to rethink the whole design due to the damage potential of the ionizing radiation environment.

## 1.3   Motivation of the work

The bolometer diagnostic, which performs the spatially resolved measurement of the total radiated power of the plasma in a very broad spectral range is also one of the optical diagnostics which have to be adapted, respectively redeveloped, for this new and complex environment of ITER. Bolometer cameras are distributed around the vessel oriented towards the plasma and perform an integrated measurement along multiple lines of sight (LOS) which allows to calculate tomographic images. Figure 1.1 is showing a perspective CAD picture of a part of the ITER vessel showing a subset of the LOS indicated as black lines. This diagnostic is crucial for ITER because the radiation losses of the plasma are one critical input parameter to determine the overall power balance and thus the fusion gain $Q$. In order to provide reliable data for the Plasma Control System (PCS), the total radiated power will have to be determined within a measurement accuracy of 10% [16, 28].

IPP has a long scientific history in the development, construction, operation and maintenance of bolometers. The metal resistor bolometer (see Chapter 2.1.2), whose design is nowadays state of the art for many fusion experiments world wide and also the type to be used in ITER, has been developed [33] and patented [34] at IPP.

Recently, F4E [1] has awarded IPP a Framework Partnership Agreement[2] (FPA) contract to perform the bolometer development for ITER. The first work packages started in July 2014. Within a duration of 4 years, the diagnostic specifications have to be developed to a prototype level allowing to start the procurement process. Different subsystems will have to be developed, such as the radiation detector itself and the different



**Figure 1.1:** Perspective CAD picture of a part of ITER.

cameras mounted in front of the detector defining the LOS. Test-equipment, electronics, installation instructions and even operation manuals are included in the work packages [35]. In order to be well prepared for the start of this FPA, the German Federal Ministry of Education and Research financed a grant in the framework of which the work of this thesis took place.

The two main challenges for the realization of this measurement system in ITER are the reliability of the detector during alternating thermal loads [36] (see Chapter 2.5) and the development of a bolometer camera design. Aim of this work, is the development of a system for the auto-

---

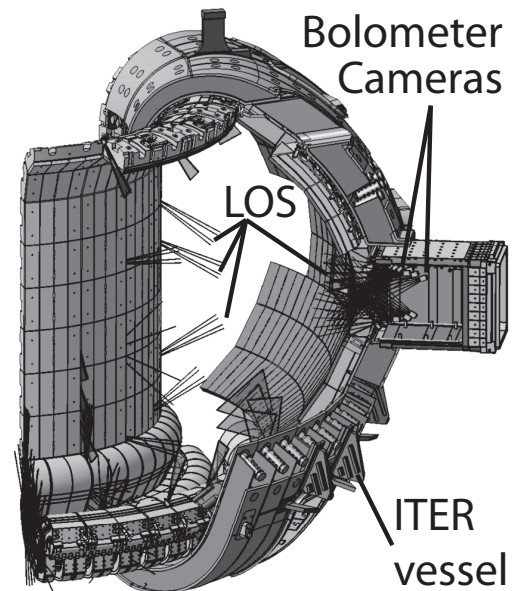[1]Fusion for Energy (F4E): The agency of the European Union responsible for coordinating the European work packages for ITER.

[2]*"The Framework Partnership Agreement (FPA) [..] is a formalized relationship between F4E and the beneficiary [IPP]"* [35]

mated measurement of the bolometer LOS alignment and characteristics in order to verify the camera properties.

## 1.3.1   ITER bolometer collimator developments

The camera in front of the detector plays an important role in determining the accuracy of the overall measurement system. For the correct operation of the tomographic reconstruction algorithms, used to calculate the radiation profile, a detailed knowledge about the LOS characteristics is fundamental. Thereby, the radiation throughput, the orientation and the viewing cone of each LOS in the vessel are the key input parameters.

But due to the unprecedented hostile ITER environment, such as the high neutron and heat flux, all bolometer components will have to be hidden behind large Blanket Modules (BM). The cameras can be distributed around the vessel, some of them will be directly mounted on the inner structure of the Vacuum Vessel (VV) while others will be mounted on the Divertor Cassette Body (DCB) or within the port plugs. However, the main difference to current tokamak experiments will be that the available installation space for the bolometer cameras will be very restricted. A relatively independent installation of the bolometer cameras in the vessel without any shielding, will not be possible anymore. The main challenge for the camera development will be that the bolomter LOS will have to look through the gaps between the BM.

These BMs cover all the internal surfaces of the experimental vessel in order to provide thermal and nuclear shielding of all sensitive components, especially of the superconducting magnets of and e.g. diagnostic components. They are constructed in a very robust and solid way, their typical dimension is $1\,\mathrm{m} \times 1.5\,\mathrm{m} \times 0.5\,\mathrm{m}$ (Height $\times$ Length $\times$ Thickness) with a weight of up to $4.6\,\mathrm{t}$.

Figure 1.2 shows the preliminary camera integration design. Three different views show the position of a four channel bolometer camera mounted on the vessel wall, in between the BMs. The radial view (A) shows a slightly tilted camera with the LOS indicated as diverging black lines from the camera housing, (B) enlarges the area around the camera. In the front view (C) the BMs are displayed transparently to highlight the gap. The last image (D) shows two DCBs, the bolometer is not shown here, but in this case the LOS will be looking trough the gap of the adjacently arranged DCBs.

The latest published configuration [37] projects a nominal BM gap size of $14\,\mathrm{mm}$. Further design considerations [38] propose non-standard toroidal gap sizes of $20-30\,\mathrm{mm}$ at specific areas, e.g. for cut-outs around the LOS. The viewing cones of the LOS will have to fit trough these gaps. However, the LOS cannot be made infinitesimally small, they need to have a certain poloidal and toroidal viewing cone in order to achieve a sufficient signal to noise ratio. Furthermore, it has to be be considered that the LOS will need a certain tolerance to the BM edge in order to compensate possible thermal expansions of the BMs during operation. Thus, a LOS defined

by the BM edges is not desired and would certainly not be reliable or restrict the experimental freedom too much.
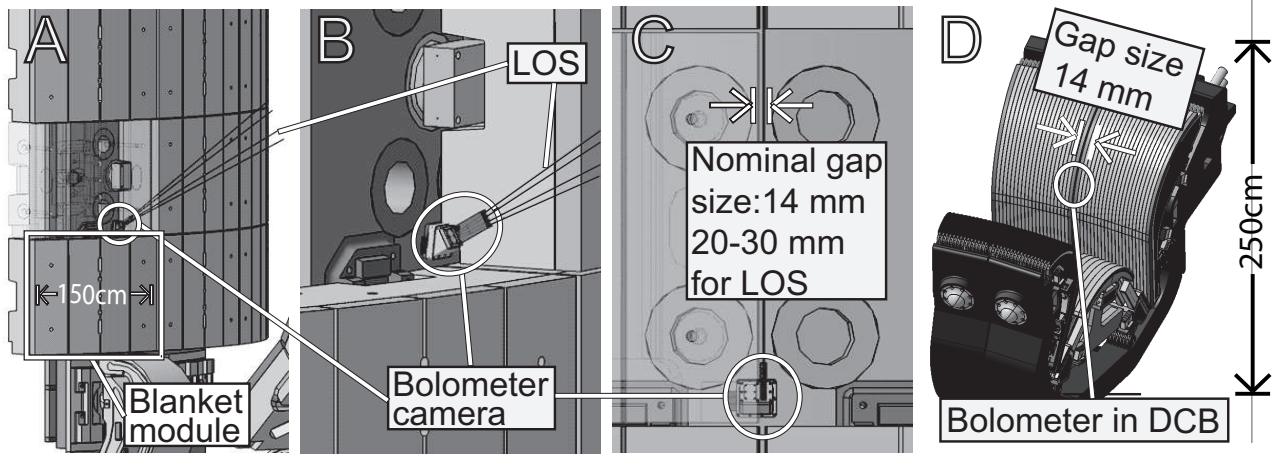


**Figure 1.2:** Three different views of the blanket modules on the inner heat shield: From left to right: Radial view (A), close-up view (B) and front view (C). The Figure on the far right (D) shows two DCBs. The typical dimensions of the ITER blanket modules are $1\,\text{m} \times 1.5\,\text{m} \times 0.5\,\text{m}$ (Height $\times$ Length $\times$ Thickness) with a weight of up to $4.6\,\text{t}$.

Summarizing these constraints, the construction design of the ITER vessel leads to very strict limitations concerning LOS characteristics, in particular with respect to the toroidal viewing cone width. Cameras will have to be developed, providing a very precisely defined LOS. Undesired effects such as stray light and channel cross-talk will have to be minimized as well. The application of noise reduction techniques on a software basis, such as performed with data acquired from a conventional 2D camera, is not possible with bolometric measurements, due to the line integrated operation of the diagnostic. If a certain error of the LOS characteristic is not known, each bolometer channel will accumulate this error, which finally results in falsifying significantly the overall measurement result.

First objective of this work, is to investigate different prototype collimator cameras under development at IPP, in order to check if the intended LOS characteristics can be achieved. Therefore, an automated measurement system allowing to characterize the LOS will developed. Different prototypes will be assessed quantitatively on their qualities in order to develop an optimal design solution for the camera.

### 1.3.2   Proof of concept of an in situ measurement device

But apart from the correct camera properties, its has also to be ensured that the LOS are passing through these BM gaps without being obscured or influenced. A partial occlusion will have a significant impact on the determination of the correct measurement of the radiated power [39]. Moreover, in order to allow the proper localization and quantification of the radiation from the plasma by the tomographic reconstruction algorithms, the final LOS alignment in the vessel

has to be known. In principal, the diagnostic performance is not influenced by the final LOS orientation or characteristic. Deviations from the intended properties and even a shadowing of certain LOS can be accepted. However, these deviations have to be known because they need to be incorporated in the data evaluation.

Finally, this question is not only important for the bolometer diagnostic itself. An incorrectly calibrated diagnostic, which is used for machine protection (e.g. surveying the power limits of the machine), in particular considering the huge amount of energy stored in the ITER plasma, can have serious consequences for the whole experiment [40]. Developing appropriate calibration procedures for similar optical diagnostics, such as the infrared system is considered being a task having the second highest risk regarding the feasibility of the overall diagnostic [41].

Thus, second objective of this work, is to develop an in situ measurement device which shows the technical feasibility and practicability of measuring and calibrating LOS remotely controlled in a tokamak fusion reactor in order to define a basis from which a similar system could be developed for ITER.

## 1.4 Outline of this thesis

This thesis is organized as follows: After introductory remarks and the global motivation of this work, which have been given in Chapter 1, Chapter 2 will review the state of the art knowledge and theoretical background about bolometers. The operation principles of the three common technologies will be presented with a focus on the metal resistor type. Then an insight into the data acquisition and processing is given, referencing and discussing the relevance of certain parameters of a LOS. Possibilities for the construction and realization of a final bolometer camera are given by presenting the design of ASDEX Upgrade and the one planned for ITER.

Chapter 3 is devoted to the developed measurement setup. Firstly, the technological requirements of such a device are analyzed. Next, the final design based on a manipulator, a radiation source and the use of a mobile coordinate measurement machine ensuring the absolute geometrical calibration of the LOS, is presented. The developed software and measurement procedure are explained in detail, along with the calibration process and the achieved measurement uncertainty.

Chapter 4 will discuss the measurement results and is divided in two sections. The first addresses the measurements and optimizations obtained for the ITER bolometer protoype cameras based on a collimator design which have been performed in the laboratory. The influences of certain design choices and the influence of different components of the prototype camera are presented and evaluated. The second subchapter presents the results of the bolometer LOS measurements and geometrical calibrations in the vessel obtained in a first setup of the developed measurement device in ASDEX Upgrade.

Chapter 5 summarizes the information gathered in this thesis. Finally, concluding remarks and an outlook for possible improvements of the measurement setup are given.

# 2. Bolometers and lines of sight in fusion experiments

This chapter describes the fundamentals of the bolometer diagnostic. The first section explains the measurement principle of bolometry and the physics behind it. Different technical designs will be compared, but the main focus will be the functionality of the metal resistor bolometer type, its technical implementation and the digital data acquisition. Finally, in order to calculate the absolute measurements of the total radiated power from the plasma, the necessary equations will be discussed along with presenting the fundamentals of plasma tomography.

A further point of focus will be to explain the technical possibilities to define the beam path of the radiation what we describe here as LOS. Theoretical calculations of the LOS geometry are presented in order to understand the basic LOS shapes. Another section will show the technical implementation of pinhole and collimator camera design, which both will be relevant in this work. At the end of this chapter, the last two sections are used to describe the current development stage of the ASDEX Upgrade and envisaged ITER bolometer diagnostic. All components will be described in the adequate accuracy to understand the technical challenges that need to be solved. The LOS distribution in the ASDEX Upgrade vessel, which has an impact on the in situ measurement procedure, will be presented too.

## 2.1 Bolometers: principles of operation

The Bolometer principle was invented in 1881 by the American physicist and aviation pioneer Samuel Pierpont Langley[1]. He discovered that when combining an electrical thermometer in a Wheatstone bridge, a temperature of less than 1/100.000° and with upgrades even *"differences in temperature amounting to one-billionth of a degree may be detected"*. He was an astronomer and his Biographical Memoir [42] explains that he used it to measure the *"distribution of radiation over the sun's surface and in sun spots"* and to *"determine the lunar energy spectrum and the temperature of the moon"*. The name was derived from the Greek words *"bole"* (beam of light) and "meter" (to measure). During his life time, it was mainly used for astronomy research

---

[1]Samuel Pierpont Langley * August 22, 1834 + February 27, 1906

and even now it is still an important measurement device in this area which is shown by the fact that one of the three on-board instruments on the Herschel Space Observatory is based on the bolometer principle [43]. Nowadays it is widely used in many other scientific areas.

In particle physics it is operated as a particle detector system at cryogenic temperatures to detect Weakly Interacting Massive particles or Dark Matter particles. Microbolometer interconnected to large arrays are used in industry applications as fully portable tools: Thermographic cameras are using the same technique to visualize the energy loss e.g. from buildings in order to detect thermal bridges. The spectral range of the detector can be adapted, so that the bolometer principle is also used on the Z-Machine at the Sandia National Laboratories measuring the absolute x-ray fluence and flux [44]. The requirements may vary significantly from industry application to space research. For bolometers in controlled nuclear fusion research following items have to be respected.

Objective of the bolometers in fusion devices are to measure the total radiated power from the fusion plasma with a broad-band detector operating in the range from near IR to soft x-ray. The operational requirements of a detector being directly in the vessel are very demanding [45]: They will have to survive in radioactive contaminated environment and be resistant to radiation damage from neutrons. The detector has to be insensitive to rapid temperature changes of the environment and peak temperatures of 150° (e.g. for ASDEX Upgrade) and should not be influenced by strong electromagnetic fields and pressure changes. Moreover, the whole system together with the mounting support has to be highly reliable, capable of bearing great loads in day-to-day operations due to the difficulty of performing repairs, remotely or during shut-down.

### 2.1.1 Bolometry in fusion experiments

Bolometry has been used as a fusion research diagnostic for over 40 years [46]. In the beginning, the bolometers were simply made from a thick film flake thermistor with definitely poorer properties then nowadays.

For the application in fusion research, three main concepts, which have been established on large-scale fusion type devices in the past, are presented. The concepts of ferroelectric [47], semiconductor [48], thermistor [46] and thermopiles [49] bolometer type are not discussed here since they are currently not applied in fusion devices. The ones in use are:

- The metal resistor bolometer: This type was described by Langley in 1881 and is nowadays still the most common design. The state of the art implementation of this type is composed of three different layers manufactured via thin-film technology: A metal resistor, an electrically insulating but thermally conducting layer and an absorption layer (see figure 2.1 in the next section). The temperature-driven change in the resistor layer is used to determine the total deposited energy in the absorption layer. This concept was developed by Mueller [33] and Mast [50] at JET and ASDEX in the 90', it resulted in a

patent [34] and was later upgraded to an array construction [51] for multiple channels in a single detector.

- The Absolute eXtreme UltraViolet (AXUV) photo diode bolometer: The most recent principle is based on semiconductor photo diodes [52, 53] using the photoelectric effect. Photo diodes convert photons of sufficient energy ($h \cdot v > E_g$) into either current or voltage using the inner photoelectric effect. They are inexpensive [54], which allows a higher LOS density compared to the metal resistor type. However, they are not radiation hardened and they cannot survive high neutron and $\gamma$-radiation fluxes and suffer degradation, which makes them unsuitable for the use on a DT machine such as ITER. In addition, because of their limited wavelength range and nonlinear sensitivity, they cannot be used to measure the absolutely calibrated radiated power in the whole emitted frequency range from the plasma. However, they are highly appreciated as a complementary diagnostic, due to their direct response to the incident power and superior time resolution of up to 500 ns [55].

- The Infrared Imaging Video Bolometer (IRVB): This method is using an infrared camera to monitor the temperature of the back of a segmented foil placed behind a pinhole. Firstly, Ingraham developed an "Infrared calorimeter for time-resolved plasma energy flux measurement" [56], which Wurden [57] improved by applying a segmented absorber to derive multiple LOS and using state of the art infrared (IR) cameras. The concept is now extensively tested [58], a calibration technique was recently developed [59] at the Large Helical Device (LHD), Japan. The concept offers excellent spatial and temporal resolution. With shielding, it could survive harsh radiation conditions. Problematic for this type is identical to the photo diode concept: This type cannot be used for the absolute calibrated measure of radiated power because of the non-linear spectral response of the thin foil [54].

The metal resistor bolometer is considered as being the *"classical bolometer type"* [57] in the fusion world, because it is the only type which is expected to meet all the requirements specified above for parameters of a DT fusion machine such as ITER [60]. All the other types can only act as a support technology [61], having individual advantages compared to the metal resistor bolometer, but cannot completely replace it.

### 2.1.2 Metal resistor bolometer

The metal resistor bolometer used here, is referred to as the *"ASDEX-type"* because they have been originally developed for the ASDEX tokamak [50], the tokamak experiment prior to ASDEX Upgrade. Another common expression is the *"foil bolometry"* [55] to distinguish it from other bolometer types. In figure 2.1 a schematic diagram of the most important parts of the metal resistor bolometer can be seen.
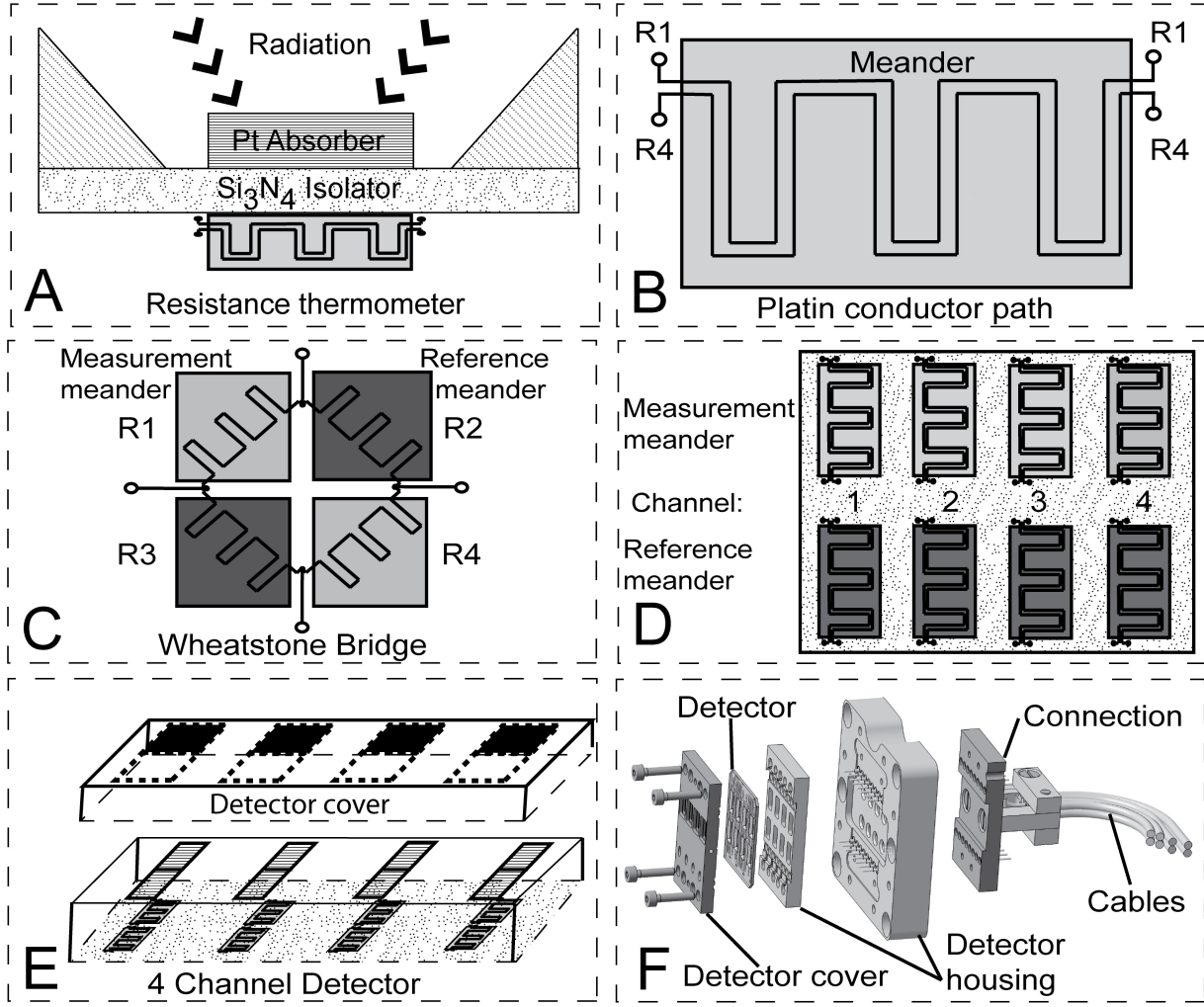
**Figure 2.1:** Schematic drawing of the metal resistor bolometer parts: A) Detector in a side-view. B) Meander shape of platinum conductor path. C) Two detectors connected in a Wheatstone Bridge. D) Four channel detector in a top view. E) Four channel detector and detector cover. F) Full ITER prototype bolometer with detector housing and cable connection.

A metal resistor bolometer is made from three layers which are manufactured using a combination of photolithographic and etching processes, vapor deposition and sputtering such as for the fabricating of integrated circuits (A). Silicon nitride ($Si_3N_4$), a chemically relatively inert material, is used as a substrate. An absorber material (Pt) is deposited on top of the substrate. Just below and on the identical area, two metal resistors in a thin meander shape consisting of two interwoven passing Pt conductor paths ($R_1$,$R_4$) are applied (B). The substrate layer in the middle acts as an electrical but not thermal insulator.

When incoming electromagnetic radiation incidents on the absorption layer, it is absorbed and transformed into thermal energy, resulting in heating up the whole detector. The resistance change ($R_1$, $R_4$) is then converted into a voltage or current signal which is measured to deduce the radiated power. Combined with a second and identical meander shape (C), a Wheatstone bridge [62] ($R_1, R_2, R_3, R_4$) can be realized corresponding to a single bolometer channel.

Thus, one resistance thermometer can act as a reference absorber $(R_2, R_3)$ to compensate for externally induced temperature drifts or nuclear heating (by neutron absorption). The standard detector design has four channels, which in turn consist of eight identical meander shapes (D). The four channel detector is mounted inside a detector housing which shields one resistance thermometer from the plasma. In order to dissipate the incoming thermal energy, the whole detector is integrated in a detector housing, acting as a heat sink. To complete the whole measurement system, the detector housing is screwed together with a custom cable connection.

The temporal evolution of the power absorbed by the detector can be calculated from the bolometer bridge voltage $\delta U_{bolo}$ by the following differential equation [50]:

$$P_{rad}(t) = \kappa_{heat} \left( \frac{d\delta U_{bolo}}{dt} + \frac{\delta U_{bolo}(t)}{\tau_{detc}} \right) \tag{2.1}$$

$\kappa_{heat}$ is the effective heat capacity and $\tau_{detc}$ the cooling time constant of the detector foil, which is again determined by the physical parameters of the whole setup, such as thickness, heat capacity and heat transmission coefficient of the materials used. They can influence the sensitivity and response time of the bolometer and can be improved by using different absorption and substrate materials. Here, different inert metals such as platinum (Pt) or gold (Au) for the absorber are used. But usually the choices are limited by other constraints, such as radiation hardness [63].

Furthermore, the thickness of the absorption layer determines the highest photon energy from the plasma, which still can be absorbed. The typical necessary thickness of this layer is physically fixed; For ASDEX Upgrade it is in the range of $\sim 4\,\mu m$ to achieve a sensitivity for up to 8 keV photons, for ITER a thickness of $\sim 12\,\mu m$ will be needed, due to the higher photon energies up to 25 keV [60]. The membrane thickness should be kept as small as possible in order to avoid increasing the overall time response of the detector. The thinner and smaller the membrane, the better the sensitivity. Usually, the membrane thickness is also determined by engineering constraints of the manufacturing process and the required mechanical robustness. The thickness of the resistive layer on the bottom is determined by the necessary meander resistance in the range of $0.5 - 1.2\,k\Omega$ in order to achieve a sufficient signal-to-noise ratio. The typical dimension of each absorber (A) is $1.5 \times 4\,mm$ and included in a four channel detector (D) it reaches a size of $2 \times 3\,cm$. At ASDEX Upgrade the currently achieved effective time resolution in the best case is 2 ms and taking into account electromagnetic noise at the worst case 30 ms [55].

The metal resistor bolometer in the design presented above is used in many fusion devices. It is operating at the largest fusion device of the world JET [64], it has been recently integrated in the new Korean tokamak K-STAR [65] and Chinese tokamak EAST [66] and will be used in the most modern Stellarator W7-X [67], which is currently under construction.

## 2.1.3  Data acquisition and absolute calibration procedure

The data acquisition (DAQ) at ASDEX Upgrade is based on a LabVIEW application using an FPGA connected to electronics developed in house[45]. A tokamak environment is a very noisy environment for all kinds of electronic circuits due to its numerous sources of external electromagnetic (EM) interferences. Thus, under real operation conditions, a few issues have to be resolved.

The DAQ applies a $5 - 10$ V AC peak-to-peak square wave voltage at $2.5$ kHz to the bolometer full bridge. This has the advantage of allowing high gains of the operational amplifiers in order to reduce possible interference signals. Cables with a length of up to $40$ m are used to shield the bolometer electronics from neutrons and other EM noise. However, this introduces an additive cable series capacity, inductance and resistance in the measurement circuit, which have to be compensated. The series inductance can be neglected, due to the high carrier frequency, but the signal cables and current supply lines between amplifiers and detectors have to be taken into account in the calculation.

Furthermore, before each plasma discharge, the cooling time constant $\tau_{detc}$ and the effective heat capacity $\kappa_{heat}$ have to be determined for each bolometer detector as the parameters depend significantly on the environmental conditions and which vary over time. Moreover, due to the manufacturing process, the variations of the foil thickness can be up to $\Delta T_{abs} = 2.5$ μm for an absorber nominal thickness of $T_{nominal} = 12.5$ μm [68]. This corresponds to a variation of $20\%$ and thus requires at least one calibration.

The calibration is done by short-circuiting two resistors of the full bridge, so that only the reference or measurement detector can be measured individually. Then, the detector area is heated with a direct current (DC) of known power. Aim is to use as little power as possible to avoid overheating of the detector and because of the temperature dependence of the parameters, while maximizing the Signal to Noise (S/N) ratio. At ASDEX Upgrade $P_{calib} = 5$ mW is considered being a good trade-off. The current is abruptly changed and from the voltage decay the cooling time constant $\tau_{detc}$ and the heat capacity $\kappa_{heat}$ can be derived, respectively fitted. The DAQ electronics are implemented in parallel so that all calibrations can be conducted simultaneously. More details of the DAQ electronics, exemplary for W7-AS [45] or ASDEX Upgrade [69] can be found elsewhere.

Taking all these constraints from the practical use into account, the equation 2.1has to be extended. The absorbed power from the bolometer $P_{rad}(t)$ can be derived from the unbalanced bolometer full bridge $U_{bolo}(t)$ with the following equation [45]:

$$P_{rad} = \frac{2}{U_{src}}(R_{md} + 2R_{cab})\kappa_{heat}\sqrt{\alpha}\left[\tau(\frac{\partial U_{bolo}}{\partial t} + U_{bolo}(1 - \frac{U_{src}^2\beta}{4\kappa(R_{md} + R_{cab})^2})\right] \quad (2.2)$$

with $\alpha$ and $\beta$ :

$$\alpha = 1 + (\omega_{src} C_{cab} (R_{md} + R_{cab}))^2 \tag{2.3}$$

$$\beta = \frac{1 - (\omega_{src} C_{cab} R_{md})^2 + (\omega_{src} C_{cab} R_{cab})^2}{1 + (\omega_{src} C_{cab} (R_{md} + R_{cab}))^2} \tag{2.4}$$

The parameters are: $U_{src}$ is the amplitude of the AC source voltage, $\omega_{src}$ is the frequency of the AC voltage, $U_{bolo}$ the bolometer bridge voltage (the measurement signal), $R_{md}$ is the meander resistance ($\approx 1.2\,\text{k}\Omega$), $R_{cab}$ the resistance of the connecting cables and $C_{cab}$ the capacity of the connecting cables.
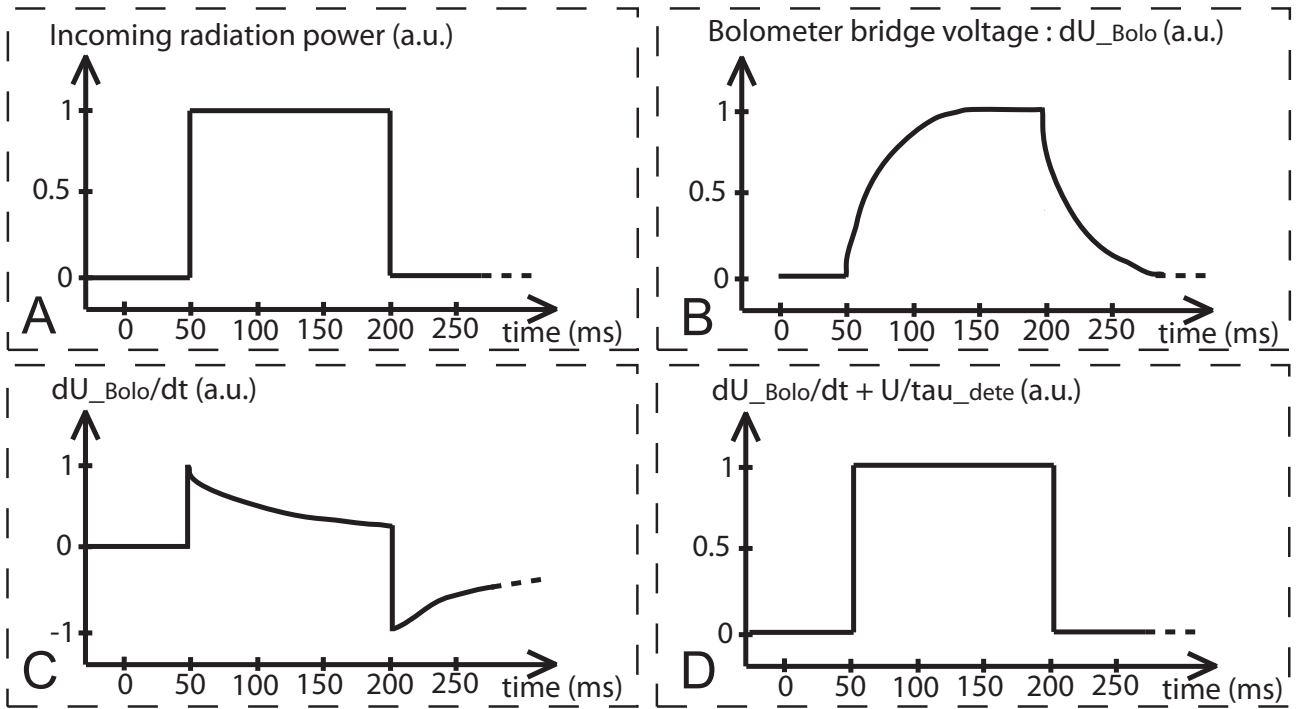


**Figure 2.2:** Internal signals of the DAQ [33]: (A) A step function of incident radiated power $P_{icd}$. (B) The resulting bolometer bridge voltage $U_{bolo}$. (C) The time derivative of the voltage $\frac{\partial U_{bolo}}{\partial t}$. (D) Corrected term with cooling time constant $\frac{d\delta U_{bolo}}{dt} + \frac{\delta U_{bolo}(t)}{\tau_{detc}}$.

Figure 2.2 shows a schematic drawing of the relevant signals from which the main properties of the metal resistor bolometer equation 2.1 can be derived. All signals are shown as normalized values. Subfigure A shows a step function of incident power on the detector of the duration $t_{pow} = 200\,\text{ms}$. The response of the bolometer bridge voltage $U_{bolo}$ acts like a resistor-capacitor circuit (RC circuit) and shows exponential increase to the maximum value. Here, shown for a thermal time constant of $\tau_{dete} \approx 25\,\text{ms}$ (Time to reach 63.2% of its final value for a step response). To determine the power $P_{rad}$, the energy per time unit has to be calculated, which is shown by applying the derivative, see Subfigure C. Finally, corrected with the cooling time constant $\tau_{dete}$ a measure of the absorbed power can be calculated (Subfigure D).

Work is in progress for further optimizing the DAQ and improving the algorithm: For steady-state operational scenarios in ITER ($\approx 30\,\text{min}$ projected discharge times) the constant heating

by the current flow during a measurement will have to be compensated. At ASDEX Upgrade this corresponds only to an ohmic heating of $P_{\Omega-heat} = 83\,\text{mW}$ due to the considerably short discharge times of $10\,\text{s}$ [45]. One possibility is to regularly recalibrate the heat capacity $\kappa_{heat}$ and cooling time constant $\tau_{detc}$, while closing the bolometer aperture with a shutter [70]. Alternatively, the change of the constants can be compensated in real-time by using the bridge current $I_{bolo}$ as a measure for the bolometer holder temperature [71].

Another issue is the influence of the neutral gas pressure on the detector. It has been shown, that pressure changes can have a significant influence ($\approx 12\%$) on the meander resistance due to the strain-gauge effect. However, the strain-gauge factor of the detector can be obtained experimentally and then compensated with a parallel monitoring of the pressure change [72].

## 2.1.4   Application of bolometric measurement data

Bolometers are considered being an *"old diagnostic"* [58] because they are one of the key diagnostics for the machine protection and used for basic control of the experiment [16]. The acquired measurements of the radiated power distribution of the plasma is fundamental for many studies. Typically, the data is used to determine the absolutely calibrated values of radiation losses of certain plasma effects. Understanding the energy loss mechanisms of a tokamak plasma is crucial in order to develop techniques to control them [48]. The experiment ISTTOK[1] is e.g. using bolometric tomography to control the plasma position during a plasma current reversal [73]. Study of ion and electron transport processes [74] and the behavior of plasma detachment[2] is examined [75]. In order to understand plasma instabilities, the diagnostic is mentioned in recent studies as *'well suited tool for detecting and localizing slow and fast events of the plasma'* [55]. Moreover, it provides data to understand MARFEs[3], which play an important role in determining the fueling and density limits of a tokamak experiment [74].

ITER is planned to operate in the so-called Type I ELMy H-mode. This mode is considered being a high performing and stationary scenario with high plasma density, good energy confinement and suited for DT operation in ITER [8]. However, many physical process of this mode have not yet been fully understood and the bolometer diagnostic is playing an important role trying to answer some of these open questions. For instance, the tomographic reconstructed profiles of the radiated power can help to track the diffusion of impurities [76] or analyze the confinement of energetic particles such as fusion born alpha particles during this special mode.

---

[1]ISTTOK is a small Portugese limiter tokamak operating since 1990.

[2]Plasma detachment is a regime where the plasma becomes completely detached (separated) from any solid surface, such as the divertor [8].

[3]A MARFE (multifaceted asymmetric radiation from the edge) is a plasma phenomenon characterized by greatly increased radiation and density fluctuations at the inner major radius edge of the plasma [8].

Furthermore, knowledge about the radiation distribution is used to evaluate the radiation energy from different plasma instabilities, such as type-I Edge Localized Modes (ELM[1]) and thermal quenches[2]. Usually, these instabilities are striking and damaging the plasma facing components [77] which leads to target erosion [78]. ELM studys are considered being very important for ITER, since they impact the global confinement and fusion performance [79]. The plasma radiation variations during these events are considered as important to understand [80]. In particular studies concerning machine protection, for e.g. analyzing the maximum heat load which occurs during plasma disruptions [81] the bolometer data is fundamental. Finally, an essential question for ITER or even for a future fusion power plant are questions concerning the extension of component lifetimes which primarily are influenced by the amount of absorbed radiation power.

### 2.1.5   Tomography

Tomography is an imaging method used to calculate a two dimensional image of an object, referred to as a *'tomogram'*, from data gathered from a measurement system from multiple directions, usually in a non-invasive way. Typically a camera is moved around the object to be observed but this is only possible if the object is not changing in the measurement period. Alternatively numerous cameras containing multiple detectors (LOS) are placed around it, as in a fusion experiment, with the advantage of having temporally resolved measurements.

From the data acquired and the knowledge of the LOS distribution (see figure 2.3 for the LOS distribution in ASDEX Upgrade) and characteristic, a cross-sectional image of the object can be calculated by applying different mathematical procedures called tomographic reconstruction, inversion or deconvolution algorithms. Multiple images obtained in different planes can even be merged to generate a three-dimensional image of that structure. Different physical phenomenons, such as electromagnetic radiation from different energy levels and particles (e.g. electrons, ions) can be used to observe that object.

In fusion devices, tomography is performed for a multiplicity of wavelengths and particle energy: The soft X-ray range is measured (e.g. for monitoring thermal instabilities or plasma disruptions), $\gamma$-ray tomography is performed (e.g. for measurement of radial distribution of fast ions) and neutron tomography (e.g. for monitoring the neutron-flux of the fusion reaction). Finally, relevant for this work, tomography of bolometric data in order to determine the spatial profile of the radiated power.

The mathematical challenge of the tomographic reconstruction lies in the fact that *'many nonlocal measurements, such as line integrals [have to be] processed mathematically to estimate*

---

[1]ELMs are unwanted plasma edge instability events which consist of repetitive (periodically but irregular) bursts of the edge plasma driven by the pressure and current

[2]A thermal quench is a fast release of heat energy caused by certain plasma instabilities [8].

*local physical quantities'* [82]. The two dimensional Radon transform[1], which represents the data obtained as the output of a tomographic measurement, has to be solved:

$$f_i(r,\vartheta) = \int_{-\infty}^{\infty} \int_{-\infty}^{\infty} g(x,y)\delta(x\cos\vartheta + y\sin\vartheta - r)\,dx\,dy \qquad (2.5)$$

$f_i(r,\vartheta)$ are the measurements obtained by a multitude of LOS ($i$) viewing the plasma from the projection angle $\vartheta$. The delta-distribution ($\delta$-funktion) represents the (infinitely thin) LOS which are convoluted with the radiation profile $g(x,y)$. The value $r$ is the distance (radius) between the LOS and the origin of the X-Y coordinate system (CS) in the center of the experiment. The angle $\vartheta$ is between $r$ pointing to the LOS and the X-Axis. More advanced tomographic algorithms respect the geometric properties of a real detection systems, but these methical details are not in the scope of this thesis (see the references cited in this section).

For most tomographic applications in a tokamak toroidal symmetry is assumed, which means that the *"diagnosed quantity [...] does not vary in the direction perpendicular to the reconstruction plane over a thickness that is measured by the 3D detection system"* [83]. Therefore the measured quantity in one poloidal cross-section can be used to project the radiation profile on the whole vessel and it has the advantage that the cameras can be spread toroidally. However, in order to avoid an excessive amount of different cables in the vessel to increase the maintenance complexity, usually most of the detectors are placed very close to each other.

Figure 2.3 shows two poloidal cross-section drawings of ASDEX Upgrade. Subfigure A shows the orientation of LOS from two cameras crossing the vessel from the right. The colors are representing the integrated power density along the LOS (in MW/m$^2$). Subfigure B shows the calculated two dimensional radiation profile, the colors are representing here the power density projected on the whole tokamak vessel (in MW/m$^3$). Numerous numerical implementations of the Radon transform exist, at ASDEX Upgrade a pixel based approach is used, therefore small rectangular 'pixels' can be identified in the figure.

A strong radiation peak left of the X-point[2] can be identified, the red line indicates the magnetic flux surface which are almost intersecting (X). The orange lines represent the contour lines of unwanted artifacts having a negative emissivity. Obviously this is physically impossible, however, a frequent part of the result. Here, it can serve as an examples of the uncertainty of these reconstructions. Usually, the quality and reliability of the results depend strongly on the manual assessment of the diagnostic operator.

These artifacts can hardly be corrected completely because from a mathematically point of view the solution is classified as an ill-based problem - its has not no unique solution. A simplified explanation using the pixel based approach is that there are more pixels then available LOS.

---

[1]The Radon transform is a generalization of the Abel transform which is a projection of $f_i(r)$ along only one particular dimension.

[2]The X-point is the saddle point for the flux function in a tokamak. The magnetic induction field is zero, thus forming a X in the divertor [8].

Additionally, three other issues are amplifying the problem: Firstly, the data contains always noise. Secondly, some areas are having a limited LOS coverage. Thirdly, no detailed knowledge of the LOS characteristics is available.
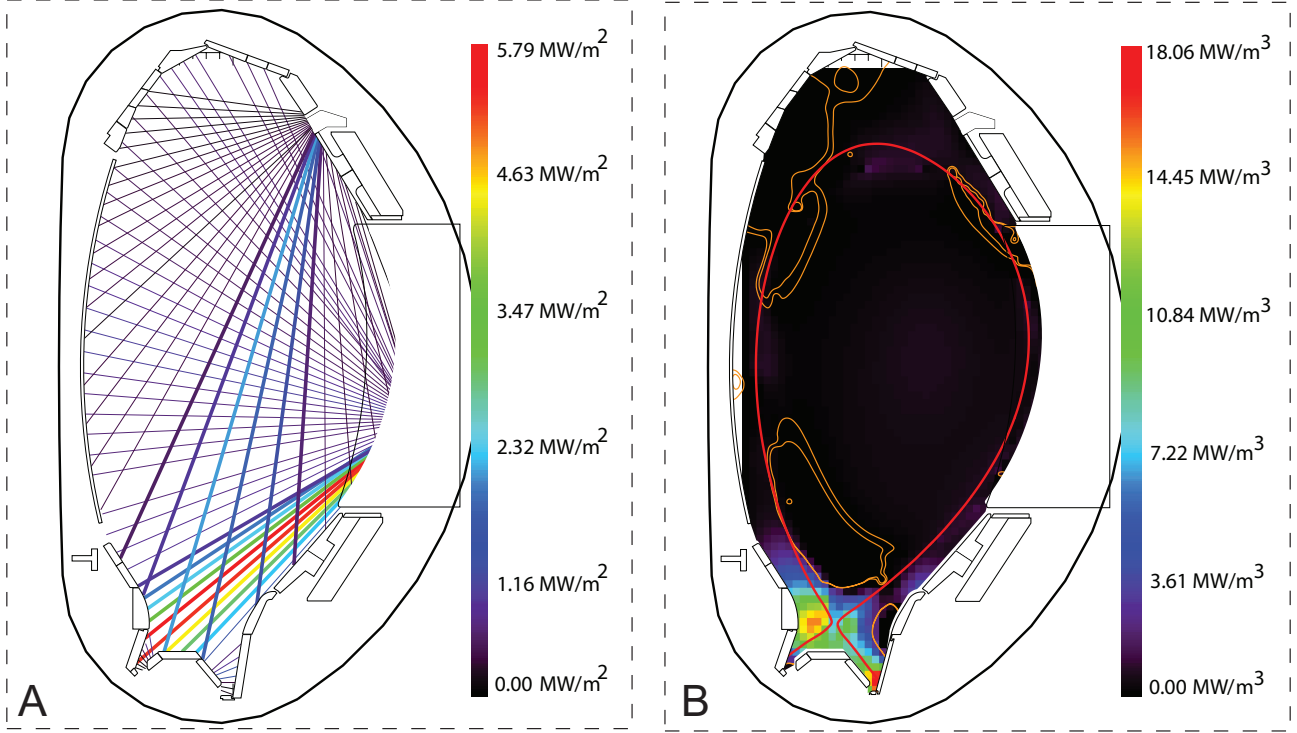


**Figure 2.3:** Subfigure A shows the LOS of two cameras, the colors represent the power density along the LOS. Subfigure B shows the two dimensional radiation profile, the colors represent the power density projected on the whole tokamak. The orange lines represent regions with artifacts, the red line the magnetic flux surface. Strong radiation around the X-point[2] can be identified. ASDEX Upgrade Shot # 30506, t = 4 s.

This means that the equations cannot be solved correctly without additional information. By adding appropriate conditions, based on the specific physical behaviour of the measured radiation profile, e.g for ASDEX Upgrade having a D-shaped plasma, conditions such as radiation gradients in relation to the flux surfaces and the geometry of the magnetic equilibrium are needed to reduced the complexity of the calculation [55]. In the past computational power was a problem for the calculation. Nowadays, using parallel computing, even a real time tomography calculation can be performed [69].

Typically, reconstruction algorithms are "trained" with samples of known radiation profiles ("phantoms") and then compared with the results in order to asses the quality of that guess and to improve the internal parameters, such as the weighting or even the exclusion of certain LOS. Different computer-assisted techniques [84] are used at ASDEX Upgrade. In this way, it is possible to optimize the reconstruction to a particular plasma behaviour but this still proves to be very unstable with respect to noisy data.

## 2.2   Lines of sight

A LOS normally refers to a straight, infinitely thin and unobstructed line between an observer and an object. However, when this term is used in applied geometric optics, LOS have a certain shape, width, height, divergence, and are limited by several engineering requirements.

At first, the constraints and goals of an optimal bolometer LOS distribution in the environment of a tokamak is presented. Next, the quantities that characterize the LOS shape of a bolometric systems, such as the finite detector size and the finite sizes of bounding apertures are explained. Finally, in order to allow the comparison of a theoretical LOS transmission with a measured transmission (see the results in Chapter 4), a simplified theoretical model for the calculation of the LOS characteristics is provided.

### 2.2.1   Optimal distribution

Several general constraints and requirements for the distribution of the LOS in a tokamak should be taken into account:

- The interesting and important areas in a tokamak, from the radiation physics perspective are: X-point, divertor, plasma edge and the bulk plasma region of the vessel. Aim is to achieve a relatively even distribution of the LOS in order to avoid irregular spatial sampling because this can cause problems for the tomographic algorithms.

- Toroidal symmetry is still an assumption in order to simplify the calculations. Due to toroidal asymmetric perturbations , e.g. from toroidally localized gas or pellet injection outlets[1] in the vessel or localized plasma behaviour, e.g. from field-aligned post-ELM filaments [85], it should be favored to align as many LOS as possible in one poloidal cross-section in order to minimize errors enduced by these effects.

- The LOS from different cameras which have the same field of view should be positioned interlaced. If an individual camera fails, it results only in a loss of resolution instead of the complete blindness in a certain area [38].

- Having at least one camera placed on the top of the vessel viewing the full vertical cross-section has the advantage that the total radiated power from the plasma ($P_{rad}$) can be calculated in a simple way, without performing a tomographic reconstruction calculation. The precondition is that the camera must view the vessel vertically in order to have a reference for the circular plasma volume of the tokamak.

---

[1]Pellet injection is an effective method for deep fueling of the fusion fuel by centrifugal acceleration [13].

- In order to improve the measurement accuracy, high radiation areas should be measured separately from areas with low radiation in order to be able to optimize the light yield of each camera.

- It is advantageous having a couple of LOS which are viewing the plasma from opposite directions or are overlapping in order to inspect the data for correctness [82]. Error sources that mainly affect only one side of the vessel, such as the localized plasma heating with ECRH can then be filtered out or identified.

As a rule, the higher the amount of LOS the quicker and better convergence of the tomographic reconstruction algorithms, which leads to a higher resolution, measurement accuracy and lower noise. It must be noted that areas having no intersected LOS, can not be spatially resolved. Typically, the overall cost of the system limits the final LOS number. Numerical simulations can be conducted in order to optimize and validate the LOS positions, distribution and theoretical reconstruction quality with a series of phantom radiation profiles. Moreover, LOS deviations from their expected orientation can be simulated to qualify their impact on the reconstruction [86] or Gaussian noise can be added to the signals, allowing filter testing in order to minimize undesirable artifacts [73].

### 2.2.2   Optimal LOS shape: trapezoidal or cone

Principally, two different one dimensional LOS shapes can be distinguished for a pinhole camera with a single detector, respectively one LOS: The trapezoidal and the cone (or triangular) beam shape. Figure 2.4 shows three schematics of the geometric reproduction of these two possible transmission functions. The transmission is normalized (a.u.), aperture width and detector width are indicated. The values in these figures are only provided as typical examples, bolometer camera and transmission are not to scale.
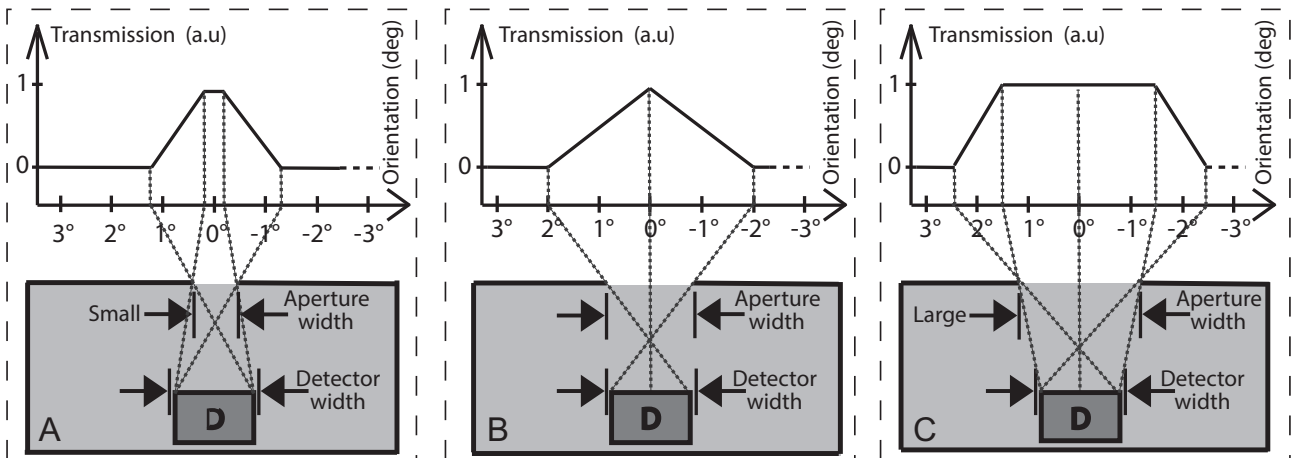


**Figure 2.4:** Geometric reproduction of the transmission function of three different detector - aperture aspect ratios. For a detector width smaller (A) and larger (C) than the aperture width the transmission is trapezoidal, for a detector having the same width as the aperture, the transmission is triangular (B). Bolometer camera and components are not to scale.

Here, aperture opening and detector are supposed to be arranged vertically, one above the other, and parallel to each other. Due to this symmetrical design, the corresponding transmission functions are also symmetric. The dotted lines highlight the significant locations of camera and transmission function. The transmission function results from a projection of the detector and aperture edge points on a horizontal plane. In this figure the dotted lines are projected on the orientation axis (X-Axis) and then elongated to their transmission value (Y-Axis).

In Subfigure A, the aperture width is smaller than the detector width. The first radiation beam can incident for an alignment of $1.3°$ (perpendicular to the detector). The maximum of the LOS will be reached as soon the entire width of the entering beam covers the detector. Assuming a constant measurement across the detector surface, the transmission remains at a constant level, from $0.2°$ to $-0.2°$, and decreases on the other side equally and reaches zero as as soon as the last ray of the incident beam left the edge of the detector. This shape is then denominated as trapezoidal.

The more the aperture size increases the closer the signal rise and fall come closer to each other, which can be seen in Subfigure B. For the equal width of aperture and detector, only with an exact vertical alignment of incident radiation towards the detector the maximum signal can be reached. Then, the transmission has a triangular shape. For an aperture width larger than the detector width, the signal becomes trapezoidal again, see Subfigure C. Due to engineering constraints and mostly due the fact that a certain S/N ratio can only be reached with a certain detector size, usually the detector - aperture aspect ratios in Subfigure B and C are relevant for bolometer cameras.

Once the amount and distribution of the LOS have been determined (compare previous section 2.2.1) the shape is optimized taking into account following issues: In the case for an optimal tomographic reconstruction, it has been shown that a 50% beam overlapping at the FWHW (Full Width Half Maximum) of poloidally adjacent channels is advantageous for reducing aliasing for the reconstruction of high-frequency spatial components [87]. The decrease of the transmission function of one LOS is compensated by the overlapping of the rise of the next LOS. Thus, the sum of the transmission functions is always at the maximum and a complete sampling of a poloidal projection space is performed [88].

In toroidal orientation, the LOS width is usually optimized for an optimal S/N ratio in order to be able to map the entire dynamic radiation range of the individual experimental conditions. However, it must be considered that the aperture width can only be extended to the limit until toroidal bending and toroidal asymmetries can be neglected [82].

## 2.2.3 Theoretical calculation of the transmission function

Several methods exist to quantify the properties of a two dimensional bolometric detection system. The following statements in this section are based on [83, 89–92]. This section explains

how to calculate the transmission function of a bolometric detection system with a geometrical approach, comparable to the drawings shown in figure 2.4. It shall be noted that the transmission is calculated independently from the wavelength and optical effects such as reflections or further scatter components.

The line integrated measurement $f$ (with the unit W) by a multiple detector system can be described as:

$$f_i(x, y) = \int_{-\infty}^{\infty} \int_{-\infty}^{\infty} K_i(x, y) g(x, y) \, dx \, dy, \tag{2.6}$$

with $i$ being the index for each bolometer channel, $K_i(x, y)$ being the two dimensional geometric function defined by the geometric parameters of the camera and $g(x, y)$ being the radiation profile. Here, the origin of the $(x, y)$ CS is defined in the center of each detector (for a multiple channel camera). Thus, it allows to describe the geometric camera parameters also with respect to their incident angles, which are more practical values: $K_i(\theta, \xi)$. $\xi$ is the angle in the vertical plane (poloidal orientation) and $\theta$ in the horizontal plane (toroidal orientation). This function is then referred to as the transmission function or simply as the transmission.

Considering a symmetrical camera design, as presented in Section 2.2.2, the transmission function can be represented by the superposition of two individual imaging systems (here for an individual LOS): $K(\theta, \xi) = k_\theta(\theta) + k_\xi(\xi)$. Moreover, considering that the toroidal width of the LOS is smaller than the plasma structures to resolve, the transmission function can be approximated by:

$$K_i(\theta, \xi) \cong E_i \delta(x \cos \xi_i + y \sin \xi_i - r_i) \tag{2.7}$$

with $E_i$ being the Etendue (scalar value) of the respective LOS ($i$). The straight line equation $x \cos \xi_i + y \sin \xi_i - r_i$ describes the straight LOS (compare Equation 2.5). Thus, the measurements are assumed to be exact line integrals weighted with the Etendue. The Etendue can be calculated by integrating over the geometric function:

$$E_i = \int_{-\infty}^{\infty} \int_{-\infty}^{\infty} K_i(\theta, \xi) \, d\theta \, d\xi \tag{2.8}$$

The Entendue is a measure for the light-yield on the detector or the throughput of the respective camera channel. This approximation is currently applied for both bolometer systems in ASDEX Upgrade (see Section 2.4). However, the transmission function has to be calculated first.

The transmission can be defined as the fraction of the intensity $I_0$ of a parallel beam of radiation which reaches the detector. The detected intensity $I_D(\xi, \theta)$ depends on the incident angles $(\xi, \theta)$, and the areas of the aperture entrance ($P$) and exit ($A$). If the areas ($A$ and $P$) are considered

being parallel, $l_\theta(\theta)$ and $l_\xi(\xi)$ being the illuminated components of the detector in toroidal respective poloidal axis, the detected intensity can be calculated by [92]:

$$I_D(\xi, \theta) = I_0 \cdot k_\theta(\theta) \cdot k_\xi(\xi) = I_0 \frac{l_\xi(\xi) \cdot l_\theta(\theta)}{P} \cos \xi \cos \theta \qquad (2.9)$$

Figure 2.5 shows the corresponding drawing of a typical geometry of a single bolometer collimator in the poloidal plane and the reference CS. Here, the collimator is slightly tilted upwards. $y_D^+ - y_D^-$ is the width of the aperture exit (A) (which corresponds to the detector width in the poloidal plane) and $y_P^+ - y_P^-$ is the width of the aperture entrance (P). $L_C$ is the collimator length and $L_D$ is the distance from the collimator exit to the detector. The critical angles $\alpha_i$ are defined by following equations: $\alpha_1 = \arctan[(y_P^- - y_D^+)/(L_C + L_D)]$, $\alpha_2 = \arctan[(y_P^- - y_D^-)/(L_C + L_D)]$, $\alpha_3 = \arctan[(y_P^+ - y_D^+)/(L_C + L_D)]$ and $\alpha_4 = \arctan[(y_P^+ - y_D^-)/(L_C + L_D)]$.

For the case of an aperture width larger than the detector width $y_P^+ - y_P^- > y_D^+ - y_D^-$ (see Subfigure C in Figure 2.4), the poloidal length $l_\xi(\xi)$ can be calculated by:

$$k_\xi(\xi) = \begin{cases} [y_D^+ - y_P^- + (L_C + L_D)\tan\xi]\cos\xi & \text{if } \alpha_1 \leq \xi < \alpha_2 \\ [y_P^+ - y_D^- - (L_C + L_D)\tan\xi]\cos\xi & \text{if } \alpha_3 < \xi \leq \alpha_4 \\ (y_D^+ - y_D^-)\cos\xi & \text{if } \alpha_2 \leq \xi \leq \alpha_3 \\ 0 & \text{if } \xi < \alpha_1 \text{ or } \xi > \alpha_4 \end{cases} \qquad (2.10)$$

Similiar considerations apply for the other case, $y_P^+ - y_P^- < y_D^+ - y_D^-$. The transmission function in toroidal orientation has to be calculated differently. Depending on the desired viewing cone width and the restrictions by other in-vessel components (see Chapter 1.3.1) it is sometimes necessary to add additional structures in the LOS channel. Here, the resulting channels are then denominated subcollimators.

Figure 2.6 shows a schematic drawing of the typical geometry for a bolometer collimator with three subcollimators in the toroidal plane. Here, the detector width is indicated in the drawing by $z_D^+ - z_D^-$.
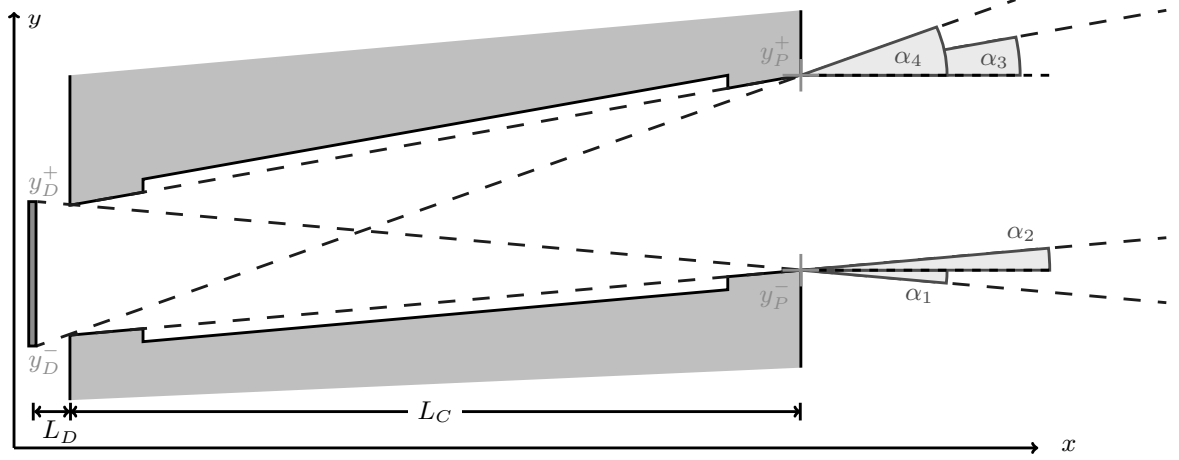
**Figure 2.5:** Schematic drawing of a typical geometry for a bolometer collimator in the poloidal plane. The dotted lines indicate the critical angles $\alpha_{1-4}$, $y_P^+$, $y_P^-$, $y_D^+$ and $y_D^-$ are indicating the edges of the collimator.
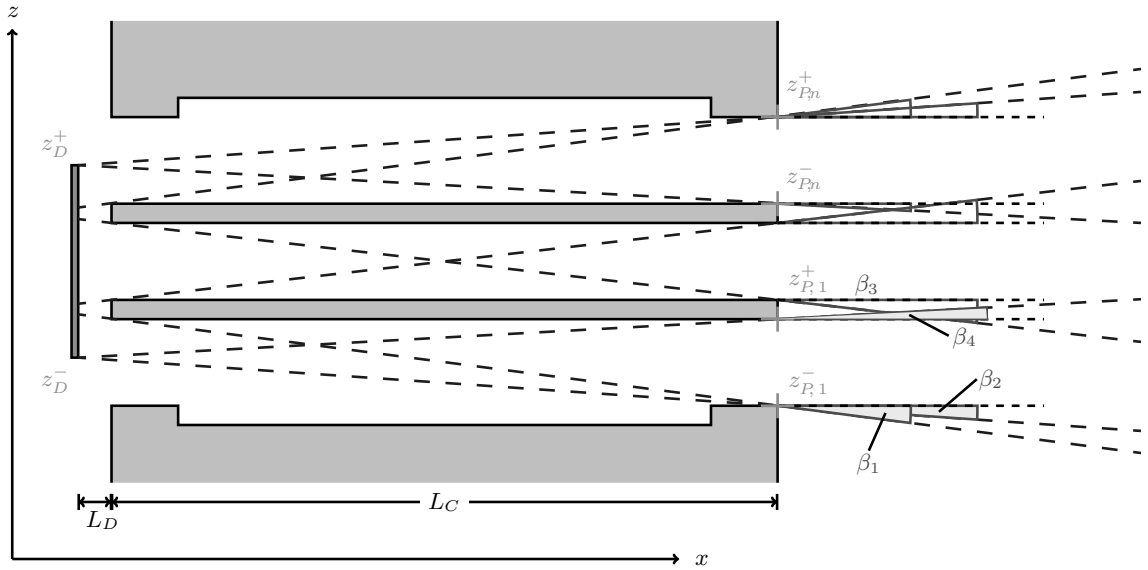


**Figure 2.6:** Schematic of a typical geometry for a bolometer collimator in the toroidal plane with three subcollimators as considered for ITER. The dotted lines indicate the critical angles $\beta_{1-4}$.

Three cases have to be distinguished here ($z_{P,i}^- \leq z_D^- < z_{P,i}^+ < z_D^+$, $z_D^- < z_{P,i}^- < z_{P,i}^+ < z_D^+$ and $z_D^- < z_{P,i}^- < z_D^+ \leq z_{P,i}^+$). The contributions of all subcollimator transmissions have to be added: $k_\theta(\theta) = \sum_{i=1}^{n} l_\theta^i(\theta)$. The critical angles are defined by $\beta_1 = \arctan[(z_{P,1}^- - z_{P,1}^+)/L_C]$, $\beta_2 = \arctan[(z_{P,1}^- - z_D^-)/(L_C + L_D)]$, $\beta_3 = 0$, $\beta_4 = \arctan[(z_{P,1}^+ - z_D^-)/(L_C + L_D)]$. The first case is shown here, the others are similar:

$$
k_\theta^i(\theta) = \begin{cases}
(z_{P,i}^+ - z_{P,i}^- + L_C \tan\theta)\cos\theta & \text{if } \beta_1 \leq \theta < \beta_2 \\
(z_{P,i}^+ - z_D^- - L_D \tan\theta)\cos\theta & \text{if } \beta_2 \leq \theta < \beta_3 \\
[z_{P,i}^+ - z_D^- - (L_C + L_D)\tan\theta]\cos\theta & \text{if } \beta_3 \leq \theta < \beta_4 \\
0 & \text{if } \theta < \beta_1 \text{ or } \theta > \beta_4
\end{cases}
\tag{2.11}
$$

## 2.3 Camera head design: pinhole or collimator

Typically, multiple detectors are integrated into one camera. The choice of the appropriate camera design plays a principal role during the first development stage of the diagnostic. However, space constraints do not always allow to select the optimal design. The different available types will be reviewed in this section.

Figure 2.7 shows a schematic diagram of the six principal camera versions. Subfigure A is the simplest version, one detector with a single small hole also referred to as "pinhole camera". Usually the detector is parallel to the aperture plane and perpendicular to the camera. Subfigure B shows a planar pinhole camera with multiple detectors viewing trough the same aperture. This is a common combination of several detectors, due to the advantage of having many LOS within little space and cost. Sometimes the detectors are tilted in direction to the aperture to optimize the light yield. Disadvantage of this design compared to a collimator design is, that the Etendue of each channel is different. Detectors looking through the aperture from the center of the housing have an increased sensitivity compared to the ones at the edge. Subfigure C shows a parallel collimator version. The aperture holes and the collimation direction is perpendicular to the viewed object. This design is widely used for X-ray tomography [93]. Subfigure D shows a radially converging collimator camera: The holes are focused towards the object located in the center of the field of view. The camera is usually larger than the viewed object, however with the advantage of having a superior resolution compared to parallel-beam collimators, a design commonly used for medical applications [94]. Subfigure E shows a radially diverging collimator or fan-beam shape camera which corresponds to the flipped camera Model D. It is used to enlarge the observable area and for large structure imaging. Certainly, the designs are not fixed, they can be a mixture or hybrid [95] of the previous versions, which is exemplary shown in Subfigure F. This type can be used to achieve increased sensitivity and resolution if only one camera is available.

Bolometric camera head designs for fusion application have been varied a lot in the past. One of the bolometer cameras projected for the Stellarator W7-X [67] is a large pinhole camera featuring 40 channels and corresponds to the design B. ASDEX Upgrade bolometers currently only have cameras of the design B, but it is planned to add additional collimator cameras during the next maintenance phase. The JET bolometer camera KB5V [96] is arranged as a diverging collimator camera (E).
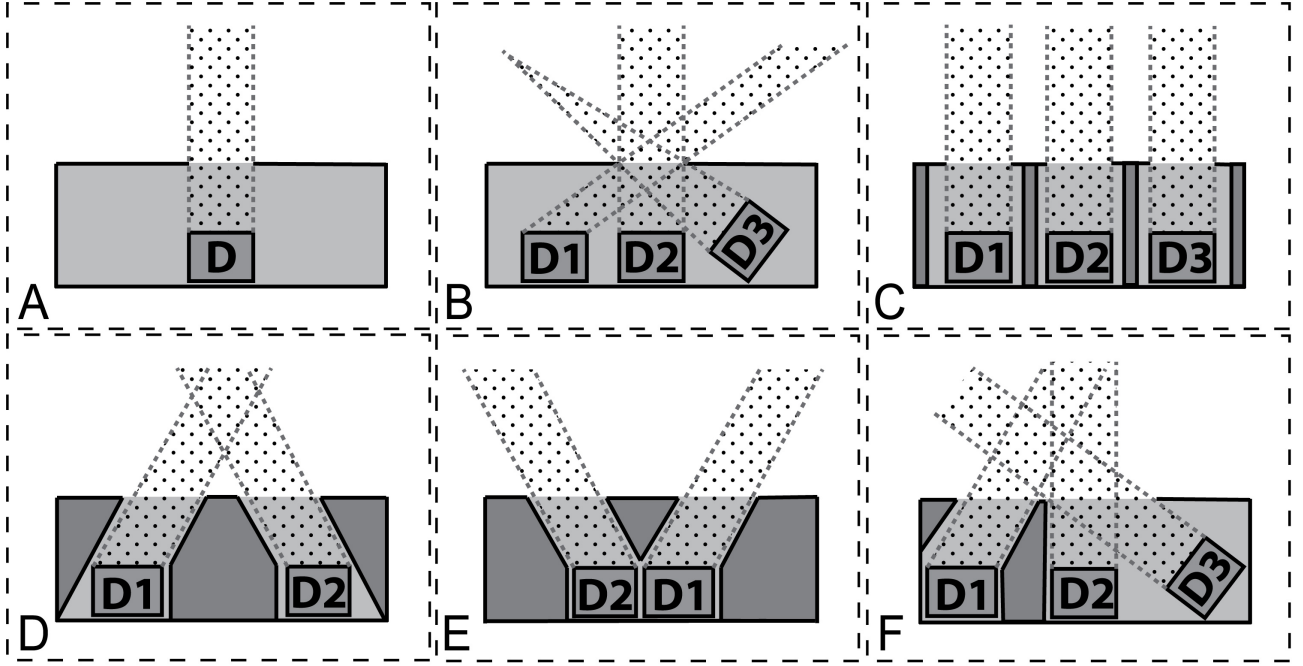
**Figure 2.7:** Schematic drawing of different camera versions. (A) Single aperture and single detector, (B) Pinhole camera with multiple detectors, (C) Parallel hole collimator camera, (D) Converging collimator camera, (E) Diverging collimator camera, (F) Mixed collimator camera. The dotted lines indicate the orientation of the LOS.

## 2.4 Bolometer diagnostic at ASDEX Upgrade

ASDEX Upgrade has two main bolometer systems: An AXUV diode and a foil bolometry system. The foil bolometers are integrated in the vessel since the start up of the experiment in 1991. The AXUV diode system has been recently installed in 2010 [97], but will not be further discussed in this work.

The foil bolometer system is based on a four-channel module. The basic design has not been changed since its introduction from Mast [50] in 85'. Apart from the change of the insulating carrier foil substrate of the sensor, from Kapton to Mica and then silicon nitride, only further cameras have been added in the vessel to increase the amount of available LOS. During the start-up of ASDEX Upgrade 32 LOS were available. Integrated in six cameras, the system features now 116 LOS. Eight LOS have been added recently (the FHS camera, see next section) viewing the divertor from the upper high field side [55]. In the next section, the basic camera design will be presented explaining the current approach of determining the LOS orientation in the ASDEX Upgrade vessel.

### 2.4.1 Camera design, material and housing

Due to the continuous upgrade of the bolometer diagnostic in ASDEX Upgrade and the resulting gradual improvement of the cameras, different camera housing designs exist, but all of them

are based on the same pin-hole design. As an example, the FHC camera is presented in detail. Figure 2.8 shows in Subfigure A a computer-aided design (CAD) drawing and in Subfigure B a photo. The front coverage has been removed for a better view of the components.
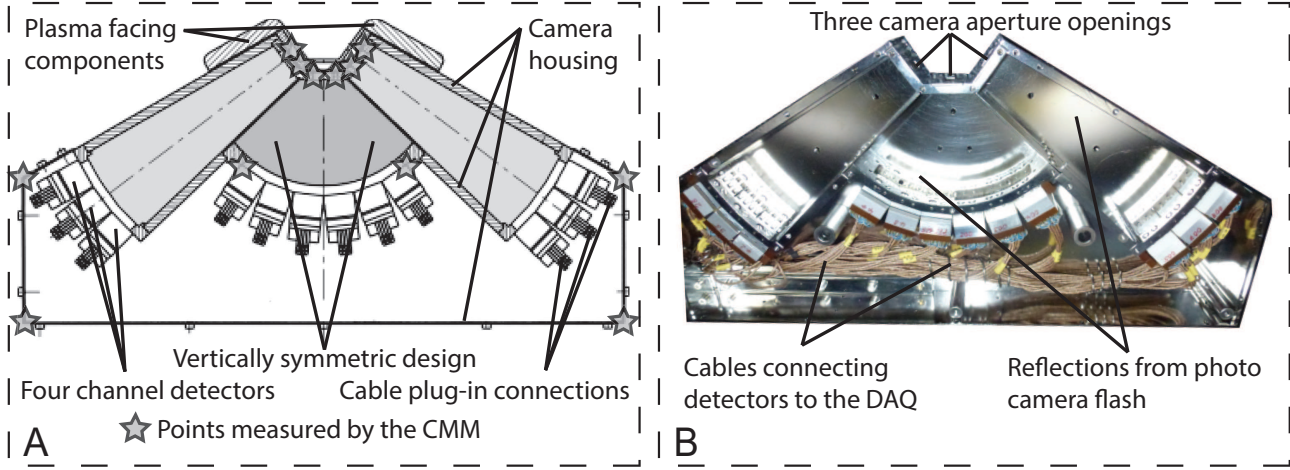


**Figure 2.8:** Subfigure A is shows a CAD image of the FHC bolometer camera and Subfigure B shows a photo of the opened camera housing. 12 detector arrays (of 4 channels each) are mounted in the camera. The photo shows the numerous cables which are needed to connect all detectors. The smooth aluminium surface appears by the reflected flash of the photo camera which illuminates certain areas. The points measured by the Coordinate Measuring Machine (CMM) are indicated by stars.

The housing of the cameras is based on aluminium plates which were screwed and partly welded together to create a pie-shaped box construction so that they can be easily accessed. The camera is based on the pinhole camera principle or design B as explained in Section 2.3. The FHC can also be regarded as three separate cameras, due to their three individual pin holes. Most components of the housing are "off the shelf" materials and have not undergone any special treatment. The four channel detectors, in white aligned at the bottom of the camera, are all aligned towards their respective pinhole and are placed next to each other on a semi circle. Thus, the three parts of the FHC camera are symmetrical to the vertical plane, hence the part on the left and the right are identical. Front and rear are similar as well. Three four channel detectors are in the left and right part of the camera and six are mounted in the center part. The detectors are connected to special low noise and low impedance cables in the back via custom plug-in connections. The large amount of necessary cables can be seen in the photo. The other cameras in ASDEX Upgrade are built according to the same principle, with minor differences depending on the amount of LOS.

In order to determine the orientation of the LOS in respect to the ASDEX Upgrade CS, the camera is mounted on its intended position and certain points of the camera are measured with a Coordinate Measuring Machine (CMM) (see Chapter 3.1.3). A few of these points are indicated in the Subfigure A. The edges of the housing are measured and some edges of the four channel detector at positions where access is possible. The remaining positions of the single detectors have to be calculated from the measurements and synchronized with CAD

data. However, this process still depends on the correct manufacturing and integration of the camera.

### 2.4.2 Line of sight distribution

Knowledge about the LOS distribution in ASDEX Upgrade is an important factor for preparing the in situ measurement and asses the theoretically possible amount of LOS which can be accessed by the calibration and measurement device (see Chapter 3.2). Therefore, the bolometer foil LOS distribution in ASDEX Upgrade is presented in this section. Figure 2.9 shows the distribution as toroidal view in Subfigure A and as a poloidal view in Subfigure B. Boxes with the camera names show the approximate positions of the cameras and the orientation of the LOS in the vessel are indicated with black lines. The LOS have their source in the camera housing and continue until they reach a PFC. A high density of LOS can be found around the X-Point, the divertor area and plasma edge due to the physics demands for a high spatial resolution in this area and in order to minimize aliasing effects.
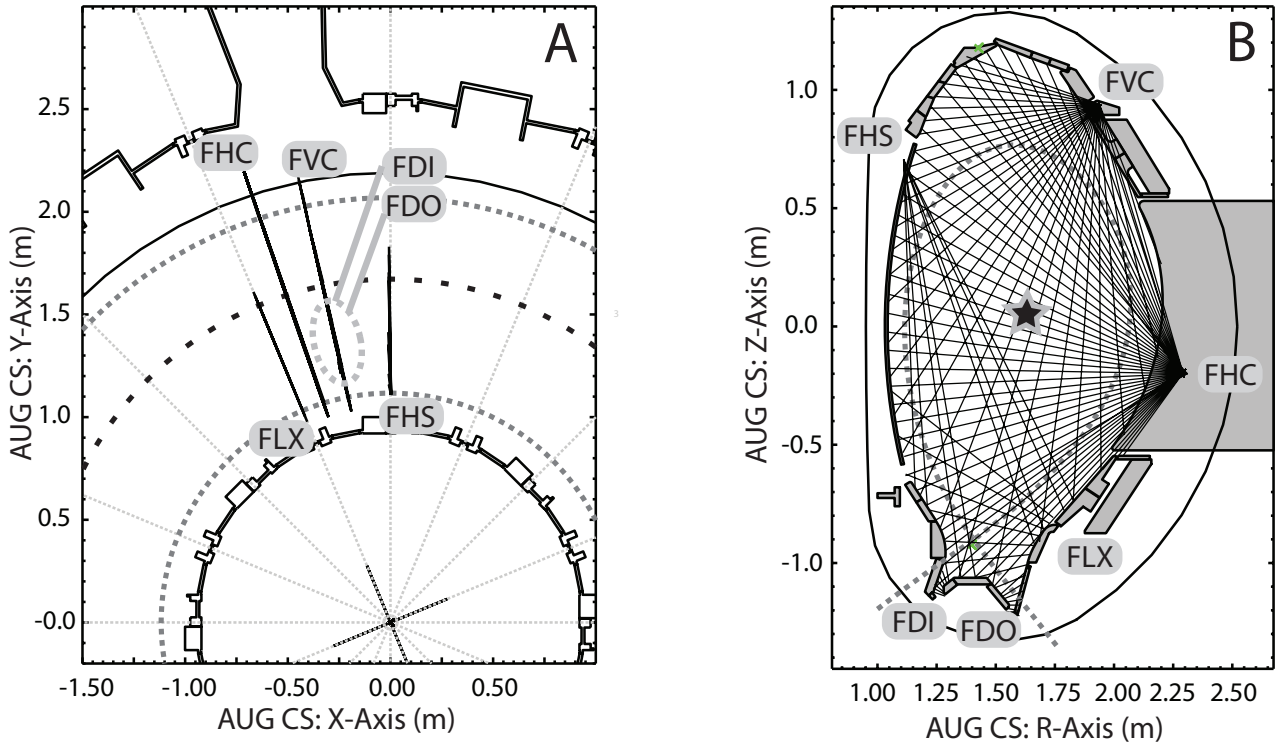


**Figure 2.9:** ASDEX Upgrade LOS distribution. Subfigure A shows the toroidal, Subfigure B the poloidal LOS distribution. The boxes indicate the approximate positions of the cameras. The separatrix is shown by the dotted grey line, the center of the magnetic axis is shown by the black dotted line (A) and as a star (B).

Six pinhole cameras are capturing the entire poloidal cross-section of the plasma vessel: The FVC camera (32 channels) has a vertical and horizontal view, the FHC (48 channels) a hori-

zontal view, the FHS (Eight channels) focuses on the high-field side[1] of the plasma, the FLX (Eight channels) views the X-point and finally FDI and FDO (both eight channels) view the inner and outer divertor. The system also features an additional camera for the monitoring of ECRH stray radiation. This camera is not treated in this work because its measurements are not relevant for the calculation of $P_{rad}$, neither used for tomography. All cameras, apart from the FHS, are installed in Sector 5 of the ASDEX Upgrade vessel which significantly simplifies the in-situ measurement setup (see Chapter 4).

## 2.5    Bolometer diagnostic for ITER

The bolometer diagnostic for ITER is still in the development stage. That the general requirements for diagnostics in ITER are very challenging, has been discussed in detail in the introductory chapter of Section 1.2. In this section, a brief overview of the status of development and the future steps shall be given.

The first proposal of a bolometer system for ITER was published almost 20 years ago under the assumption for the first ITER design[2] [98]. Most of the conclusions drawn at that time are still valid, such as using a distributed camera layout and arranging the bolometer camera between the blanket and divertor modules. The metal resistor bolometer detector technology is currently the only type which has a high development state including wide application experience in various fusion experiments. The bolometer system at JET, which is based on the metal resistor type (respectively the "ASDEX-type", see Chapter 2.1.2), is considered being the most relevant to derive the next development steps for ITER [60].

One major task was to develop alternative radiation resistant materials acting as substrate and absorber on the detector with adequate thermal and dielectric properties [63, 99]. It was established that the originally used substrate materials Mica[3] or Kapton®[4] cannot be used [22], due to the neutron induced degradation and swelling of these materials. Many irradiation tests have been performed in the past in order to evaluate alternative materials [100–103]. The use of a low stress silicon nitride for the carrier material (substrate) is currently considered the best option in order to survive the ITER radiation dose rates [60]. For the meander material, gold is considered being critical as the high neutron fluencies expected in ITER will transmute it to mercury, thus it was substituted with platinum having a ten times smaller thermal neutron capture cross-section than gold. However, the final material composition is not yet determined and work in this area is still under progress.

---

[1]The high-field side is the area left from the circular axis of the torus in a poloidal cross-sectional view [8], respectively left of the star, in Figure 2.9 (B).

[2]Also know as ITER-98 Design and Physics Basis.

[3]Mica is a group of sheet silicate minerals.

[4]Kapton is a high heat-resistance polyimide material developed by the company *DuPont*.

At IPP, a prototype detector based on silicon nitride with a Pt meander and absorber has been been manufactured firstly in '05 [104]. As a next step, a 12 μm thick absorption layer was successfully deposited on the sicilium nitride membrane in 12' [60] to ensure the necessary attenuation length for the 25 keV photons generated in advanced scenarios for ITER. The spectral sensitivity [105] has been measured in cooperation with the Physikalische-Technische Bundesanstalt in Berlin and confirmed a sufficient absorption range.

Secondary engineering constraints have to be respected, such as performing an integration study [23] in order to evaluate spatial requirements e.g. in the relevant diagnostics port plug (Equatorial Port Plug 1 of ITER). There have been many occasions which required the reassessment due to the continuous change of the ITER design. One of the major ITER design updates, was to integrate the Edge Localised Mode (ELM)/Vertical Stability (VS) coil. If and how these coils exert an influence on the limited space availability had to be studied [39]. Additionally, work to evaluate possible bolometer electrical contacts, connections and cables [103, 106] have been conducted, besides investigating and proposing the appropriate electrical infrastructure with connectors and feedthroughs [107].

As explained in the motivation in Chapter 1.3, IPP has already been working during the past five years on developing preliminary designs for the ITER cameras. In the next section, the current status of the camera design proposed from IPP will be presented, besides a brief review of the past development steps in order to justify the design choices.

## 2.5.1 Camera design, material and housing

Several versions of a camera prototype have been designed, manufactured and investigated. Objective was to gather an understanding of all major parts influencing the camera performance. Studies in order to optimize the LOS distribution in a poloidal cross-section of the vessel have been conducted in the past with the ITER-98 design [89] and were recently performed again with the current design. Thus, the two principal camera types have been evaluated by proposing a draft design of a five channel collimator and a pinhole camera.

Most of the cameras will have to be placed between the support structure and the FW elements of the vessel, which results in little available space, respectively limiting the camera length. Moreover, the constraints described in the motivation of the work (see Chapter 1.3), will have to be respected. It was established that in order to reach the extremely narrow LOS width of only a few degrees, only a collimator type camera could be realized [38] at these locations. All in-vessel and divertor cameras ($\approx 60\%$ of the LOS) will be based on a collimator design, but for cameras mounted in other areas, e.g. the equatorial port plug (EPP), pinhole cameras could be envisaged.

Figure 2.10 shows the three gradually developed designs of the collimator as a CAD image from the years '11, '12 and '13. Components which not necessarily influence the LOS, such as
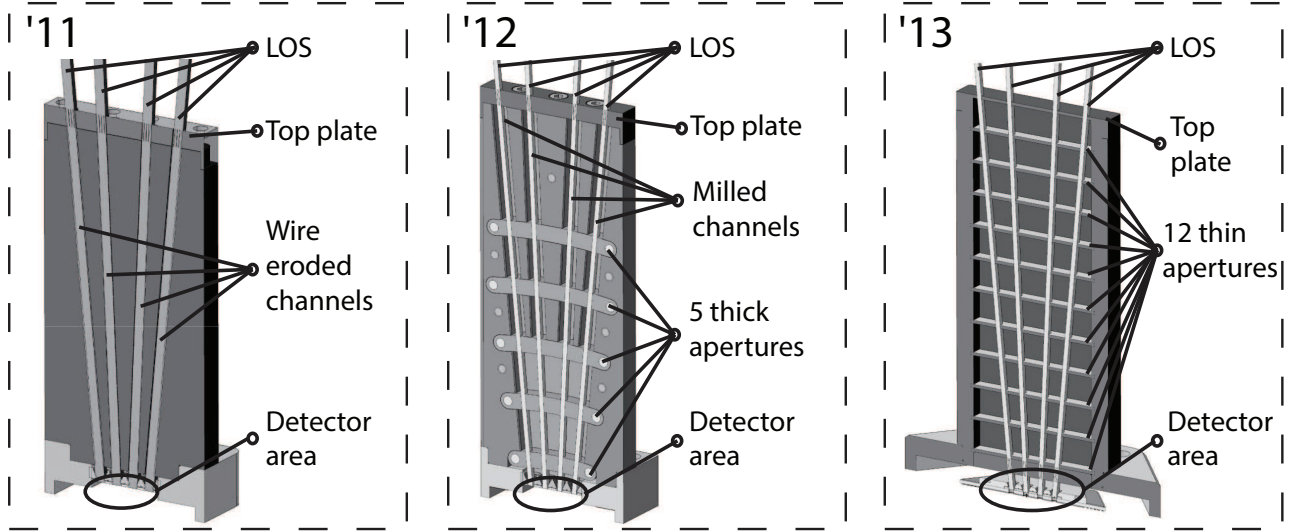
**Figure 2.10:** From left to right, the three collimator cameras are shown which have been developed in the last years '11, '12 [108] and '13. Here they are shown in a cutaway view generated from the corresponding CAD drawing to illustrate the LOS. The subcomponents such as top plate, collimator body and apertures are higlighted with different color shades.

thermal contact foils, connections screws, cables and sockets are not shown. The LOS and the four main components of the collimator are denominated in the drawing of each model version. In the following, these main components will be explained in more detail:

1. The collimator body or also to be referred as collimator housing which is the largest and central part of the camera. Its length $L_c$ is one of the main parameters which determines the viewing cone width (see Chapter 2.2.3). Model '12 and '13 consist of two half sections, the back and front collimator housing. Only the back part is shown in the sectional drawings of Figure 2.10. The Models '11 and '12 contain additional channels in the collimator housing which are manufactured by wire erosion and milling. The collimator housing of the Model '13 is only an empty case which can be equipped with up to 12 apertures defining the LOS.

2. Multiple apertures can be mounted inside the collimator housing in the Models '12 and '13. Thus, the aperture openings can be adapted to the desired viewing cones without changing the whole assembly. In the '11 Model the LOS are only defined by the wire eroded channels (see Figure 2.10)

3. A top plate can be screwed on top of the collimator housing, which corresponds to the first or top aperture. Furthermore, it provides the precise fit of the two housing parts which are screwed together. Details about this top plate will be explained in the section 2.5.3 for the Model '12.

4. The area on the bottom of the collimator housing is reserved for the detector. Here, the models were designed so that the standard four channel detector from ASDEX Upgrade can be used. Furthermore, a mounting bracket is located at the end of the collimator,

allowing a connection to the vessel wall or with the laboratory clamping device (see Figure 3.5).

One of the driving parameters was to build a collimator which can endure a maximum level of heat flux through all components, particularly the apertures must not be twisted or deformed due to large temperature gradients of up to $\delta T = 300°$ ($T = 450°$C at the top plate and $T = 150°$C at the vessel mounting). For this purpose, the decision was taken early to manufacture the collimator components from a Molybdenum-titanium-zirconium[1] (TZM) alloy. It is considered as candidate material for many ITER high-heat flux applications such as for the divertor heat sink or optical diagnostics equipped with in-vessel metallic mirrors [109].

TZM has various advantageous properties such as allowing operating temperatures up to 1400°, a lower thermal expansion coefficient and improved thermal conductivity compared to standard stainless steel alloys[2] used for the bolometer cameras in the past e.g. in ASDEX Upgrade or JET. Furthermore this material provides a high level of strength, good resistance to radiation swelling, good corrosion resistance, good machining characteristics and its ultrahigh vacuum compatibility is confirmed by acceptable outgassing rates [110].

The stability criteria influenced also the first camera Model '11 which was milled from a single piece of TZM. The four channels have been directly wire eroded into the material which can be described as one single very thick aperture corresponding to the camera length. Measurements with the manual version of IBOROB [91] revealed the downside of that design: Reflections along the entire length of the channel walls lead to a widespread LOS in both poloidal and



**Figure 2.11:** Isometric CAD view of the collimator prototype Model '12.

toroidal direction compared to the desired theoretical one (see Chapter 4.1.1 for more details). However, a benefit of this basic design was the simplicity of manufacturing and probably the best possible thermal properties.

Thus, an advanced and more modular design was developed: The Model '12 which can be seen in detail in Figure 2.11. It shall be noted that most results concerning the ITER collimator

---

[1]TZM contains: 99.2-99.4% Molybdenum, 0.50% Titanium, 0.08% Zirconium and 0.01-0.04% Carbon.

[2]Thermal conductivity for TZM: $\lambda_{TZM} = 126\,\mathrm{Wm^{-1}K^{-1}}$ compared to a stainless steel alloy (AISI 316, austenitic and non-magnetic): $\lambda_{AISI-316} = 16.3\,\mathrm{Wm^{-1}K^{-1}}$.

camera of this work are based on this model (see chapter 4.1). Therefore it will be explained in more detail than the other models.

The camera housing has no longer the task to define the LOS. It only acts as a support for the apertures. The channel walls are only separating each channel and shielding the detector from unwanted radiation from all other directions. The housing contains five insertions allowing to integrate the slightly curved apertures. Two locating pins at the edge of the camera body are used to proper align and fasten each aperture in its position. In addition, the apertures are counter-sunk into the housing with slightly recessed grooves. This ensures that no radiation can pass through a remaining small slit between aperture and body.

Different openings can be integrated in the apertures without changing the whole camera body design. Since different LOS width are considered being an advantageous property for ITER in order to provide the best S/N ratio, respectively light yield at different camera locations in the vessel, this design has been choosen. Additionally, with a modular design, it would be easier to make comparative experiments in order to analyze the effects of the different components.

The overall aperture width is sequentially increasing from aperture 1 to 5 due the spreading of the LOS over its length in the camera. The top rectangular aperture is denominated top plate (see Section 2.5.3). The apertures are numbered consecutively (see Section 2.5.2) and labeled in the figure for proper identification: The first aperture (1) is closest and the last aperture (5) is furthest to the detector. The four channel detector is integrated in the camera housing and not shown in the figure.

The Model '13, which is also shown in the Figure 2.10 was the subsequent design. The reasons for these design changes will be discussed in the results chapter 4.1. However, it is only shown for the sake of completeness, it was not investigated as part of this work. The next section will describe the different aperture and top plate types developed for the Model '12.

### 2.5.2   Aperture design

The apertures have always been manufactured as a set of five. Figure 2.12 shows the four different aperture versions which have been developed and studied during this work. The base frame of alle apertures is the same, but they feature different toroidal and poloidal openings. Moreover, they have been built slightly over sized to allow variable channel openings and later modifications without pushing to the outermost manufacturing limit. The channel openings are rectangular and equally large for all four channels within one aperture. However, the aperture size depends on the aperture number (1-5), they are following the LOS broadening within the collimator.

The base frame of the apertures was manufactured using a Computerized Numerical Control (CNC) machine and the channel openings and the holes for the locating pins via wire and die
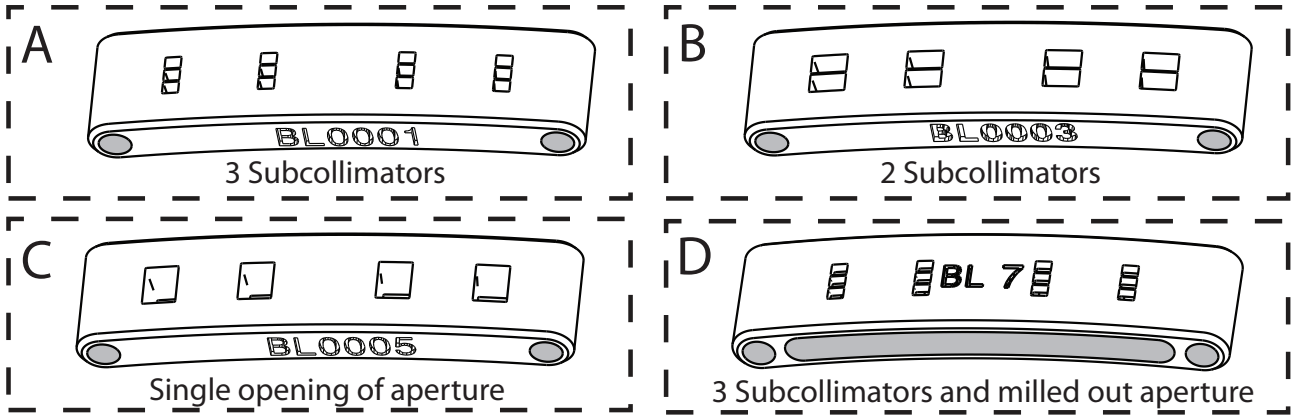
**Figure 2.12:** The four different aperture version of the '12 collimator camera model: BL0001 has the smallest opening with three subcollimators (A), BL0003 a medium size with two subcollimators (B) and BL0005 has the largest (C). BL7 is a modified version of BL0001, the inner part has been milled out (grey area in Subfigure D).

sinker Electric Discharge Machining with a specified accuracy of $0.02\,\mu m$ by the manufacturer. This manufacturing process is currently considered being one of the most precise while creating such small and complex objects. The definitive accuracy limit can be exemplary understood by the aperture openings. They are not exactly rectangular as it seems in the figure, because the minimum inside radius is defined by the wire diameter.

### 2.5.3 Top plate design

The top plate corresponds to the last aperture on top of the collimator housing. Figure 2.13 shows the four different top plate versions. Six countersunk screws connect the top plate to the housing, the screw holes are indicated in Subfigure D. The top plate of the collimator camera Version '12 is not curved as the apertures, but the aperture holes are following the alignment of the LOS. Thus, the holes are slightly tilted according to the orientations (see Section 2.5.4). The exact design parameters of the top plate, the number of subcollimators $N_t$, the poloidal opening $d_p$ and the toroidal opening $d_t$, are summarized in table 2.1.

The toroidal opening $d_t$ is referred to the toroidal width of each subcollimator, if they exist. For BL0005 it simply corresponds to the total toroidal width of the aperture. E.g. for BL0001: $N_t = 3, d_t = 1.23\,mm : N_t * d_t = 3.69\,mm$. The difference between BL0005 ($d_t = 4\,mm$) is in account of the division bars which have a thickness of $0.15\,mm$.

One version will be explained in more detail: Top plate version ITERBolo-6 in Subfigure C features a grid in order to filter microwave stray radiation from the external Electron Cyclotron Resonance Heating (ECRH) systems. The ECRH uses microwaves to heat the plasma and can provide several MW of output power. However, if stray radiation reaches the bolometer detectors a power is measured, which cannot be related to plasma radiation and thus is a source of quantifiable uncertainties.
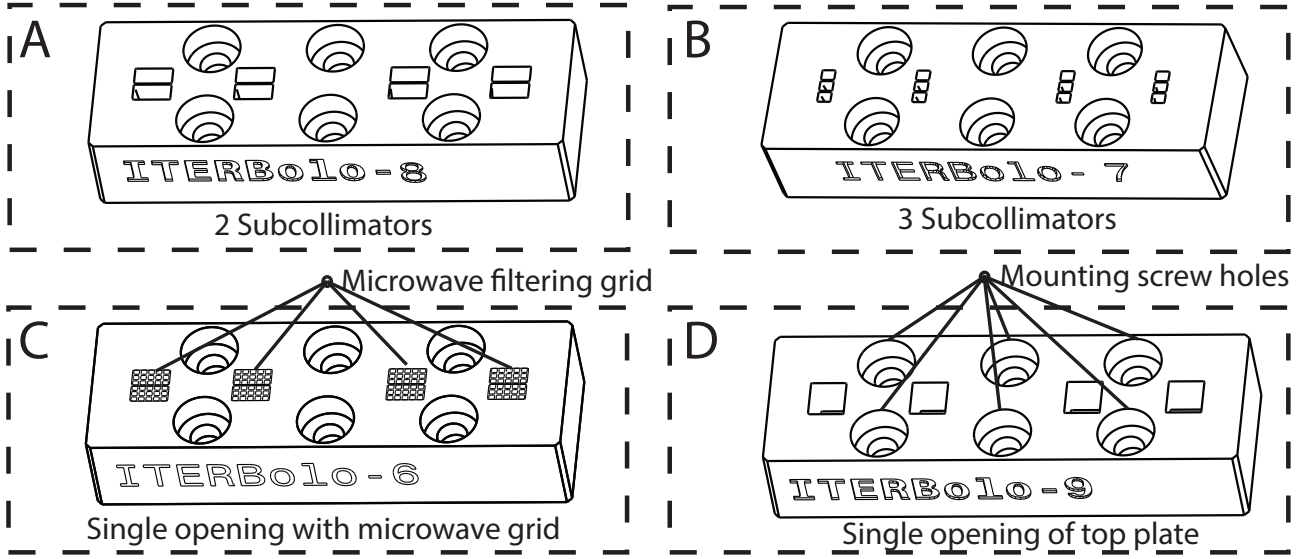
**Figure 2.13:** Four different top plate designs for the ITER bolmeter prototype camera. Sub-figure A is showing the version with 2 subcollimators coressponding the BL0003 apertures and Subfigure B corresponds to the BL0001 apertures. The version ITERBolo-6 (C) has an integrated microwave filtering grid in the aperture openings. The mounting holes are indicated exemplary for the version ITERBolo-9 (D) corresponding to the BL0005 apertures.

Therefore, a special grid was integrated in this top plate to act as attenuating wave-guide for microwaves in the relevant frequency range for the ITER ECRH ($\sim 170\,\mathrm{GHz}$). It consists of small channels with a toroidal width of $t_{micro} = 0.54\,\mathrm{mm}$ and a poloidal width of $p_{micro} = 0.4\,\mathrm{mm}$). The length of the channels is $5\,\mathrm{mm}$, which results from the need to achieve a certain damping[1].

**Table 2.1:** Design properties of the four top plates for the collimator Model '12.

| Top plate | No. of subcollimators $N_t$ | Poloidal opening $d_p$ | Toroidal opening $d_t$ |
|-----------|------------------------------|------------------------|------------------------|
| ITERBolo-6 | 1 | 3.73 mm | 4 mm |
| ITERBolo-7 | 3 | 1.5 mm | 1.23 mm |
| ITERBolo-8 | 2 | 4 mm | 1.93 mm |
| ITERBolo-9 | 1 | 3.73 mm | 4 mm |

The remaining grid material between the holes is about $0.15\,\mathrm{mm}$ thick which is necessary due to material stability issues, particulary important to endure the temperature gradients (see collimator design in section 2.5.1). Disadvantage, is certainly the lower light yield. Comparing the effective aperture area of top plate ITERBolo-8 (Subfigure D) without a grid and the version with a grid ITERBolo-6 (Subfigure C), about 50% difference can be calculated.

---

[1]Measurements with a microwave test setup at the University of Stuttgart could confirm a damping of at least $70\,\mathrm{db}$ in the range of $125 - 225\,\mathrm{GHz}$ [111].

### 2.5.4 LOS configurations

Figure 2.14 shows the theoretical transmission of BL0005/ITERBolo-9(6) as calculated with equation 2.9. This aperture and top plate configuration has one of the widest viewing cones. The coordinate system for this and the following figure is located in the respective detector of each channel. It can be seen that the toroidal orientation is the same for all channels because they are vertically (poloidally) arranged, one above the other.
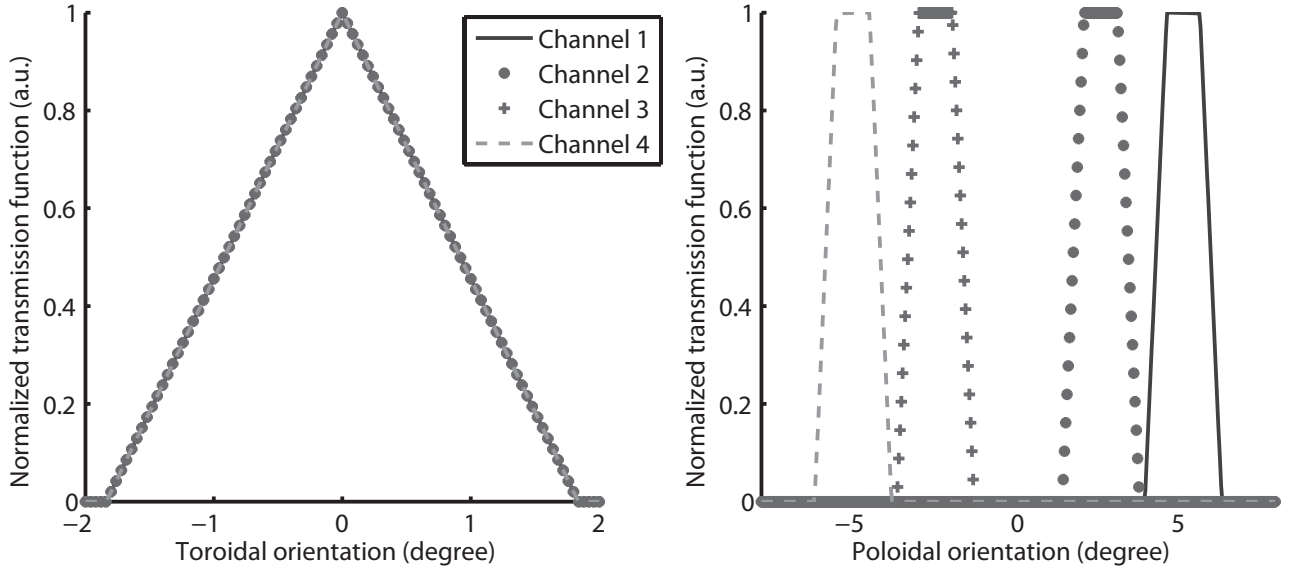


**Figure 2.14:** Normalized theoretical transmission function (Channel 1,2,3,4) of configuration BL0005/ITERBolo-9 in toroidal (left) and poloidal (right) orientation. The shape is trapezoidal in poloidal orientation and triangular in toroidal orientation.

The toroidal LOS shape is triangular and the poloidal LOS shape is trapezoidal. Due to the large poloidal opening of $d_p = 3.73\,\text{mm}$ (see Figure 2.4 (C)) the aperture size is larger than the detector size, which in this setup corresponds to $1.5\,\text{mm}$ length in the poloidal orientation. Moreover, because of the diverging design of the collimator camera the LOS are not overlapping or are bordering each other. The larger distance between Channel 2 to Channel 3 and the symmetry of Channel 1/2 and 3/4 is as expected from the symmetric design (compare Figure 2.12 showing the aperture design).

Concerning the toroidal width, the maximum range amounts to $\Delta\theta_{max} \approx 4°$ and $\Delta\theta_{FWHM} \approx 2°$ at its FWHM. The toroidal maximum for all channels is at $\theta = 0°$ which here is trivial, because the CS is defined in the center of the channels. The poloidal channel orientation, which corresponds to the center or main focus of the transmission, is listed here for each channels: $\xi^1_{max} = 5.15°$, $\xi^2_{max} = 2.58°$, $\xi^3_{max} = -2.58°$, $\xi^4_{max} = -5.15°$.

Figure 2.15 shows the theoretical transmission of the configuration BL0001/ITERBolo-7. Here, the aperture openings are much smaller and correspond to a narrower viewing cone. For the toroidal width, the maximum range amounts to $\Delta\theta_{max} \approx 1.2°$ and $\Delta\theta_{FWHM} \approx 0.6°$ at its
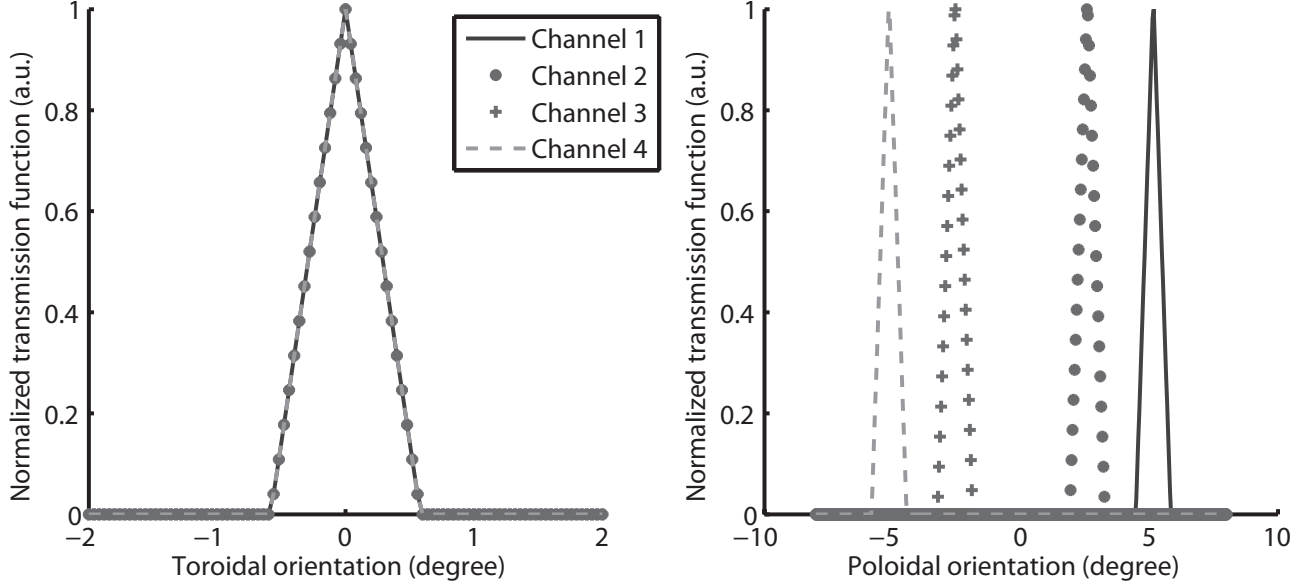
**Figure 2.15:** Normalized theoretical transmission function (Channel 1,2,3,4) of aperture configuration BL0001(BL7)/ITERBolo-7 in toroidal (left) and poloidal (right) orientation. The legend applies to both plots. In the toroidal orientation all channel curves overlay exactly, which is as expected.

FWHM. The poloidal maximum width amounts to $\Delta\xi_{max} \approx 1.4°$ and $\Delta\xi_{FWHM} \approx 0.7°$ at its FWHM. The toroidal and poloidal orientations are for all aperture designs the same.

BL7/ITERBolo-7 has in principle the same parameters as BL0001/ITERBolo-7, respectively the same theoretical transmission function. The differences will be visible later in the measurements (see section 4.1.3.4). BL0003/ITERBolo-8 is a mixture between the two presented versions. In poloidal orientation, it has a slightly larger poloidal trapezoidal flat top and in the toroidal orientation the LOS width is between the values shown in the two previous plots (not shown here).

# 3. Experimental setup

This chapter describes the experimental setup of IBOROB, the ITER Bolometer Robot Test Rig, shown in Figure 3.1, which was developed to measure the alignment and the characteristics of the LOS both in the laboratory and in ASDEX Upgrade tokamak (see Figure 4.22). Firstly, a requirement analysis is performed to determine the properties of all necessary parts. The physical basis, which consists of the manipulator, the radiation source and a system for the absolute calibration, is presented. The final implementation of the system is presented divided into sections for the hardware and software. The latter consists of a remote control program which was realized as a National Instruments LabVIEW program with the help of the Imaging Lab Robotics Library for KUKA [112] and combined with the existing bolometer Data Acquisition (DAQ) [69]. The capability of the software is explained with a focus on the measurement procedure. The kinematic path planning and correlation of measurement signals are addressed as well. Finally, the constraints of the system and the measurement accuracy are discussed.
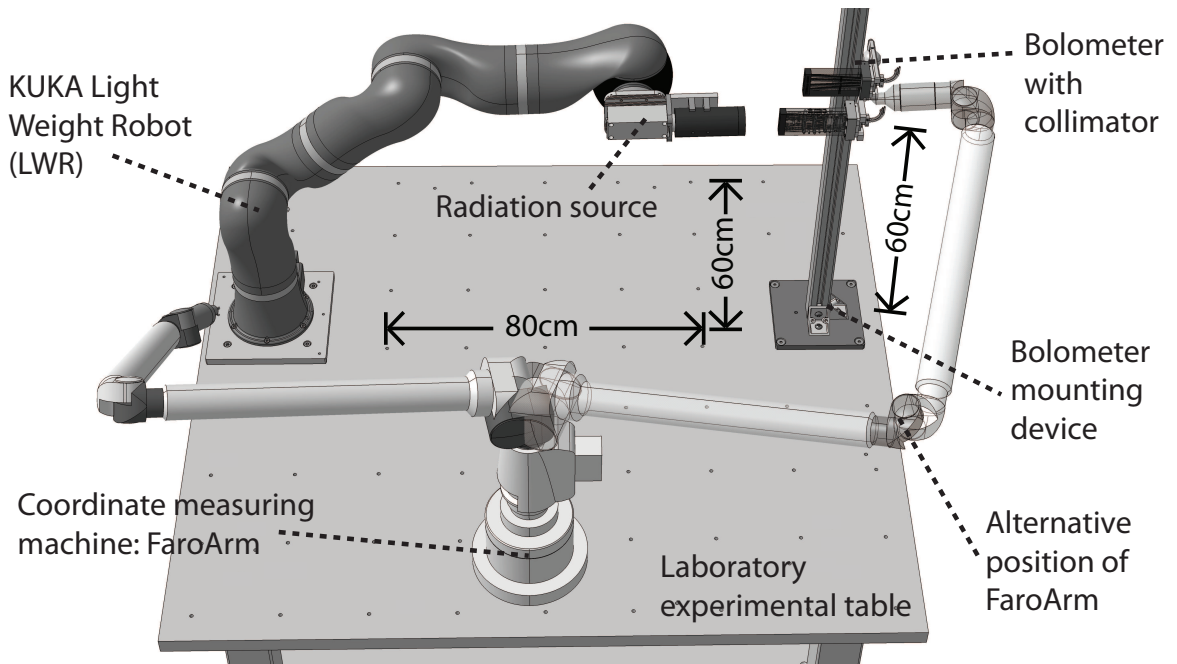


**Figure 3.1:** Perspective CAD drawing of IBOROB in the laboratory setup. KUKA LWR on the left, the FaroArm in the middle and on the right two bolometers mounted on the aluminium profile via the clamping elements. The table has a 20 cm pitch pattern of holes.

## 3.1 Requirements for a line of sight calibration device

Main objective of this work is to develop a device to allow the measurement of the geometrical calibration and characterization of the LOS of bolometer cameras. For this reason, a search was undertaken examining the procedures, methods and architectures of systems actually in place for similar challenges.

Methods to allow the geometric calibration of cameras used for photogrammetry already exist and are well established. Classic close-range digital or analog photo cameras, which acquire directly a two dimensional image, are commonly geometrically calibrated by observing a pre-defined pattern (e.g. a chessboard consisting of $8 \times 8$ black and white squares) from different viewpoints. This set of images, which is called a bundle adjustment, is then usually solved by a least-squares algorithm according to an optimality criterion involving all image projections [113] which finally allows to calculate the camera calibration parameters.

Cameras with larger focal lengths, e.g. devices for remote sensing (telescopes) or aerial mapping [114], which have a more comparable optical system like bolometers, use a combination of a collimated light source with a goniometer. The designated camera to be calibrated is mounted on a pan-tilt table where it can be flexibly rotated and tilted in front of a collimated radiation beam. The orientation of the goniometer is then correlated with the camera image and allows to derive the viewing direction of a set of pixels [115].

A goniometer based approach could be used to determine the precise angular orientation of the bolometer LOS in the laboratory. A positioning goniometer consists usually of an electro-mechanical stage which can rotate an object very precisely in respect to another axis in space. But for measurements in the vessel this is not applicable due to the fixed positions of the bolometer arrays in the fusion experiment. These techniques are not suited to address our problem directly, but can be used to derive a dedicated approach.

The Charge Exchange Recombination Spectroscopy (CXRS), which is a diagnostic to measure the ion temperature, rotation velocity and impurity density, needs also to determine the exact alignment of the LOS to operate at full performance and functionality [116]. However, this system has the possibility to exchange the spectrometer and replace it with a light source without the intervention of the optical equipment which define the LOS. By backlighting the optical fibers the light beam of the source shines in the torus and can then be measured directly. Simply by putting an object like a piece of paper in the light path, *"the position of the focal points and the optical heads are measured"* [31] with a Coordinate Measurement Machine (CMM).

The measurement of neutron emissivity is performed by means of neutron flux monitors. This diagnostic also needs an appropriate calibration strategy in order to guarantee a certain spatial resolution. The Vertical Neutron Camera (VNC) of ITER will be composed of two fan-shaped

collimating structures with a total number of 11 collimators (here called apertures) [117]. The plan for this diagnostic is to move a neutron emitting calibration source inside the experimental vessel. A re-calibration in an external room (Hot cell or neutron test area) on a regular basis of individual detectors should be made available as well [15]. This moving calibration source will be used for both absolute intensity calibration and a geometrical calibration of the camera.

Related ideas can also be derived from the Thomson Scattering system proposed for ITER to measure the central electron temperature and density profile. In order to provide a constant level of diagnostic performance, a calibration of this diagnostic has to be performed regularly in situ. Apart from the need of a spectral calibration, which is performed using a broadband light source with known spectral profile, the current developers [118] state *"Though in practice it will be desirable to measure separately the calibration of the collection path optics and the spectrometer plus detectors. The collection path optics are likely to have an age related calibration [...] while the spectrometer may have an angular dependent calibration of the interference filters giving rise to a different calibration for different scattering source locations [...]".* Moreover, the ITER thermography diagnostic, which provides data about the spatial and temporal evolution of the first wall surface temperatures, makes the same proposal: *"A calibration source mounted on a robot to be used during shutdown"* [41]. In other words these are all requests for the development of a geometrical calibration device for the optical paths of different ITER diagnostic systems.

All these development proposals are based on a similar approach:

> **The spatial calibration of diagnostic optical properties by movement of a radiation source on well-known coordinates in the vessel.**

Summarized, two basic items are necessary for the development of a geometrical calibration system for bolometry diagnostics:

- An energy source radiating in the spectral range of the bolometer detector with sufficient power to generate an acceptable high S/N ratio.

- A manipulator which can move and orient the radiation source precisely and whose position and alignment is known in relation to the experimental vessel.

The following sections will define the appropriate requirements for a LOS calibration device. Besides the fundamental physical requirements, criteria which facilitate the technical realization in ASDEX Upgrade, will be discussed.

### 3.1.1   Manipulator

The essential part of the setup is the manipulator which will be used to move the radiation source in the three dimensional space of the expected LOS area. Principally, the final complete assembly should be able to be operational in a laboratory environment and in ASDEX Upgrade.

The functional properties, such as the measurement accuracy, can be different depending of the operation environment, but this is an issue which will be evaluated later in this chapter, see section 3.5. The essential physical criteria of a suitable manipulator are listed in the following:

- Absolute position accuracy should be in the mm-range. As a matter of course, this value will influence the overall measurement accuracy of the LOS calibration tool. Due to its importance, this issue will be discussed in detail in Section 3.1.3.

- Adequate load capacity of the manipulator to carry the weight of the radiation source including optional optical components with supports.

- Get in and out of the vessel through the standard opening, the A-Port, a radially aligned port of 0.9 m length, 0.8 m height and 0.4 m width.

- Capability to fit and maneuver in the limited geometric space of ASDEX Upgrade, e.g. in the divertor, while enabling a significant work area, see the Figure 4.22 of the poloidal cross-section.

- The manipulator must be able to work independent from the normal floor alignment in a perpendicular or in a parallel alignment to the gravitational force, i.e allowing ceiling- or wall-mounted operation.

- Weight of the manipulator and generated leverage forces are not allowed to exceed the limits of the vacuum vessel wall bolts. An installation of new bolts is unwanted from the vessel operators and due to space restrictions hardly possible. This means that a perfect form closure mounting device will have to secure a stable and fixed orientation.

- All items, parts and cables from the manipulator, which are in the vessel, have to comply with the Low Voltage Directive (LVD[1].) due to European Union regulations [119] on work in closed containers [120].

Following criteria should be fulfilled as best as possible because they would significantly reduce build, test and installation efforts. Though they are not considered as show-stoppers if the selected manipulator does not comply with all these capabilities:

- The manipulator should be as flexible as possible: For a typical industrial joint-arm robot this means for each joint a minimum operating angle of 120°.

- The necessary floor space, respectively the manipulator foot, should not be much larger than a factor of 2-3 compared to the arm diameter, as otherwise the starting position of a flexible mounting device will be very limited (see Chapter 3.2.1). This also applies for components of the arms which should not be made of complex geometric structures like e.g. some small pallet robots.

---

[1]Low Voltage Directive (LVD) 2006/95/EC, 12. December 2006

- CAD data should be available for a virtual commissioning allowing the simulation of the implementation of the system before final procurement.

- Virtually unrestricted access to control the system, easy to use programming language and as far as possible open network connectivity for the implementation of a remote control system. In that regard, a system limited to classic integration with a Programmable Logic Controller (PLC) with a Supervisory Control And Data Acquisition (SCADA) system like e.g. Siemens Simatic would not be ideal.

- It would be advisable, if the forces that the manipulator is able to apply on other components can be restricted, in order to limit possible damage of devices in the vicinity.

- Due to the lack of experience at IPP concerning commercial robotics and manipulators, it would be advantageous if the company which provides the manipulator offers basic training and engineering support during the start of the project. Being in close proximity to IPP would be a benefit, to simplify and reduce costs of maintenance and possible repairs.

It is becoming clear that the requirements to operate such a device in situ, are much more stringent than in the laboratory, alone on account the fact that a laboratory environment provides more space. Thus, the parameters of the manipulator will be mainly defined by the requirements given for the vessel operation.

Because of the high fraction of automatism especially in the heavy industries, e.g. automobile industry, robotic technologies are widely available. There is a large choice of robots available from over 10+ robotic firms worldwide. At the time of the beginning of the project[1] an assessment of different manipulators available on the market was conducted. In Chapter 3.2.1 the selected manipulator is described.

### 3.1.2 Radiation source

The radiation source is needed to uniformly irradiate the bolometer camera. For the selection of a radiation source, a broad-band light source, which represents the same spectrum and power as emitted during a typical fusion reaction in a tokamak, is the most appropriate. However, such a radiation source (apart from a fusion plasma itself), simply does not exist.

For the selection of a proper radiation source, the following requirements need to be considered:

- Radiating in the spectral range of the detector, preferably in a range of high energy absorption of the detector, alternatively this can be compensated by providing sufficient output power.

---

[1]The ITER Bolometer BMBF Project started in Nov 2008.

- Parallel radiation (low beam divergence) of the source is required to determine its exact orientation during the measurement procedure.

- Radiation source diameter has to be large enough to cover the entire surface of the aperture entrance of the bolometer.

- Uniform power output, constant within $\Delta P \leq 1 - 5\%$. This value is determined so that the measuring uncertainty is influenced to the smallest degree possible.

- Complete setup must not exceed the maximum load limit given by the manipulator.

- The output power and consequently the power, which is deposited on the absorber has to be adjustable to adapt the power density when working with different experimental set-ups. This allows to carry out the measurements in a optimal S/N ratio.

- Light source shall not add usability constraints such as a long time to stabilize or a short lifetime resulting in regular source exchange.

There exists a wide range of commercial light sources for calibration tasks. Usually, quartz tungsten halogen lamps are used as a general light source for visible and NIR (Near-infrared) applications. Deuterium (D2) lamps can produce highly stable, reproducible and intense UV (ultraviolet) radiation. Noble gases (Neon (Ne), Xenon (Xe) and Krypton(Kr))-lamps connected via optical fibers can provide line radiation in similiar wavelength ranges with a high intensity. A fully wavelength tunable light source like an optical parametric oscillator (OPO) would also be desirable. Combined with an integrating sphere, any radiation source can generate a uniform output. However, these set-ups are too heavy and too large for the manipulator and probably very expensive as well.

Laser sources can serve most of these attributes through excellent efficiency and high reliability with the disadvantage that they typically provide only a very narrow frequency range. The applicability of the results from one measurement wavelength of the laser to other relevant frequency bands of the bolometer detector will pose an additional challenge. Nonetheless, the decision was made in favor of a laser setup (see Section 3.2.2). Therefore, the results will have to be interpreted carefully. The arising implications will be treated as part of the discussion in the measurement results (see Chapter 4).

### 3.1.3   Absolute position calibration

The absolute positions and orientations of all parts of the system have to be determined prior to measurement. Otherwise, global statements of the alignment of the LOS can not be made. All diagnostic components in a tokamak experiment are usually oriented towards a special vessel coordinate system, the Torus Coordinate System (TCS) or the ASDEX Upgrade CS (described in Chapter 4.2.4).

Manipulators usually offer the possibility to calibrate themselves, collectively referred to as self-calibration. They can determine their position with respect to an internal system. This ability is used for certain manipulators which loose their calibration values once they have been shut down, comparable to the resetting of a capacitive caliper. However, this calibration values are then only stored in the internal software and usually are not accessible form outside besides being relative values. This self calibration should not be confused with the absolute position calibration performed with IBOROB because this function is limited on the manipulator itself and does not allow to measure additional external points.

Thus, at least one initiatory global calibration with an external system will have to be performed. ASDEX Upgrade is an experiment under continuous development. After each shutdown many systems are changed and upgraded, a regular external recalibration is necessary anyway. Moreover, points in remote and difficult accessible areas have to be reached, such as the bolometers in the divertor area, so a small device with the smallest possible measuring tip would be required.

For these purposes, the portable CMM *"Faro Arm Platinum®"* [121] is widely used at ASDEX Upgrade. It was used recently for the installation of a fiber-optic sensor in order to verify its correct position [32] and is used on a regular basis during machine maintenance and diagnostic upgrades [116]. The CMM can determine its position in the TCS by measuring certain predefined points which are evenly distributed in the experimental vessel. Afterwards, conclusions towards the orientation in respect to the magnetic flux surfaces, separatrix or other scientific important positions can be drawn. For the construction of W7-X[1], it is widely used by the metrology team [122]. The FaroArm, is based on a multi joint, manually positionable arm which allows to measure points in a three dimensional environment with a volumetric accuracy of up to $\pm 0.086$ mm. Ball probes with different lengths and diameters can be mounted to the arm to allow the flexible access in narrow areas.

Here, it will be used to determine the bolometer head positions in reference to the manipulator CS. Additionally, it includes the software *"Cam2Measure®"* which provides many features which simplify its application. For instance, a plane or a circle can be constructed out of 3 measured points and the position of an object in space can be calculated while indicating the achieved measurement accuracy.

## 3.2 Description of the ITER bolometer robot test rig

The complete system which was finally built was named ITER Bolometer Robot Test Rig (IBOROB). A schematic diagram of all components of IBOROB is shown in Figure 3.2. It consists of a KUKA robot as a manipulator, a laser with an attached beam expander as a radiation source, a remote control interface the electronics of the data acquisition and the *FaroArm*

---

[1]Wendelstein 7-X (W7-X) is an experimental stellarator currently being built at IPP Greifswald, Germany.

used as a supporting tool. The principal tasks and responsibilities of the main components, manipulator, radiation source and remote control, are listed in the diagramm as well. The mutual dependency is represented by solid lines. The dashed lines indicate the elements which are important for the data exchange.
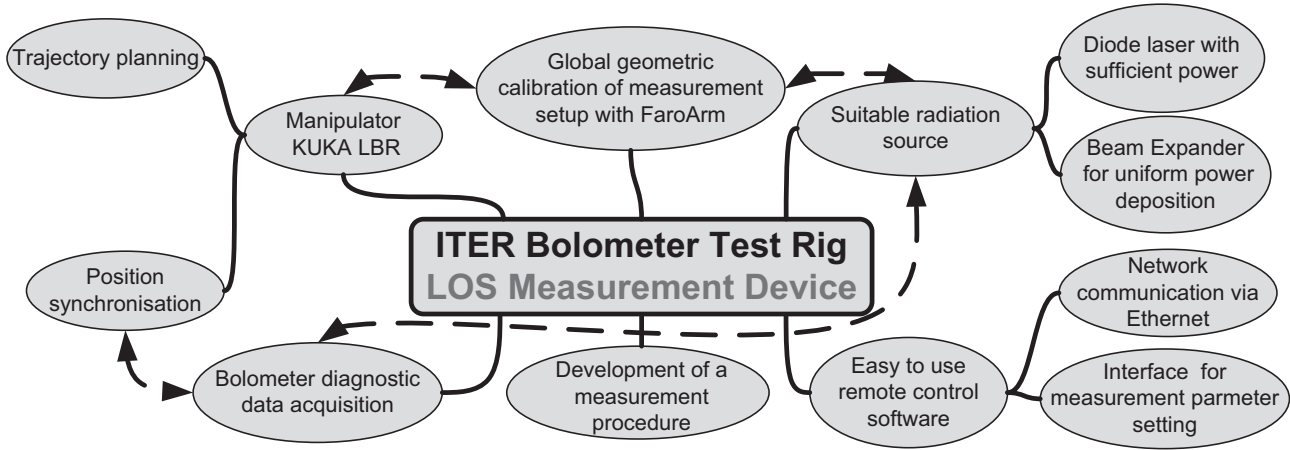


**Figure 3.2:** Diagram of the IBOROB system. The dotted lines indicate between which components data has to be transmitted.

In the following sections of this chapters, all components for IBOROB will be presented together with the reason behind the choice and the main criteria for their selection. The first presented part will be the robot.

### 3.2.1   KUKA Light Weight Robot

The Light Weight Robot (LWR) of the version 4 from the German robot company KUKA[1] was choosen as a manipulator. The LWR is based on a 7-axis actuator design and can be seen on Figure 3.3. The Figure shows the robot and the KUKA Robot Controller (KRC), which is a industrial style computer including the power supply for the robot. On top of the KRC is the KUKA Control Panel (KCP), a remote hand control interface with a small screen including the main function keys, such as enabling the drives, starting and stopping of programs and manual position control. Custom made cables connect all the components. The LWR meets all stringent conditions demanded in Section 3.1, especially the geometrical ones, and addresses most of the usability aspects. As the name suggests, the robot has only a weight of 16 kg and simultaneously offers 7 kg of load capacity which makes him very portable and flexible, an advantageous property for the transport from one laboratory to the other. The robot can be mounted and operated in any orientation which was an important requirement to perform measurements in ASDEX Upgrade.

The positioning accuracy is certainly an important requirement for a manipulator. The manual indicates a repetition accuracy of $\pm 0.05$ mm (ISO 9283) and KUKA staff made the statement

---

[1]The company KUKA was named by the German company founders in 1898: Keller und Knappich Augsburg.

that the absolute accuracy is $\pm 1\,\text{mm}$. The positioning accuracy is usually not specified for robots and depends on the accuracy of the calibration process. Both values have been verified by the Institute for Process Control and Robotics from the University of Karlsruhe which used the LWR for the development of a computer aided surgery of the human skull [123]. Having a reference for these parameters is important, in particular since robot manufactures rarely indicate the absolute accuracy due to the fact that it depends on the application environment and usually leads to poorer values. In what way the manipulator accuracy influences the overall IBOROB system will be discussed in the final Section 3.5 of this chapter.
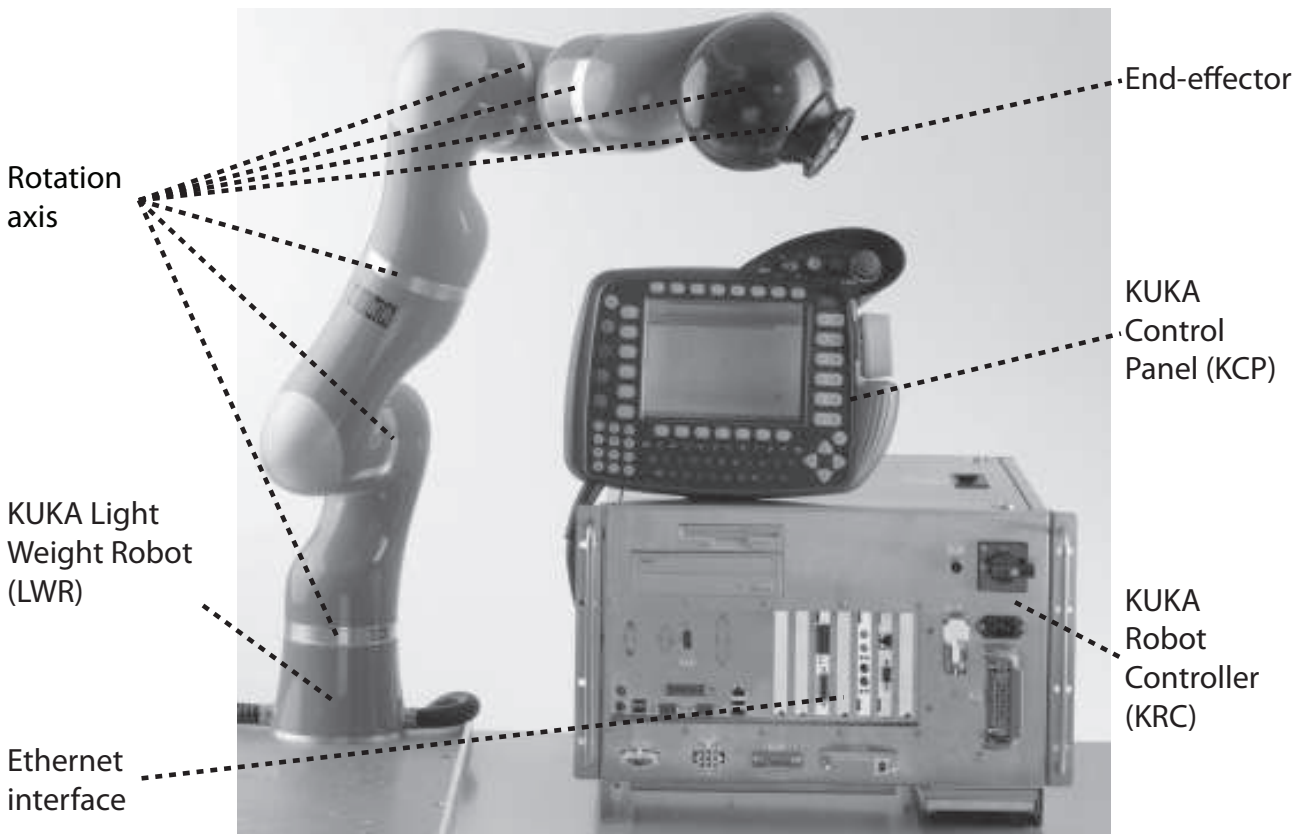


**Figure 3.3:** The KUKA Lightweight Robot (LWR) on the left with KUKA Robot Controller (KRC) and KUKA Control Panel (KCP) on the right (image from [124]). The seven rotation axis, the end effector and ethernet interface are indicated.

The LWR is not an ordinary joint-arm robot, given that he has seven joints and not as usally six, which would be sufficient degrees of freedom allowing to move and orientate in all directions. It allows the robot to e.g move the elbow around an object or reorientate the axis without affecting the hand position and orientation. This kinematic redundancy was not a must requirement for this application but it can be very useful when operating in a crowded space like an experimental fusion reactor. Generally the robot is smooth and slender, without any disturbance contours, e.g. a large foot, thereby the risk of interference problems with other objects for the integration in the vessel is reduced.

The ease of handling and programming the robot benefits from the teach-in capability by moving the end-effector by hand in a force-controlled mode. The teach-in positions can be

recorded, simplifying joint trajectory testing and helping to program the movements. The joints of the LWR, respectively the elbow of the robot, can be adapted to the environment, e.g. twisted manually in an optimal angle so that the next movement can be done to its maximum extension. In the past, such work had been solved by sophisticated simulations or more time consuming try-outs. This ability paid off in particular during the short time slot in which the measurements of the ASDEX Upgrade bolometers were conducted.

The LWR is widely used in the robotics research landscape due to open communication and control interface [124]. KUKA developed for this robot a communication standard that enables the exchange of data via a UDP or TCP/IP interface called Fast Research Interface (FRI). It allows the direct low-level real-time access of the robot controller, including a complete parameter set for all available control architectures (Force-Control, Stiffness-Control, Position-Control) and the direct setting of position coordinates is possible at a rate up to 1 KHz.

Most standard commercial off-the-shelf robots are integrated into production lines via a separate Programmable Logic Controller (PLC[1]) which usually does not allow to change internal parameters and only start or stop preprogrammed code. This can be ideal for industrial applications, but for a project in development stage a more open interface is preferred. Furthermore, we would need additional hardware to connect a PLC based robot with the bolometer electronics. The FRI can be run on a remote PC which is connected via Ethernet to the KRC and can therefore easily be integrated in the existing network of the laboratories or the experimental hall of ASDEX Upgrade.

All in all, the KUKA LWR was the only manipulator at the time of the procurement in 2009 that would allow to develop an in-situ measurement and calibration tool for the bolometer LOS in ASDEX Upgrade. The key advantage of the LWR to other robots at the time of the procurement, the integrated force and torque sensor which allows an impedance control over the torque sensor feedback, was not a necessary capability for us. But in terms of robot size, flexibility, connectivity and accuracy the robot is state of the art for our application. Interestingly the application of the LWR for *"Research outside robotics field: [...] e.g., robot is used to automate measurements"* is mentioned in one of the first publications of the developers [124], which describes in general terms the objective of the robot in this work.

### 3.2.2   Laser and beam expander

As a radiation source, a single-Mode diode laser 638 nm (red) version of the iBeam smart model familiy from *TOPTICA Photonics AG* was selected. The specifications of the laser are shown in table 3.1.

The laser offers a Gaussian power distribution by the transverse electromagnetic mode: $TEM_{00}$, sufficient power up to 100 mW, a superior pointing stability (75 µrad divergence for an estimated

---

[1]In Germany known as SPS (Speicherprogrammierbare Steuerung).

**Table 3.1:** Specifications of Toptica iBeam smart 100 mW, 638 nm laser. Only the specification necessary for the IBOROB system are shown. Data from the manufacturers manual [125].

| Specification | Parameter |
|---|---|
| Spatial mode | $TEM_{00}$, $M_2$ |
| Beam diameter (typical at $1/e^2$) | 1 mm |
| Divergence (typical) | < 1 mrad |
| Beam shape circular, ellipticity | < 10% |
| Power stability (drift over 48 h at $\Delta T \pm 5°$) | < 0.5% |
| Pointing stability | < 5µ$rad/K$ |
| DC input requirements | 12 V / 2 A |
| Operating ambient temperature range | $15°C - 40°C$ |
| Dimensions (L×W×H) | $100 \times 40 \times 40$ mm$^3$ |
| Weight | < 250 g |
| Max. heat dissipation (baseplate at $50°C$) | < 12 W |
| Digital communication interface | RS-232 ≤ 115.200 baud |
| CDRH qualification | Class IIIb |

operating range of $\Delta T = 25°$ ($5°C - 30°C$) which corresponds to a maximum angular displacement of $0.0042°$). All physical specifications, such as a compact dimension of the laser including its driver electronics (the necessary current supply can be mounted externally) and the total weight correlate with the manipulator capabilities. The control of the laser can be realized through a RS-232 interface, a common standard for serial communication and transmission of data. Thus, the laser control does not require special programming or development of drivers and can be implemented easily in the LabVIEW control system, see Section 3.3.6. The remaining specifications like e.g. polarization, wavelength range, maximum analog and digital modulation bandwidth are not relevant for this setup.

The laser is classified by Center for Devices and Radiological Health (CDRH) in class IIIb because of an output greater than 5 mW which requires certain safety measures. The entire setup has to be checked by the local Laser Safety Officer who determines the appropriate control measures. Apart from basic protective equipment like laser protective eye-wear and laminated laser warning signs, an equipment lamp and an extra switch was inserted in between the laser. For the measurements performed in ASDEX Upgrade all vessel openings and ports have to be blocked to prevent any laser light from leaving the vessel. The primary entry port is closed with a shutter and sealed with a lock for the time of the measurement operations.

To generate a broad and parallel radiation source of a sufficient diameter for the bolometer aperture openings a beam expander was mounted in front of the laser. A fixed power beam expander from the company Edmund Optics [126] with 20x magnification was chosen. It has a focus mechanism allowing to generate a parallel radiation output. The laser beam with a diameter $\varnothing_{las-in}$ of $\approx 1 - 2$ mm (diameter visible to the naked eye) enters the 20x beam expander resulting in a diameter $\varnothing_{las-out}$ of 27 mm large laser beam which corresponds to the lens diameter.

According to the manufacturers information, the focus should be very precise maintaining the bore sight accuracy while changing the focus due to its non-rotating optics. However, a value is not given. During the calibration process and in order to obtain the overall measurement accuracy of IBOROB, this value has to be determined (see Section 3.4.1.1).

The mechanical construction of the laser and beam expander attachment can be seen in a CAD image in Figure 3.4. The last part of the robot arm is based on a spherical head (in black) within which the last rotation axis (here vertically aligned) is incorporated (compare to CAD Figure 3.1 of IBOROB in the laboratory). It is equipped with a standardized DIN ISO 9409 robot adapter plate on which the laser and the beam expander attachment can be mounted.
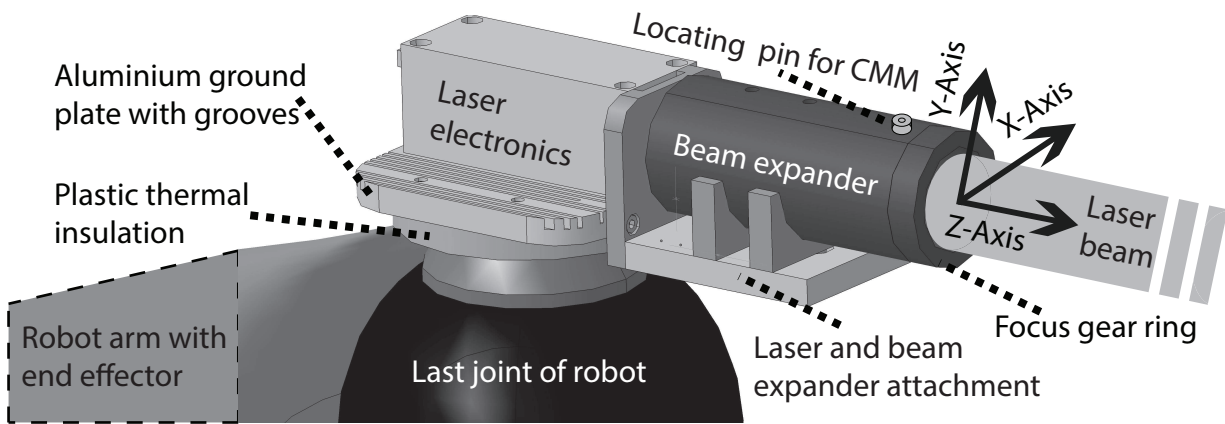


**Figure 3.4:** Laser and beam expander attachment mounted on the end effector of the KUKA LWR. Laser beam, focus gear ring of the beam expander, CS of laser and basic construction parts are indicated.

The laser and the beam expander attachment for the robot includes a thermal insulating plastic ground plate in order to avoid a thermal bridge between the laser electronics and the last robot joint motor. The operating temperature limit of the laser is $40°C$ and the robot joint can reach similar temperatures during normal operation. Thus, both have to be thermally separated. In particular when performing a measurement over a long period, it must be guaranteed that the electronic components don't overheat - and then switch off automatically. Therefore, in order to improve the heat dissipation, an aluminium ground plate of 1 cm thickness containing multiple grooves forming a heat sink structure is mounted in between the laser electronics and the insulation layer.

This aluminum ground plate serves also as connection to the beam expander attachment. It is bolted sideways to the rest of the attachment which consists of two semi circular holders serving as mounting brackets for the beam expander. They position the expander at the right position with respect to the laser aperture opening.

To define the orientation of the laser and beam expander device towards the robot flange (DIN ISO 9409 robot adapter plate) during assembly and dismantling, two locating pins are integrated in the bottom of the aluminium ground plate (not shown in the figure). Therefore,

once mounted, the position in respect to the robot flange is fixed with an exactness down to a few micrometers.

Nevertheless, the CS of the laser has to be recalibrated after each disassembly, due to the changing alignment in the range of a few degrees. It should be noted, that it is advantageous for the subsequent calibration procedure (see Section 3.4.1.1) to orient the laser in one of the robot end-effector axis, here the Z-axis. The origin of the CS and the exact orientation of the X- and Y-axis is irrelevant due to the central symmetry of the laser mode. For these components, all parts have been manufactured via turning and milling processes at IPP, the bolts are standard parts, hex socket steel M4 and M6 screws. In the next section the remaining system integration parts of IBOROB will be explained.

## 3.2.3   Mounting devices for the vessel and laboratory

In order to combine all components presented above, some additional parts for connecting and alignment purposes had to be developed. Different parts for the operation in ASDEX Upgrade and in the laboratory have been necessary. The following section will focus on the construction details of the mounting device for ASDEX Upgrade and the two different laboratory clamping devices. Finally, a brief insight in safety related procedures will conclude the "hardware" part of this chapter.

For the laboratory setup the robot is mounted via an adapter plate using screws on a brushed stainless steel table (see CAD Figure 3.1 in the introduction of this chapter or a photo, in Figure 4.1, in the results Chapter 4.2). The table is very heavy, its weight is approximately $100\,\text{kg}$ to keep the robot steady, with a minimum of sway during fast motions like emergency stops. The table is a $3\,\text{cm}$ thick perforated plate, with $10\,\text{cm} \times 10\,\text{cm}$ regular hole patterns, which allows an efficient and flexible positioning of all involved devices.

To position bolometer and collimator at an appropriate height and alignment; a profile rod can be screwed at various positions on the table. In order to allow a free individual orientation of the bolometer camera, two versions for the clamping element connected to the profile rod have been developed. A version with a fixed position and a version with a flexible ball joint. A CAD drawing of the two versions is shown in Figure 3.5. Subfigure A shows the ball joint clamping with the collimator prototype Version '11 and below, Subfigure B shows the fixed joint clamping with the following collimator Version '12. The aluminum profile rod and the cables which exit from the detector are indicated as well. The bolometer and detector is screwed via 10 screws onto the clamping element, so that it is possible to mount different collimator versions or to change the aperture configurations without affecting the orientation. The ball joint clamping was in particular advantageous to study and to perform experimental FaroArm measurements with different camera orientations.
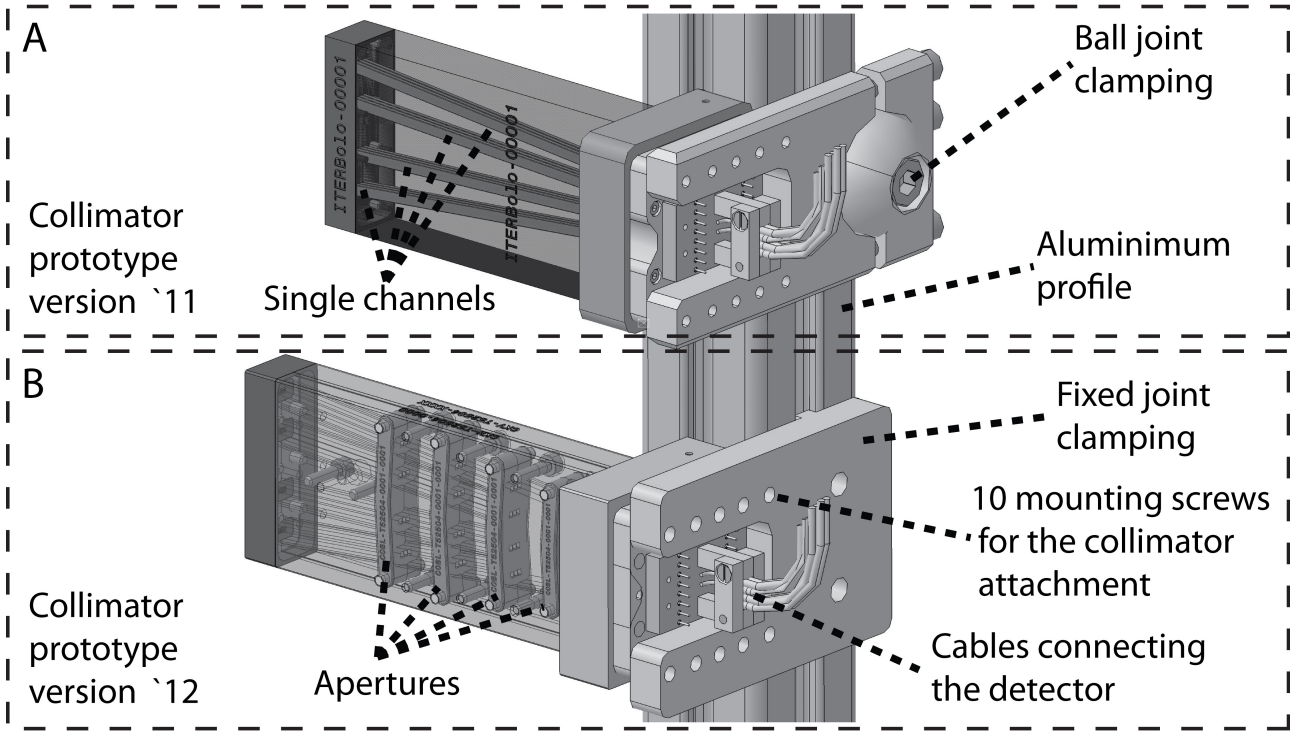
**Figure 3.5:** The two bolometer camera clamping elements for the laboratory measurement setup mounted on an aluminum profile rod. Version A on top is equipped with a ball joint and version B on the bottom with fixed horizontal clamping orientation. Cables, mounting screws and apertures are indicated.

For the operation of IBOROB in ASDEX Upgrade a custom mounting device compatible with the vessel properties had to be developed. However, there are not many places available to place and mount the robot. The vessel outer wall is occupied throughout with other diagnostic devices and equipment of an experimental fusion device such as heating systems, leaving little room for IBOROB. A recently used laser welding application [32] with a similar weight as the robot was mounted on a type of rail which passes circularly around the tokamak.

However, a mobile mounting device is not necessary for our application because most of the bolometer cameras are located in the same sector (see 2.4.2). The mounting has to be extremely stable and able to withstand strong mechanical forces which can occur during powerful accelerations, should allow a certain position flexibility in order to optimize the axis alignment in respect to the bolometer cameras and should not take up any more space in the vessel than is absolutely necessary.

The CAD image of the mounting device in ASDEX Upgrade can be seen on Figure 3.6. Three possible alignments are shown: Horizontal (A), vertical to the left (B) and vertical to the right (C). The device consists of three main parts: 1.) A U-shaped carrier, which is always horizontally aligned and adjusted to fit exactly the shape of the inner vessel wall. 2.) A circular base plate which can be rotated around the central axis in steps of 90°. These two parts are then screwed to the inner vessel wall through exactly that axis, realized by a large M14 screw. Thus, it can flexibly be placed in one of the 16 sectors (22.5° steps) of the vessel. 3.) The
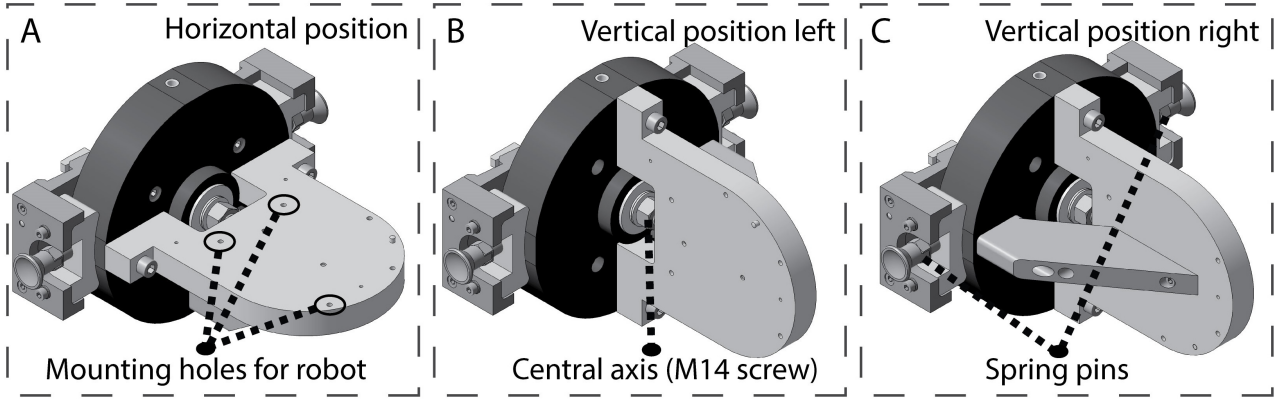
**Figure 3.6:** Isometric CAD view of the mounting device for IBOROB in ASDEX Upgrade. It can be mounted horizontally as shown in Subfigure A, or rotated in 90° steps e.g. vertically to the left or to the right, shown in Subfigures B and C.

robot support, a semicircular plate bolted to the circular base plate, upon which the KUKA LWR can be bolted. The U-shaped carrier has two spring pins on the side which have to be unplugged to allow the circular base plate to rotate. Mounting holes for the robot, the central axis and the spring pins are indicated in the figure as well.

The final decision concerning the orientation of the robot will be discussed in the results Chapter 4.2.4. A foto of the mounting device mounted in ASDEX Upgrade can be seen in Figure 4.18. All parts have been manufactured from stainless steel.

## 3.3   Software for remote control

In order make this "proof of concept"-system as comparable as possible to a future ITER system, the device has to be operated by remote handling, as autonomously and as simple as possible (see motivation of the work in Section 1).

Therefore, a software for the remote control of all components of the system has been developed using National Instruments LabVIEW (Laboratory Virtual Instrument Engineering Workbench). LabVIEW is a visual programming language which is a widely used program for computer controlled measurements and also used at IPP for the bolometer data acquisition [69]. The remote control software developed during this work, enables the remote configuration and remote control of all functions of the KUKA LWR without using the manual control (KCP). The laser can be toggled and the data acquisition and operation of the bolometer electronics can be controlled. A real time supervision of the position and status of the measurement procedure is made available and functions are integrated in a user-friendly graphic menu interface. On-line error diagnostics and troubleshooting can be performed remotely.

The remote access to the internal robot path planning was one objective of this work. Firstly, the approach was taken to use the FRI as described in Section 3.2.1. The FRI could certainly

provide this task, due to its low level access down to internal system parameters such as the control sample time. Many network and control interfaces, based on the FRI, have been under development and are still improved by large research associations (OROCOS [127] and OpenKC [128]), mostly focused on robotic control algorithms. However, due to the vast number of possibilities, this also involves a large complexity.

ImagingLab, an Italian (robotics) software company, released in 2012 a LabVIEW based network interface denominated *"Robotics Library for KUKA, Toolkit for Directly Commanding and Controlling KUKA Robotics from NI LabVIEW"* [112], which also covers the ability of remotely controlling a KUKA robot. Although the company had no experience with operating a LWR, the software was successfully brought into operation.

The library allows to connect a host computer to the robot via a TCP/IP Ethernet connection. Once connected, the user can permanently read and write into all essential variables (Boolean, integer, char, string) of the robotic system. It is slower, however, as the FRI (FRI Sample Time $T_{FRI} = 2\,\mathrm{ms}$, ImagingLab Sample Time $T_{ImgLab} = 100 - 250\,\mathrm{ms}$[1]), but still sufficiently for our application. The library gives access to the internal LWR measurement data such as the joint angles and relative positions in respect to certain coordinate systems. The robot status (Drives, errors, control mode) can be supervised and even performance data like the temperature of the joints or safety relevant parameters like overall speed limits can be accessed. If the type and the name of the variable are known to the user, full read and write access to complete data arrays and clusters, which are e.g. used for the description of coordinate systems, is possible.
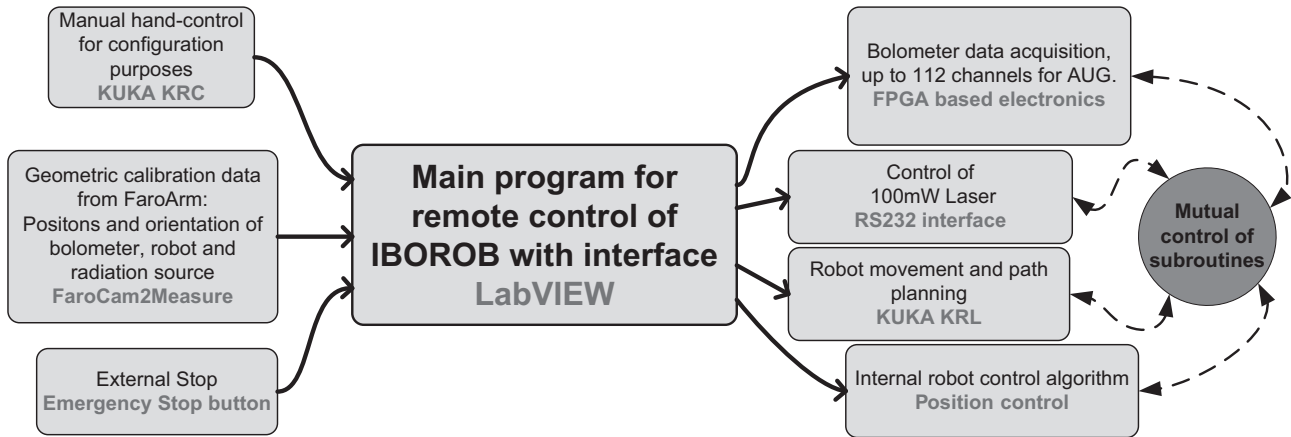


**Figure 3.7:** Diagram of main interacting software components of IBOROB. The input variables are on the left, the controlled software applications and programs on the right. The systems and interfaces used are marked in grey.

However, path planning and robot movement commands still have to be realized through a program in the KUKA Robot Control Language (KRL). The remote control interface will have to form a kind of symbiosis between the ImagingLab library and the KUKA KRL. A KRL program can not be remotely changed, transferred nor modified. But different programs can

---

[1]The sample time is not specified by the manufacturer, but was determined for our case experimentally. It depends approximately on the amount of Read/Write functions used in parallel, see Section 3.3.4.

be loaded, started, stopped and triggered by other external events supervised by a LabVIEW application. Thus, a variable modular program was developed. The parts will be explained in the following sections.

The diagram in Figure 3.7 shows an overview of the developed IBOROB software parts. Four objects are interacting with the main control program, which works as a stand-alone software program: It has to control the laser, trigger the Field Programmable Gate Array (FPGA) based Data Acquisition of the bolometer detectors, perform the global path planning and control the robot movement. As input variables the geometric data sets from the FaroArm have to be processed. The emergency stop still has to be allowed and introduced externally. The following sections will explain all parts including the post processing of the measurement data.

### 3.3.1 Robot movement and path planning

Most of the robots used in industry, including the KUKA LWR, are programmed via an industrial robot language. Usually each manufacturer has developed its own version. The KUKA company developed the KUKA Robot Control Language (KRL) which can be optionally remotely controlled by a PLC when operating with several machines or additional tools, such as a gripper or here a radiation source (see Section 3.2.1). The KUKA programming language is a high-level procedural programming language [129,130] which supports functional programming. The language focuses on usability over optimal program efficiency shown by the fact that it is a directly interpreted language and does not require a compilation. During the execution of the program a pointer shows the position of the program flow, which makes it easy to understand the course of actions.

The robot can be operated in two main modes: The automatic mode, where the drives[1] are engaged, and the manual mode which is used for testing or programming purposes. Here, a KRL program which is running in the automatic mode was developed containing all robot movements necessary for the measurement and calibration of the LOS. The motion of the robot's joints, the end effector or used tool (here: the radiation source) position can be described in different coordinate systems. Thus, positions and orientation of the tool CS can be freely set with respect to different CS. The internal robot control calculates then the joint angles and optimal intermediate positions. The IBOROB program is organized as follows:

The sequence of each movement and the principal direction of the movement is predefined but the variables and CS frames are empty and defined and filled by the remote control. A CS frame, which is denominated as a type `E6POS` variable is an array of `REAL` values which contains two 3x1 vectors: `X,Y,Z` for the position and `A,B,C` for the orientation[2]. The same applies for a joint frame, which is defined by a 7x1 vector, due to its seven axis (`A(X)`): `A1,A2,A3,A4,A5,A6,E1`[3].

---

[1]"Drives" is a common term used by KUKA for the motors of a robot [129].

[2]The KUKA CS are defined as following: X-Axis (C-Rotation), Y-Axis(B-Rotation), Z-Axis(A-Rotation).

[3]The seventh axis is not a standard in robotics, therefore denominated as "Extra-Axis" `E(X)`.

For the movements specific commands of the KRL are used, e.g. `LIN REL E6POS(1)` for
`E6POS(1)=(0,0,0,10,0,0)` means performing a linear movement, i.e. interpolating a straight
line between the position and the one given by `E6POS(1)` and rotating the Z-axis around $+10°$
while maintaining all other positions and orientations. This is just one example of the used
instructions, more details as well as other movement types, can be found in the manual of the
robot, the programming language documentation and previous performed work [131].

### 3.3.2   Implementation of the laser control

To enable a fully automatic measurement it was necessary to implement the laser control in
the LabVIEW application as well. The Toptica iBeam smart family of single-mode diode lasers
can be configured and controlled through a RS-232 (115.200 baud) communication and via a
COM/TTY port driver. LabVIEW provides standard software libraries for these connections.
Toptica provides a list of ASCII line commands which have to be communicated to the laser,
e.g. : `la on` means to switch the laser on and `pw 50` to set the laser output to 50 mW. Sending
the corresponding commands makes the electronics perform the task. Two principal properties
had to be improved, the time delay and the overall code stability:

- A significant time delay of about $100 - 200$ ms exists between sending a control message
  and the final execution. The provided examples from Toptica showed the same delay,
  therefore an inefficient programming structure can be excluded as the reason of that
  problem. Given that it is important for the application not to perform measurements in
  an undefined status of the laser, a receipt acknowledgement was added. After each new
  command, the status of the modified parameter is interrogated and therefore verified.

- The laser electronics or the RS-232 connection were not 100% stable. During some lab-
  oratory experiments the laser control crashed - the laser didn't react any more on the
  commands. The RS-232 connection had to be closed and reconnected to establish control
  again. For such cases, a watchdog was implemented which restarted the system after a
  certain time. Due to this unreliability, the time delay as explained above, could not be
  compensated by phase shifting the command in advance. Especially for the measure-
  ments in ASDEX Upgrade the system needs a high reliability because of the limited time
  available for in-vessel experiments.

The dimensions of the ASDEX Upgrade experimental hall are large, the distance between the
vessel and the DAQ computers are about 50 m and the RS-232 cable lengths are limited to
$\approx 15$ m. There is no clear definition of the cable length by the standard (ANSI EIA, TIA-232,
1997), however a maximum capacitance is defined, which results for normal non low-capacitance
cables in a maximum distance $\approx 15$ m. For the ASDEX Upgrade measurements a RS-232 -
Ethernet transceiver was integrated in the cable connection between laser electronics and remote
control computer. The Ethernet transceiver translates the serial data to Ethernet packages and

sends them over an existing Twisted-pair CAT-5 peer to peer connection, thus allowing larger connection distances.

### 3.3.3   Integration of the electronic data acquisition

The foil bolometer data acquisition system at ASDEX Upgrade is based on a National Instruments PXI system running Microsoft Windows with LabVIEW 2009. The basis of the PC is a rugged industrial-style based platform which contains a multi-core embedded controller in a 8-Slot 3U PXI Express Chassis. Additionally, it is equipped with four NI FlexRIO FPGA Modules cards in the Eurocard format. Each module is used to measure up to 32 channels via a Virtex-5 FPGA. Furthermore, it offers the possibility of real-time parallel signal processing which is an important capability for tomography [69].

The digital in- and outputs are connected to custom-built electronics which in turn are connected via shielded connectors and cables to the bolometer cameras. The electronics consists of commercially available 16 bit digital-to-analog converters which provide the necessary source current for the measuring bridge while simultaneously measuring the bridge voltage of the Wheatstone bridge of each bolometer channel.

For the operation at ASDEX Upgrade, the application is started and configured by the responsible bolometer operator. During an experiment, the data acquisition is started by one of the global ASDEX Upgrade trigger signals. For IBOROB, the data acquisition part had to be integrated into the main LabVIEW control application, as seen on the diagram of Figure 3.7. The laboratory and ASDEX Upgrade version only differ in terms of number (Four channels in the laboratory and 112 for ASDEX Upgrade) of acquired channels and the used operating system, Windows XP for ASDEX Upgrade and Windows 7 in the laboratory, but are in principle the same. The data acquisition works in the following way:

The process of calibration ($\kappa_{heat}$ and $\tau_{ct}$) and measurement is completely integrated on the FPGA in VHDL[1] automatically from the LabVIEW flowcharts programs. For the high-speed buffered data acquisition it uses DMA[2] transfers by using a FIFO architecture which has the advantage of allowing the FPGA to use the host RAM as if it were one of its own. Thus, transferring large amounts of data in a multi-channel construction is possible.

When no radiation is incoming, the bridge is balanced and no bolometer bridge voltage can be measured. As soon as radiation is impacting the detector it is heated up and a voltage difference can be observed. For the calculation of the absolute value of the incident power the voltage value is further processed with its derivative over time and the material constants (see Section 2.1.3 and [45]). In this work, for the measurement of the transmission of bolometer cameras, only the bolometer bridge voltage is used.

---

[1]VHDL = VHSIC (Very High Speed Integrated Circuits) Hardware Description Language.
[2]Direct Memory Access.

### 3.3.4   Mutual remote control of subroutines

The principal task of the LabVIEW remote control program is to act as a master program which starts and stops all necessary subroutines needed for the measurement procedure (see Figure 3.7). The three main parts of IBOROB (laser control, robot movement, and the bolometer DAQ) have to be synchronized and put in their correct order. The input information from the control interface (see Section 3.3.6) is used for logical decision making and branching to different sections of the program. For instance, it has to be ensured that the laser has already been switched on for a certain time before the DAQ acquires data.

The main function used of the ImagingLab Robotics Library for KUKA is a Read/Write function block which gives access to all internal variables of the robot system. The empty positions and CS frame defined in the robot control language (see Section 3.3.1) are filled with values according to the requirements. But only setting the position variables of a predefined movement procedure would not offer the desired flexibility. Thus, the execution of these functions is made dependent of some conditions (position and alignment of the robot) which can be defined by the LabVIEW control interface (see Section 3.3.6). `FOR` or `IF` loops can be started or stopped by changing their conditions.

Most of these case distinctions are realized by several boolean (`BOOL`) and integer (`INT`) variables which indicate the status of its respective subroutine. For instance, there is a boolean variable connected to the RS-232 laser control which is designated to switch the laser on (1) and off (0) again. This variable is changed to on when the robot arrives at the measurement position e.g after a certain step has been done. In a similar manner the execution of all other subroutines is controlled. However, due to the inherent uncertainty of the used TCP/IP protocol and the demanding requirements with respect to the process reliability (collision free movement) each network data transmission has to be checked. This means that after a variable has been transferred, the value is subsequently read and compared if it is equal with the sent value.

### 3.3.5   Data processing and filtering

For measurements where only relative statements are necessary and which are performed in quasi steady-state conditions, the bolometer bridge voltage can be used as a measure of the intensity of deposited power on the detector, which simplifies the DAQ. In particular during long measurements, the derivation (and integration) of the bolometer bridge voltage introduces additional noise and taking into account the relatively low power of the laser compared to the plasma radiation, the S/N ratio of the overall setup should not be further deteriorated.

To obtain a measure of the deposited power, the DAQ simply needs to wait a certain constant idle time in the order of a few thermal time constants of the detector to reach the thermal equilibrium. Herein, one thermal time constant of the detector amounts to approximately

100 ms. This is only possible when the power is not changing, hence the robot respectively the radiation source has to wait on the current position until this measurement has been successfully performed. Hence, the measurements are conducted in a steady state condition of the detector.

The DAQ is then triggered by the remote control program to acquire a certain amount of samples ($\approx 500$ samples) of the digitized signal and the average value is taken to achieve a signal smoothing and filter out any high-frequency noise. The value is then written into a buffer and written into a (ASCII[1]) measurement file after the whole measurement is finished. Further data processing is then performed with a numerical analysis computing program. Here, MATLAB (matrix laboratory) from the company MathWorks, has been used.

The radiation power detected by the sensor, can slightly vary due to the inaccuracies of the robot positioning (see Section 3.5). Larger disparities occur due to the different aperture opening sizes. The differences in absorbed power can be over 50%, e.g. for the aperture with and without the microwave grid (see Section 2.5.3). Therefore, a normalization to the maximum of each measurement is performed to ensure comparability of multiple measurements. It should be noted that the theoretical transmission is based on a normalized signal as well. Sometimes, the bolometer electronics had problems determining a correct offset of the measurement. For such cases, linear and time independent transformation of the signal, such as an offset correction or the removal of individual outliers, have been performed. The general characteristic of the LOS has not been influenced, only the meaningfulness and interpretability has been improved.

### 3.3.6 Control interface and measurement parameters

The LabVIEW based control interface allowing to set the measurement parameters and to supervise all other relevant parameters can be seen in Figure 3.8. The standard built-in libraries of controls and indicators have been used to generate a practical user interface. All parameters have been limited to certain input values, so that e.g for the robot motion collisions with other objects are avoided. For standard measurement scenarios untrained staff, such as students can use the test rig in the laboratory without supervision and the risk of creating damage to the components.

The settings are saved for each measurement in a separate ASCII measurement file to facilitate the post processing of the data. All of the main functions have been realized as sub-functions and can be stopped separately, e.g. for troubleshooting reasons. They are presented in the following:

1. **Laser Control:** Firstly, it contains the laser boot-up sequence which performs a test if the RS-232 connection to the electronics is working correctly. Then it allows the setting of the three operation modes of the measurement: Continuously powered on, operated synchronously by the robot position or a manual control for testing purposes. Finally, the

---

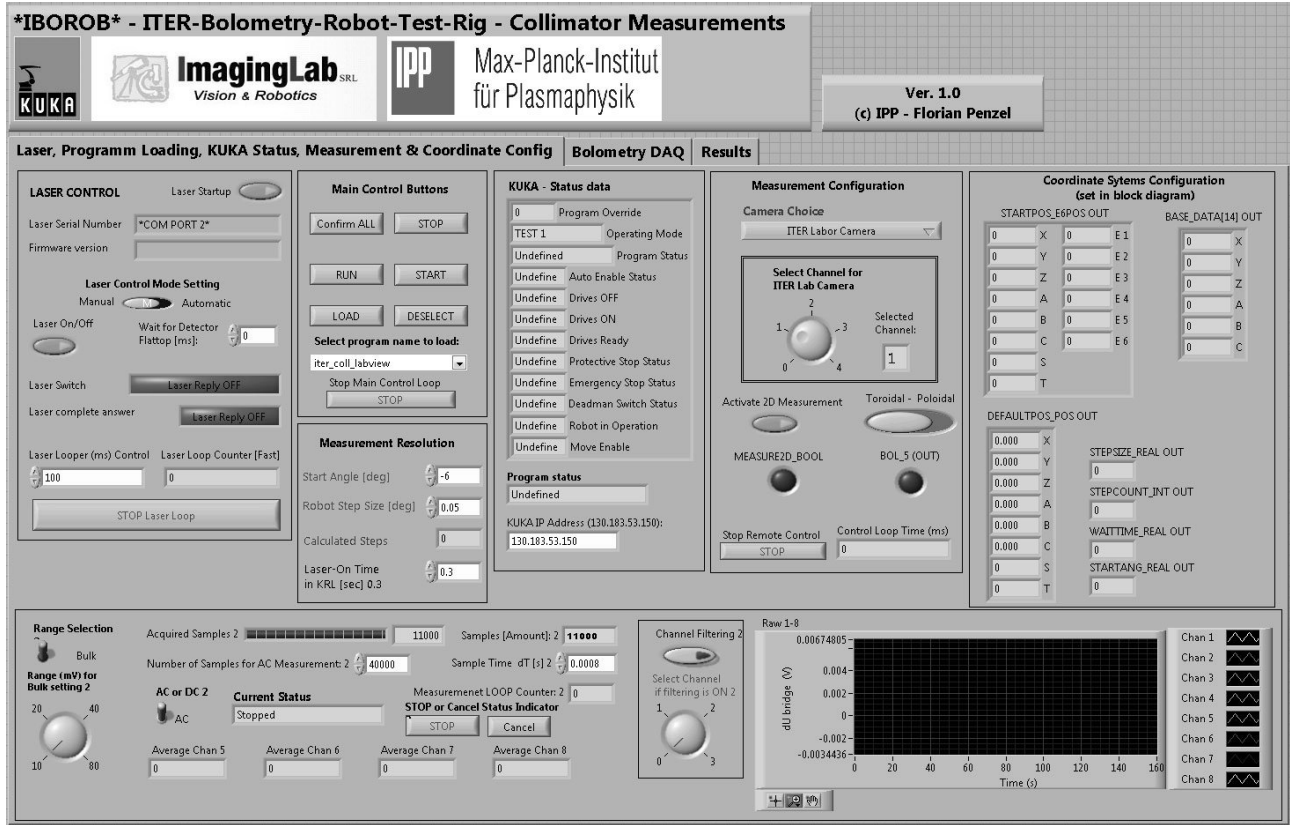[1]ASCII = American Standard Code for Information Interchange.

**Figure 3.8:** Screenshot of the control interface of IBOROB realized with LabVIEW.

laser power (1-100 mW) can be controlled. The status of the internal variables are shown by multicolored displays. More details of the technical realization have been explained in the previous Section 3.3.2.

2. **Main Control:** Once the robot is operated in automatic mode, which means the drives have been switched on and the brakes have been deactivated, the position respectively program control is transferred to the remote computer running the LabVIEW control application. Only the external emergency stop is still capable of influencing the status. Now, all primary functions such as program selecting, loading, starting, stopping and confirm (a manual confirmation command), can be controlled remotely. Here, it is mainly used to load the program for the laboratory or ASDEX Upgrade measurements.

3. **KUKA Status Control:** This part is mainly used for monitoring the robot status parameters like operating mode, such as overall speed joint or end effector speed limits, the drive status, the status display of emergency or deadman switch. The remote IP-Address of the robot has to be specified in this sub function as well.

4. **Measurement and Coordinate System Control:** The key part for the accuracy of the remote control application. The measurement parameters can be configured, such as the robot step size ($\delta_\xi, \delta_\theta$), toroidal and poloidal scan width ($\Delta\xi$ and $\Delta\theta$). For the laboratory setup the desired channel can be selected directly in the program. For the ASDEX Upgrade measurements different programs have to be loaded separately due to

the different pre-positions and orientations of the robot. The measurement procedure, one or two dimensional, can be selected. On the far right the internal CS data can be supervised and adjusted if the geometry of the setup is changed.

5. **Data Acquisition Control:** In this part the bolometer data acquisition can be monitored. Individual or also several channels can be supervised simultaneously. The sample frequency (Standard sampling time of bolometer electronics $T_{DAQ} = 0.8\,\mathrm{ms}$) can be determined, the range of the analog-digital converter $(10 - 20 - 40 - 80\,\mathrm{mV})$ and the total number of samples per robot position can be selected e.g. for measurements with the continuously powered on laser. The real time visualization of the measurement data has been recognized as an important tool to prematurely identify configuration errors without it being necessary to wait for the completion of the measurement period.

## 3.4   Measurement procedure and settings

After the description of the hardware and software parts of IBOROB, the measurement principle will be explained in the following section. As each measurement system has to be calibrated prior to measurement, the developed procedure of globally calibrating the measurement device and its components will be explained, too. Two different options have been used for the measurement of the LOS: The one and the two dimensional measurement procedure. Both methods will be explained next to the description of an efficient parameter choice of the measurement configuration software. Finally, the overall measurement accuracy of IBOROB is evaluated.

### 3.4.1   Absolute calibration of the system

To achieve a reliable and absolutely calibrated result for the transmission function, all system components of IBOROB have to be geometrically aligned in respect to each other: The internal robot CS, the orientation of the laser and the orientation of the bolometer camera. For a calibration measurement in the vessel, additionally the orientation of the vessel CS has to be known. For the positioning accuracy of the robot we depend on the manufacturer, assuming a correct operation of the robot including the separate axis calibration with the vernier scale (see manufactures manual [129]). Apart from that, the central objective is to know these orientations to the highest possible accuracy because they have a direct impact on the calibration accuracy.

Different measures have been taken: At first, locating pins and positioning holes have been mounted on the carrier frame of the laser and beam expander attachment (see Figure 3.4) and the mounting device (see Section 3.6) in order allow identical procedures for the measurement with the FaroArm. All components such as the mounting device have been manufactured respecting the highest tolerance grades of DIN ISO 2768 and certainly none of the optical components should be loose or slightly moving.

The laser and beam expander have been connected to each other on a carrier frame (aluminium ground plate with circular mountig brackets, see Figure 3.4). After the integration, these components have not been disassembled during the time of this work. But the connection of the laser and beam expander between the robot end effector had to be separated regularly for maintenance. The same applies for the adapter plate of the LWR of the laboratory setup, the bolometer clamping element and the mounting device for ASDEX Upgrade. These issues are prerequisites, however, do not contribute directly to the knowledge of the final alignment accuracy of all CS.

The external parts can be calibrated using the FaroArm Platinum, the laser and beam expander have been calibrated using a specifically developed method using the robot capabilities of the KUKA LWR software. They are described in the two following subsections.

### 3.4.1.1   Laser and beam expander orientation and position

Aim of this part of the calibration procedure is to determine the orientation of the laser CS relative to the robot CS. The origin of the laser CS (X,Y,Z) can be taken from the CAD drawings of the laser and beam expander mounting device. Due to the manufacturing accuracy it is important to emphasize that the aim is to determine the physical orientation (A,B,C) of the laser beam and not of the components housing. In robotics, the laser which is mounted on the end effector, corresponds to the TOOL CS. This CS is a variable coordinate system with the last joint center as its origin, oriented typically with the Z-Axis in the mounting direction of the end effector (see Figure 3.4). It can be changed manually in the tool settings or via the remote control interface (see Chapter 3.5).

Once the laser orientation is properly integrated into the TOOL CS, the internal robot control algorithms can take care of the exact positioning. Usually, these kind of tool calibrations are done by approaching the tool center point (TCP), which is mostly defined in the center of the tool, manually (with the KCP) to a fixed reference point from various directions [132]. The geometric parameters of the robot and the kinematic model are then used to calculate the TCP. For stationary or fixed tools this is a proven and successful method [133]; however the accuracy requirements are typically lower. For instance, in a standard weld application in the automotive industry a level of precision of a few degrees for the welding angle is sufficient.

The challenge in our setup is, that the laser has to be projected on a plane in order to be measured. For achieving the highest accuracy possible, an iterative method using the manual control functionality of the robot has been developed. The diagram in Figure 3.9 shows the calibration process: The laser is targeted on a wall at a large distance (here, $D_{calib} = 17\,\mathrm{m}$) from the robot in an experimental hall. At first, the laser is aiming on the start position. Then a rotation of the TOOL CS of 180° in its own CS around the z-Axis (expected orientation of the laser) is performed. In the Figure, the points are indicating the position of the laser on the wall.
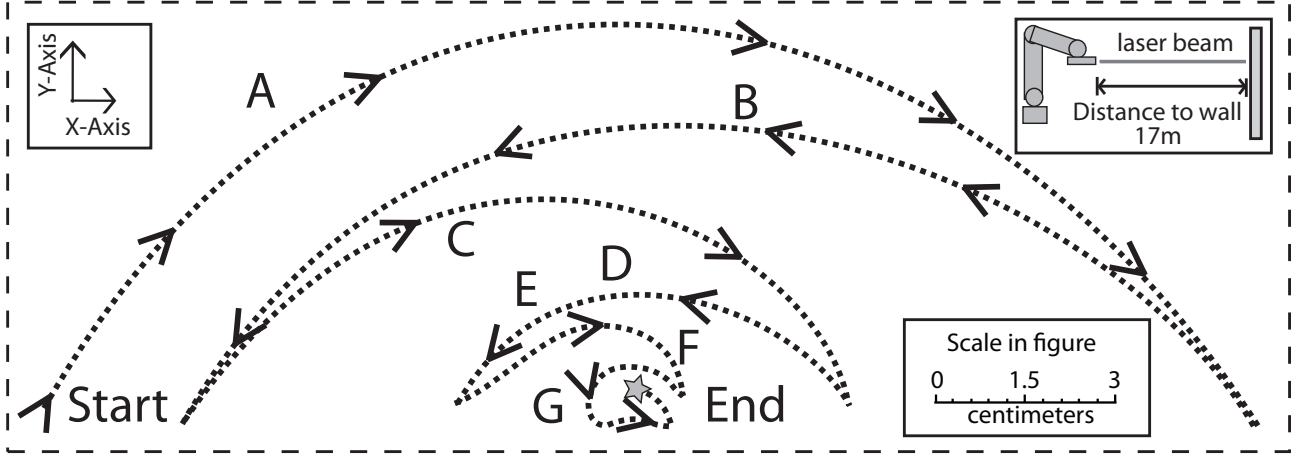
**Figure 3.9:** Calibration process of the laser CS: The TOOL CS of the robot is rotated around the X- or Y-Axis and systematically (A-G) adapted. First, a semicircle is projected on the wall until the kinematic accuracy of the manipulator is reached which can be seen by an undirected dithering (indicated by the star).

If the actual laser CS and the TOOL CS match, no movement of the laser apart from undirected dithering, determined by the friction, joint encoder accuracy and limitations of numerics of the robot, can be observed. For the Figure 3.9, a total deviation of about $\Delta_{calib}(A) \approx 0.33°$ is shown at the beginning (A) which corresponds to a circle with a diameter of $\varnothing_{calib}(A) \approx 20\,\text{cm}$. However, it can not be differentiated between wrong settings of either the X- or Y-Axis. By stepwise (A-F) adapting the parameters of the X- and Y-Axis and observing the deviations, the robot TOOL CS data can be approximated to the real orientation of the laser CS.

Finally (G), the laser CS is determined to the accuracy of the robot system, no circle can be observed anymore. The remaining area in which the laser spot fluctuates can be used as measure for the possible alignment accuracy in our setup. In the case presented in the Figure about $\varnothing_{calib}(G) \approx 1.2\,\text{cm}$ remain at the end which corresponds to an uncertainty of $\Delta_{calib}(G) \approx 0.04°$. This final value is noted for the overall accuracy calculations of IBOROB (see Section 3.5.1). During the repeatedly performed recalibrations (e.g. after transport of IBOROB), deviations of up to $\Delta_{calib}(A) \approx 1.5°$ could be observed.

This laser calibration process is performed with the beam expander focused on the wall to a small laser spot $\varnothing_{focus} = 1 - 2\,\text{mm}$ in order recognize the movements more easily. The focus of the beam expander is changed via a non-roating lens (see Section 3.2.2). Therefore it is necessary to know if the laser axis changes when the focus is adjusted because the measurements are performed in the defocused state $\varnothing_{focus} = 27\,\text{mm}$. The change in focus results in a deviation of up to $5\,\text{mm}$ at the calibration distance of $D_{calib} = 17\,\text{m}$ which is corresponding to an angular error of $\Delta_{focus} = 0.016°$.

#### 3.4.1.2  Robot orientation and position

The next step in order to globally determine the alignment of all IBOROB components is to measure the orientation of the robot CS with respect to its surroundings, i.e. either the CS of ASDEX Upgrade or that of the assembly in the laboratory.

For the operation in ASDEX Upgrade, the FaroArm is mounted next to the robot and determines the ASDEX Upgrade CS by measuring reference points evenly distributed all over the vessel. These reference points have been defined by the vessel engineers in the past and their accuracy cannot be checked. However, the points have proven their validity as reference for the physical orientation of all position-relevant diagnostics for a long time. The points allow to construct a CS which is used to make global statements of the LOS orientation. In the laboratory an external CS, e.g. the laboratory table or the bolometer camera housing, has to be defined.

To determine the orientation of the robot, the following method was applied: The robot is moved manually controlling the TCP of the laser and beam expander along the $\pm X$, $\pm Y$ and $\pm Z$ axis of the global robot CS. In parallel, the positions of the TCP are recorded by the CMM. Movements within a range of $\approx 300\,\text{mm}$ are sufficient not to influence the global measurement accuracy (see Section 3.5.1) too much considering the repeat accuracy of the KUKA LWR of $0.1\,\text{mm}$ ($\arctan \frac{0.1\,\text{mm}}{300\,\text{mm}} \approx 0.02°$). Depending on the available space in the laboratory, large axis movements up to $1\,\text{m}$ can be performed. The application of this method in the vessel is shown in the results Chapter 4.2.4.

The robot foot center can be determined by measuring several points around the circumference of the robot foot and projecting this circle on the base plate surface of the mounting device, using the FaroArm software. Together with the positions of the bolometers, which have been measured with the FaroArm as well, the data can be transferred to the remote control program. By targeting with the laser known external points, such as the bolometer aperture openings, it can be checked easily if the calibration was successful.

### 3.4.2  One dimensional measurement

The measurement of LOS works as follows: After power on of the system, the robot is set into automatic mode and the remote control interface of the robot is started. All components are calibrated as explained using the methods of Section 3.4.1. The CS of all required parts are determined with the FaroArm and transferred into the database of the remote control software. Once the network control is connected, the measurement settings are defined (see Section 3.3.6) and the measurement procedure can be started.

At first, the robot moves to a pre-position for which the orientation of each axis is specified and the laser is facing approximately the position of the bolometer. Next, the robot aligns the

laser CS perpendicular with respect to the reference CS and aims centrally on the aperture opening of the bolometer camera. The reference CS can be the bolometer CS in the laboratory (freely definable, e.g. by the collimator and camera housing) or in the experimental vessel it is the ASDEX Upgrade CS. Then, the start position of the measurement, which corresponds to the boundary value of the entire measurement, is approached by the robot. The operator can perform a brief check if everything goes well before the transmission measurements are started.

Performing a one dimensional measurement with IBOROB means that the LOS transmission from one channel is measured along the horizontal or vertical orientation of the bolometer camera, i.e. toroidal or poloidal orientation, respectively. If a measurement in one orientation is performed, the other orientation remains constant and should be selected so that the maximum transmission is met. Meanwhile, the laser remains always oriented on the aperture opening. In the following this is referred to as a poloidal or toroidal measurement. The center can be determined by interpolating a preceding coarse two dimensional measurement (see next Section 3.4.3) or alternatively it can be approximately determined with a manual movement of the robot and a simultaneous data acquisition.
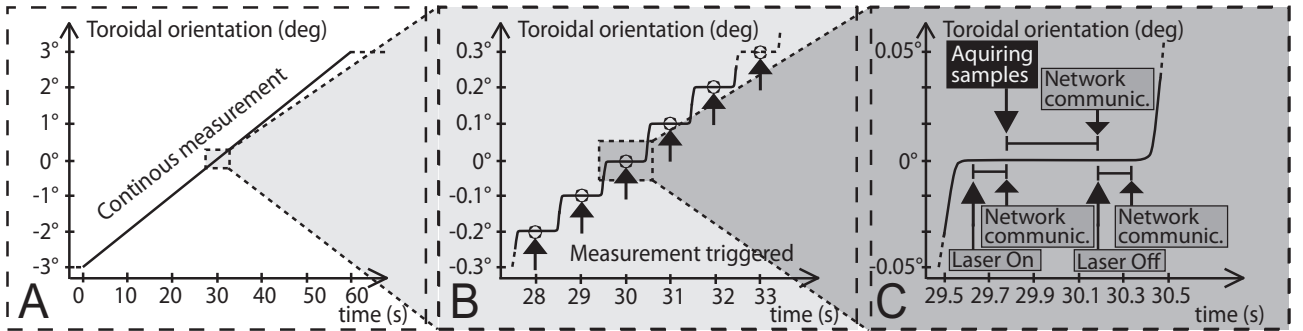


**Figure 3.10:** Subfigure A shows a diagram of a toroidal one dimensional measurement over the total time. Subfigure B shows an enlarged picture, the individual steps can be recognized. Subfigure C explains one step in detail, indicating laser control, network communication delay and sample acquisition.

Figure 3.10 shows a diagram with three gradually enlarged signal charts. Subfigure A shows a toroidal measurement which consits of a toroidal movement from $\theta(t_0 = 0\,\mathrm{s}) = -3°$ to $\theta(t_e = 60\,\mathrm{s}) = 3°$ over the time axis. The poloidal orientation is not changing, $\xi = 0°$. Subfigure B magnifies the area around $\theta(t = 30\,\mathrm{s}) = 0°$. It can be recognized that the robot performs incremental movements with a step size of $\delta_\theta = 0.1°$. After every step the measurement is triggered. Here, each measurement takes about $\delta t = 1\,\mathrm{s}$.

The process for each individual measurement is explained in detail in Subfigure C: As soon as the measurement point (defined by the orientation) is reached, the command to switch the laser on is transmitted. Due to the transmission delays and the following acknowledgement, referred to as network communication in the figure, some time passes by (see Section 3.3.2)($\approx 200\,\mathrm{ms}$). Moreover, it has to be ensured that the bolometer detector reaches thermal equilibrium (see Section 2.1). This is followed by the acquisition of a certain amount of samples, here shown for

500 samples (Amounts of samples * sample time = measurement time, 500 samples * 0.8 ms = 400 ms) which are then further processed by the DAQ part of the program (see Section 3.3.5) including the position data of the robot.

Finally, the laser is switched off and the next measurement position is approached. For measurements with low resolutions and short measurement times, the laser on-off control may be omitted (see section 3.3.6, operation mode 'continuously powered on laser'). At the beginning of the development of IBOROB, as the remote control interface had not been developed yet, measurements had been performed in this operation mode. In this case, only the corresponding DAQ was triggered on and off. But especially for the two dimensional measurement, which will be explained in the next section, this is not possible. It would lead to too large volumes of data which the bolometer DAQ cannot handle and the signal drifting over time would substantial deteriorate the signal.

### 3.4.3 Two dimensional measurement

The two dimensional measurement allows to determine the complete LOS transmission in toroidal and poloidal orientation. Figure 3.11 shows six diagrams which explain this procedure in detail.
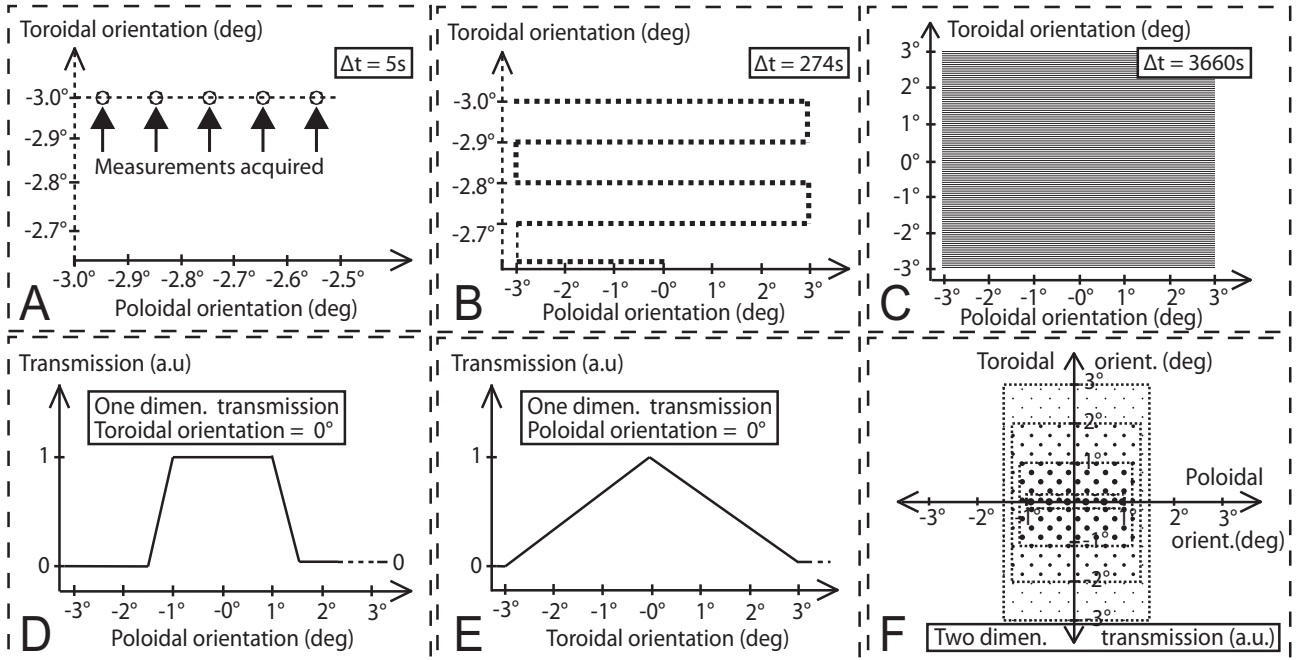


**Figure 3.11:** Subfigure A illustrates the incremental data acquisition during a movement in the toroidal orientation. Subfigure B shows the gradual movement in poloidal orientation after the completion of one toroidal measurement. Subfigure C shows the sampling of the whole measurement area. Subfigures D and E show an example of (theoretical) poloidal ($k_\xi(\xi)$) and toroidal ($k_\theta(\theta)$) transmissions. Subfigure F shows the corresponding two dimensional measurement results of $K(\theta, \xi)$ in a contour plot with the dot size indicating the transmission value.

Subfigure A shows the beginning of the measurement. Measurements are gradually acquired, as explained in Figure 3.10. But in this case, the robot starts the measurement at $\theta(t_0) = \xi(t_0) = -3°$. At first, the robot proceeds only in the toroidal plane. Then, one poloidal step is performed and the next toroidal plane is measured, see Subfigure B. Finally, the whole measurement area is covered with the robot, here with a resolution of $\delta_{\xi,\theta} = 0.1°$ (see Subfigure C). The necessary time periods for each Subfigure ($\Delta t$ in A,B,C) are indicated, and can be approximated according to: $1\,\mathrm{s}$ sample time per step for 60 toroidal steps * 60 poloidal steps + 60 repositioning movements ($\approx 1\,\mathrm{s}$) = $3660\,\mathrm{s} \approx 1\,\mathrm{h}$.

Subfigure D shows the poloidal transmission of an exemplary (theoretical) LOS, here in a trapezoidal shape for a toroidal alignment of $\theta = 0°$. Subfigure E shows the toroidal transmission for a poloidal alignment of $\xi = 0°$, here in a triangular shape. The result of a two dimensional transmission measurement is illustrated by the contour plot in poloidal and toroidal orientation. The dot size in the plot represents the normalized transmission value.

## 3.5 Assessment of measurement procedure

In the following, a brief evaluation of the measurement procedure will be carried out. Section 3.5.1 will show data to asses the overall measurement repeatably and Section 3.5.2 will derive the absolute angular measurement uncertainty of IBOROB.

For the following calculation has to be considered, that if errors are performed during the calibration process of the different involved components, it is difficult to deduce them later form the measurement results. Small errors have only an influence on the accuracy, not on the overall functioning of the device. Moreover, the calibration has to rely on parameters such as the definition of the internal origin of the robot CS.

### 3.5.1 Overall measurement repeatability

The measurement repeatability, the degree to which repeated measurements under unchanged conditions show the same results, has been determined for IBOROB. Multiple measurements with the same measurement settings for different aperture setups using BL7, BL0005, and BL0003 apertures of the Model '12 have been performed in order to obtain a certain statistical likelihood. The measurements are never exactly the same, the values are in a range around the true value or offset from it. The results can be seen in the table 3.2.

Five measurements have been performed with three different configurations in poloidal and toroidal orientation. Then, the standard deviation $\sigma$ has been calculated in order to show how much variation exists around the average value. $\sigma_{signal}$ is the value calculated when IBOROB moves in the area outside of the LOS and $\sigma_{noise}$ represents the variations calculated during

| Collimator Type | $\sigma_{total}(\xi/\theta)$ | $\sigma_{noise}(\xi/\theta)$ | $\sigma_{signal}(\xi/\theta)$ |
|---|---|---|---|
| BL7/ITERBolo-7 | 0.7 % / 1.3 % | 0.5 % / 1.0 % | 0.8 % / 1.3 % |
| BL0005/ITERBolo-9 | 0.4 % / 0.3 % | 0.3 % / 0.3 % | 0.8 % / 0.5 % |
| BL0003/ITERBolo-8 | 0.6 % / 0.5 % | 0.7 % / 0.4 % | 0.8 % / 0.8 % |

**Table 3.2:** Measurement uncertainty calculations for IBOROB in the laboratory setup.

the rest area where no significant transmission can be measured. $\sigma_{total}$ is the overall standard deviation. The worst standard deviation amounts to 1.3 %. Thus, no error bar will have to be added to the results because the repeatability error is within the range of the line thickness of the plots.

The reasons for the deviations can not be separated. The laser electronics could influence the constancy of the power output and the whole data acquisition part can introduce uncertainties: the D/A converter in the electronics, cables which absorb interference from electromagnetic noise and external radiation power fluctuations. In addition the position repeatability accuracy of the robot will have an influence.

### 3.5.2 Absolute angular measurement uncertainty

In order to estimate the measurement uncertainty concerning the absolute angular accuracy following issues have to be respected:

- The laser and beam expander orientation with respect to the robot CS could be determined with an uncertainty of $\Delta_{calib} \approx 0.04°$ (see Section 3.4.1.1).

- The difference between focused and unfocused laser amounts to $\Delta_{focus} = 0.016°$.

- The robot absolute positioning accuracy is assumed to be 1 mm [123]. The measurements in the laboratory and in ASDEX Upgrade have been done at a measurement distance of 600 mm to the bolometer aperture (top plate opening of ITER prototypes or pinhole of vessel cameras). This corresponds at an angular uncertainty of $\Delta_{robot} = 0.1°$.

- The FaroArm absolute measurement accuracy depends on the setup, e.g on the stability of the support and the distribution of the reference points. The laboratory setup could reach a position accuracy of 0.1 mm, in comparison to the ASDEX Upgrade setting of about 0.5 mm. Considering 500 mm of movement range of the robot, this corresponds to an angular accuracy of $\Delta_{Faro-Lab} = 0.01°$ and $\Delta_{Faro-AUG} = 0.05°$.

These values allow to calculate two measurement task specific uncertainty values. For measurements assessing only the principal LOS characteristics, such as the shape, the relative width of the LOS and the existence of internal reflections, the systematic inaccuracies can be neglected. Therefore, many of the measurements performed in the laboratory setup of IBOROB have only to take the absolute position accuracy of the robot into account. The resulting overall

measurement uncertainty then corresponds to $\Delta_{Lab} = 0.1°$. For the measurement in ASDEX Upgrade and for measurements in the laboratory, where statements with regard to the global alignment will be made, all possible systematic deviations will have to be taken into account. This results in an overall measurement uncertainty of: $\Delta_{calib} + \Delta_{focus} + \Delta_{robot} + \Delta_{Faro-AUG} = 0.04° + 0.016° + 0.1° + 0.05° = \Delta_{AUG} \approx 0.2°$.

# 4. Results of line of sight measurements

In this chapter, the results of the LOS measurements of the ITER bolometer collimator prototype Versions '11 - '12 and of the in situ measurements of the ASDEX Upgrade bolometers will be presented. The results of the ITER prototypes are arranged according to the main outcomes and are followed by the derived statements and conclusions. The results from the ASDEX Upgrade bolometer measurements are being accompanied by different sections explaining the solutions to the challenges that arise from the in-situ measurement.

## 4.1   ITER prototype bolometer measurements

The ITER prototype bolometer measurements have all been conducted with the laboratory setup of IBOROB (see Chapter 3). A picture of the experimental setup can be seen on Figure 4.1, all key components of IBOROB including a few collimator parts are indicated.
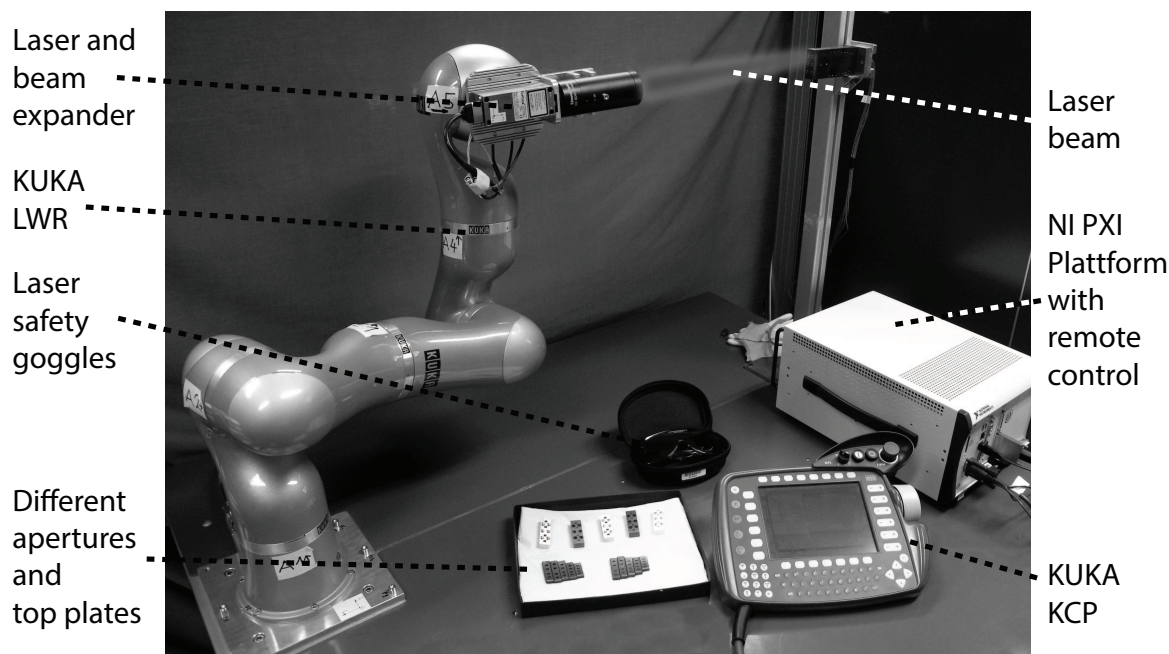


**Figure 4.1:**   Picture of IBOROB mounted on a table in the laboratory. A laser beam has been added with an image processing program. The KUKA KCP, the remote control computer based on the NI PXI plattform, the laser protection goggles and a couple of dismounted apertures and top plates can be seen on the laboratory table.

In total, a set of about 100 different collimator configurations, integrated in a database containing over 800 single measurements, have been acquired as part of this thesis work. Apart from testing the overall system performance, such as determining the measurement uncertainty and performing system tests during the gradual development of IBOROB, the main objectives concerning the bolometer camera development have been the following:

- Review and verification of the principal design by comparing the theoretical calculated LOS characteristic with the transmission measurements.

- Assessment and evaluation of various collimator/aperture configurations.

- Identification of all individual LOS influencing parts, in particular their effect on stray light enhancement and reduction.

- Gaining more understanding about the internal camera physics and optical effects in order to make the right choice for future design changes and developments.

Figure 4.2 shows a two dimensional LOS measurement plot of the '12 ITER bolometer collimator prototype in the version BL0005/ITERBolo-6 (see Chapter 2.5.1 for nomenclature) with a full set of apertures, referred in future parts of the work as the A12345 configuration. This measurement consists of an overlay of four different quadratic ($\Delta\xi = \Delta\theta = 3°$) measurement areas, one for each LOS, acquired with varying angular resolutions. Since this bolometer camera is based on a collimator design each LOS respectively channel has to be measured separately.
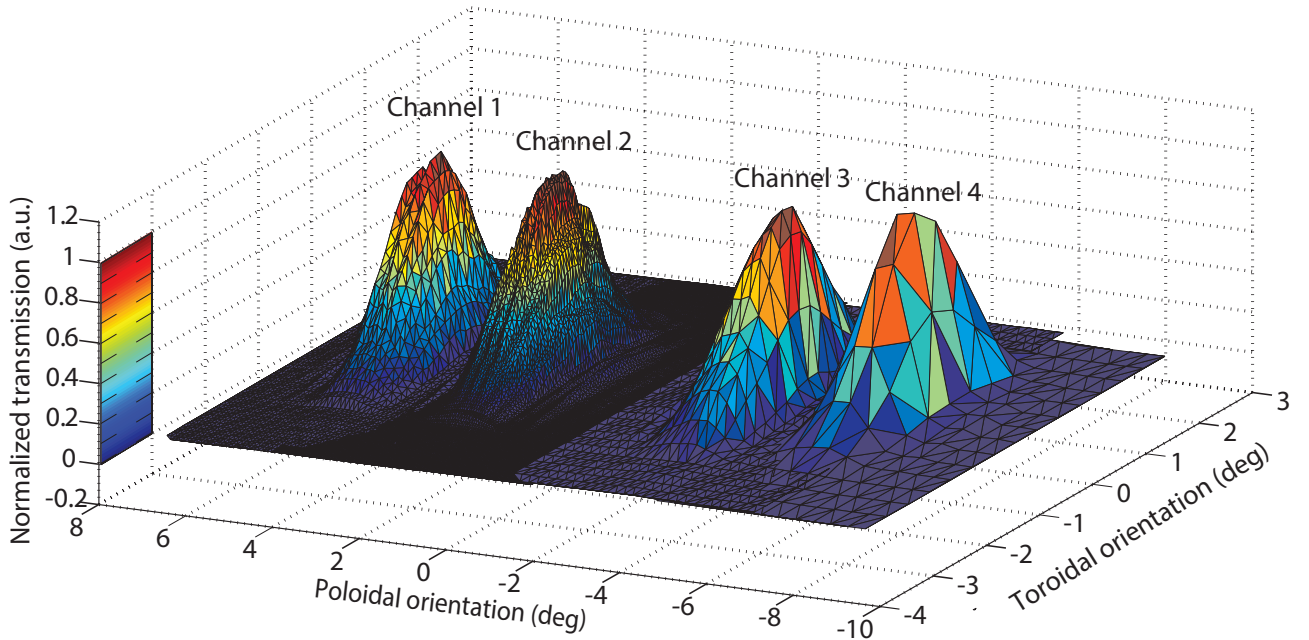


**Figure 4.2:** Two dimensional measurement of all four channels of the '12 ITER bolometer collimator prototype version BL0005/ITERBolo-6 with different measurement resolutions. A full (A12345) aperture set and a top plate with integrated microwave filtering grid was used.

Just as the theoretical transmissions (see Chapter 2.2), the measured transmissions are presented normalized to the maximum value of each detector channel. The values are taken from

the DAQ measurements of the bolometer bridge voltage in the Wheatstone bridge of the detector (see Figure 2.2, Subfigure B). They are plotted against the inclination angle in the poloidal (vertical) or toroidal (horizontal) angle in the laboratory CS. A mesh plot is generated with a Delaunay triangulation [134], the fill color is defined by the average value in the triangle. The noise of all four channels is below 5%, minor differences in the S/N ratio create a difference of the background color, in the plot visible by a lighter or darker blue, e.g. for Channel 2 beeing darker than the others.

For this measurement, the collimator is mounted in the laboratory with the fixed clamping device, thus the four channels are vertically aligned (compare mounting device Figure 3.6) which corresponds to a poloidal LOS alignment in the vessel of a tokamak CS. Oriented with respect to the laboratory CS, Channel 1 and Channel 2 are aligned in the positive poloidal direction and Channel 3 and 4 in the negative poloidal direction. The laboratory CS is defined as a right-hand Cartesian CS in the center of each camera detector with the Z-Axis in direction of the robot and the X-Axis facing upwards. The FaroArm (see Chapter 3.1.3) is used to provide the absolute position of the camera housing with respect to the robot CS. However, most of the statements can be derived from a relative position or alignment (e.g. directly from the robot CS) such as the alignment of the channels towards each other, the distances in between and the radiation throughput.

Four different resolutions respectively robot step sizes, noticeable in the plot by the differently sized triangles, have been used in these measurements to visualize the differences and illustrate the effects on the accuracy of the conclusions drawn. Table 4.1 summarizes the parameter settings and results of that measurement. In the CAD CS, the alignment of the bolometer channels corresponds to the construction design respectively theoretical calculations.

**Table 4.1:** Measurement settings for the '12 ITER bolometer collimator prototype corresponding to the two dimensional transmission measurement of Figure 4.2.

| Measurement parameters | Channel 1 | Channel 2 | Channel 3 | Channel 4 |
|---|---|---|---|---|
| CAD CS pol. orientation ($\xi_{CAD}$) | 5.15° | 2.58° | −2.58° | −5.15° |
| Lab CS pol. orientation ($\xi_{MEA}$) | 5.25° | 2.49° | −2.94° | −5.42° |
| Angular resolution ($\delta_\xi$, $\delta_\theta$) | 0.1° | 0.05° | 0.2° | 0.4° |
| Meas. time | 61 min | 242 min | 15.5 min | 4 min |
| Samples acquired | 3660 | 14.520 | 930 | 240 |

The measured poloidal orientation of the Channels in the laboratory CS is determined by calculating the center of gravity of the signal. Channel 1 and Channel 2 are acceptable within the limits of accuracy in the laboratory ($\Delta_{Lab} = 0.1°$).

Due to the poorer angular resolution of the measurement of Channel 3 ($\delta_\xi = 0.2°$) and 4 ($\delta_\xi = 0.4°$) more details are lost and the error of the interpolation increased which can bee seen as smoothing of the signal in particular at the edges ($\xi = -6°$). Finally this can lead to a false

interpretation of the transmission, signal variations such as the modulation on top of the signal on Channel 1 can only be identified with a sufficient resolution (see Section 4.1.3.1).

Only for the determination of the orientation, respective the main emphasizes of the signal, lower resolutions between $\delta_{\xi,\theta} = 0.2° - 0.4°$ are sufficient. For time-critical measurements, such as for the ASDEX Upgrade measurements presented in Section 4.2 a step size of $\delta_{\xi,\theta} = 0.15°$ was chosen as a compromise.

The IBOROB LOS calibration device has been gradually developed during the time of this work. At the beginning of the work, only one dimensional measurements could be performed, mainly because the remote control program was not available yet. IBOROB was not fully automated, for each measurement point the bolometer DAQ had to be started manually and each movement step had to be confirmed with the manual hand control (KCP), which resulted in a lot of effort for a high sampling rate. Therefore, in particular for the Model '11, it was only possible to measure with a very low angular resolution $\delta_{\xi,\theta} = 0.5°$.

However, this has not been a considerable disadvantage for the laboratory measurements. Given that most properties of the different design variations can be identified and recognized more clearly from a one dimensional measurement than a two dimensional measurement, the measurement plots for the following sections will consist only of data acquired with the one dimensional method (see Chapter 3.4.2). This applies in particular if quantitative values are to be derived from the figures.

### 4.1.1   LOS transmission of '11 collimator prototype

In order to understand the development of the ITER collimator cameras over time, the transmission measurements of the very first build prototype '11 will be presented in this section. For all measurements presented here the measurement CS corresponds to the laboratory CS and the origin is defined in the center of the detector. The measurement of the poloidal transmission of all four channels including the theoretical transmission can be seen in Figure 4.3. The theoretical LOS characteristic was calculated according to the equations presented in Chapter 2.2.3.

In order to have an exactly defined LOS, the '11 ITER bolometer collimator protoype (see Chapter 2.5.1, Figure 2.10) has been manufactured by high-precision electro-erosion machining made out of one piece of TZM which corresponds to the Subfigure E of Figure 2.7 in Chapter 2.3. Thus, it contains toroidal subcollimators over the whole length of the camera. The main design drivers were to obtain a high thermal conductivity and mechanical strength besides being easy to manufacture and assemble.

However, this prototype proved to suffer significantly from reflections, which can be clearly seen by the significantly broader LOS than the transmission predicted by the theoretical calculations.
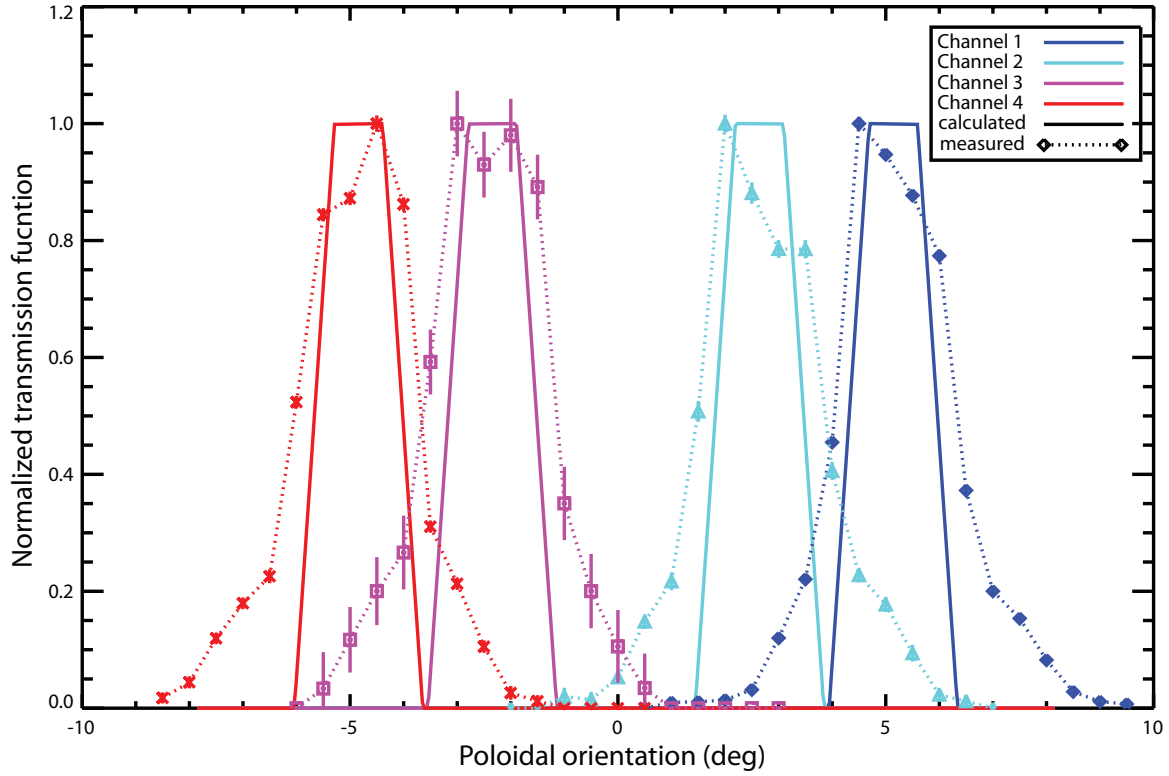
**Figure 4.3:** Normalized poloidal transmission function of the '11 ITER bolometer collimator protoype [92]. The dashed lines correspond to the measured data, the solid line is the theoretical calculated transmission ($k_\xi(\xi)$).

That implies that the Etendue of each LOS is much larger, too. The channels in this bolometer camera have been wire eroded over their whole length which creates a flat and very smooth surface prone to mirror-like reflections. Using this camera in a fusion device to derive the radiated power the results would be too high. In toroidal orientation, the transmission shows the same behavior (not shown here, see [92]).

## 4.1.2 LOS transmission of '12 collimator prototype

The results from the measurements of the '11 collimator prototype lead to the development of the aperture-style '12 collimator prototype. It is clear that the surface, the material, the shape and finishing has a major influence on the LOS transmission by reducing or allowing for reflections. Thus, in order to study the interaction of all these components in detail a modular design has been developed (see Chapter 2.5.1 for design details and aperture denomination) allowing to integrate different aperture sizes to obtain different LOS shapes and widths.

A range of dedicated experiments (800+ individual measurements) have been carried out with this new collimator version during this work: The different aperture configurations have been compared to each other, the two which different the most (BL0005 and BL0001) will be presented in the following sections, distinguished between the poloidal and toroidal characteristics.

Moreover, the influence of the different top plate types, with and without microwave filtering grid, will be evaluated. Furthermore, the collimator housing has been modified and a test coating has been applied and evaluated in respect to the transmission changes.

The advantage of these various experiments was to gain experience operating IBOROB over time and allowing to distinguish between configuration and measurement errors or trustworthy results. All measurements presented from the measurements of the '12 collimator prototype are one dimensional measurements performed with a step size of $\delta_{\xi,\theta} = 0.05°$ which allows to detect the smallest transmission differences in the range of the measuring uncertainty.

#### 4.1.2.1   Apertures with a wide viewing cone

Firstly, the measurement results of the large apertures with a wide viewing cone (aperture version BL0005 with top plate ITERBolo-9) will be presented. Figure 4.4 shows a toroidal plot and Figure 4.5 a poloidal plot of the transmission measurements.
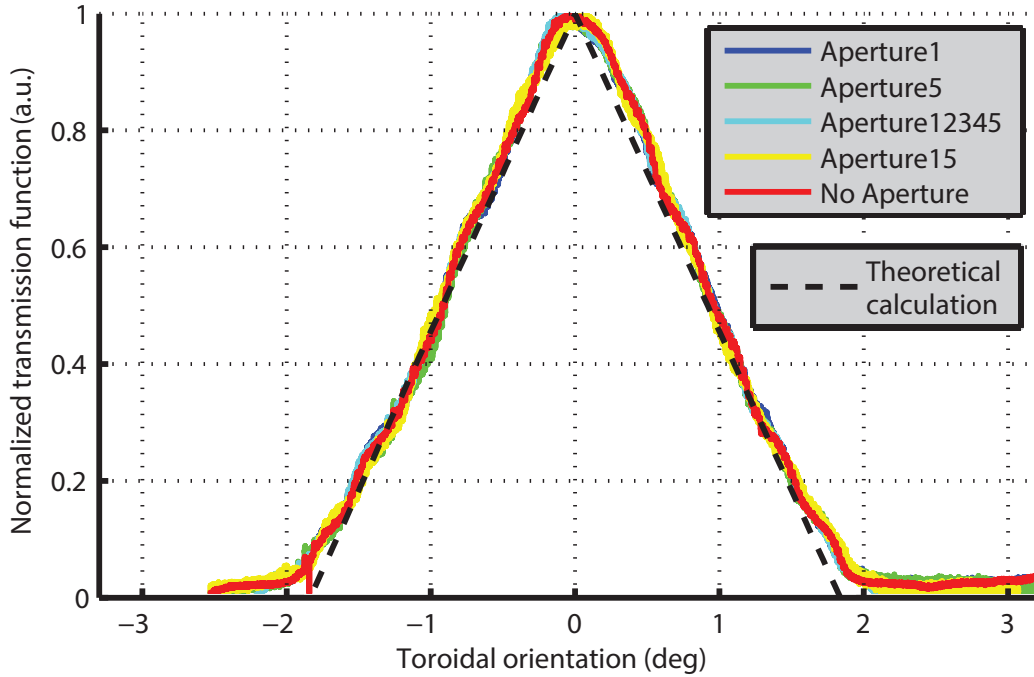


**Figure 4.4:**   Normalized toroidal transmission function of a collimator with a wide viewing cone (BL0005). Different aperture configurations: All five apertures (Aperture12345), only the first (Aperture1), only the last (Aperture5), a special combination (Aperture15), without apertures at all (No Aperture) and the theoretical calculation is integrated in the plot.

For the first analysis, only Channel 2 will be analyzed. The other channels have been measured only to verify the symmetrical design of the collimator. Channel 1 corresponds to Channel 4 and Channel 2 to Channel 3 (see Chapter 2.2.3), but they are not shown here. They show the same behavior and deviate only within the context of the measuring accuracy. Here, five different aperture configurations are compared: A full set (Aperture12345), only the first (Aperture1), only the last (Aperture5), a special combination (Aperture15) and without any apertures at
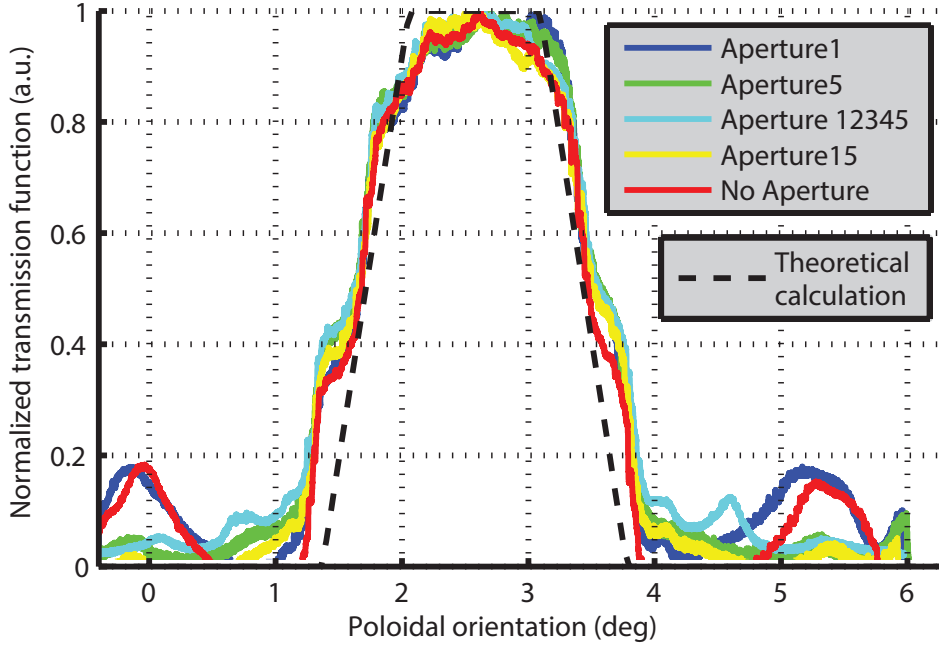
**Figure 4.5:** Normalized poloidal transmission function of a collimator with a wide viewing cone (BL0005). Different aperture configurations: All five apertures (Aperture12345), only the first (Aperture1), only the last (Aperture5), a special combination (Aperture15), without apertures at all (No Aperture) and the theoretical calculation is integrated in the plot.

all (No Aperture). This allows to study the collimator prototype as a function of number of apertures. Adding the theoretically expected transmission according to the design (dotted line) in the plots allows to assess the quality of the LOS definition.

The toroidal LOS of Figure 4.4 shows a triangular shape and virtually no deviation from the theoretical LOS for different configurations. Even with fewer apertures, no substantial loss of signal shape is evident. The LOS is sufficiently defined with the top plate only (No Aperture). For the poloidal transmission a similarly good characteristic, with a minor unsteady signal rise at $\xi = 1.5°$ and $\xi = 3.5°$ can be achieved. The flat top of the trapezoidal signal shape between $\xi = 2.15°$ and $\xi = 3.15$ can not be perfectly attained, the signal shape is still slightly rounded.

With too few (Aperture1) or no apertures, reflections from the remaining channel walls appear in the signal with a maximum at $\xi = 0°$ and $\xi = 5.5°$. The reflections appear on both sides of the signal due to the poloidal symmetry of the camera construction and add in total $\approx 10\%$ more power to the signal. If the diagnostic is operated in this configuration and this characteristic remains unnoticed during the experimental operation, more radiated power then actually present will be calculated.

The location of the reflection inside the collimator housing can be estimated: 2.5° angular difference of the reflection to the LOS center corresponds to half the length of the collimator ($L_c = 150\,\text{mm}$) and half of the channel width ($W_{channel} = 6.5\,\text{mm}$): $\arctan(\frac{3.25\,\text{mm}}{75\,\text{mm}}) \approx 2.5°$. Therefore, this single reflection is located approximately in the middle of the collimator length.

The reflections don't appear for the same configuration in the toroidal plot, because the channel walls are further apart in the toroidal orientation. Similar reflections probably exist for steeper angles of incidences (which have not been measured here) as well. However, then the light has to reflect multiple times in between the channel walls to reach the detector which would dampen its intensity to a value below the threshold of the measurement accuracy.

On the one hand it is trivial to show that too few apertures are not enough to correctly define the LOS. But on the other hand, the maximum number can not be recommended straightaway, too. Of particular interest in this context is the aperture setting with the first and the last aperture (Aperture15). The large reflection on the sides of the signals have disappeared and the transmission shows less reflections around the border of the main LOS than the configuration with the full aperture set (Aperture12345). That implies that more apertures not necessarily result in a better signal, e.g. for a large viewing cone as presented. Here, the best performance in both orientations is achieved with a careful selected aperture set (Aperture 15).

### 4.1.2.2   Apertures with a small viewing cone

For a configuration with the small viewing cone (aperture version BL0001 with top plate ITERBolo-7) Figure 4.6 shows the measured transmission in toroidal orientation and Figure 4.7 in the poloidal orientation. Both orientations have a triangular transmission shape. In the toroidal orientation, the theoretically expected transmission can be reached only with a full set of apertures. The other aperture configurations show a much broader signal than desired. The top plate only configuration (No Aperture) has more than 200% of the intended signal power. Moreover, the configuration with the first and the last aperture (Aperture15), which has been considered as good for the wide viewing cone, also adds about 50% to the signal power. All these settings are not acceptable.

The edge area of the full configuration (Aperture12345) shows still strong reflections and stretches the transmission symmetrically in both positive and negative orientations. A signal width over $\Delta\theta = 2°$ can be recognized for transmission values below 10%. However, the LOS shape gradually improves by adding apertures, but it is also clear that even five apertures are not sufficient to define the signal properly. The top aperture (Aperture5) seems to narrow the shape of signal around the top ($-0.2° < \theta < 0.2°$) and apertures which are in the lower or middle part are influencing the broader LOS shape ($-0.5° < \theta < 0.5°$).

This is as expected, because for (almost) perpendicular incoming radiation ($-0.2° < \theta < 0.2°$) the top plate defines the maximum possible viewing cone. Under the assumption that the construction is free of errors and for a straight incidence of light reflections are not relevant because the radiation falls directly onto the detector. All additional apertures are only necessary to limit the radiation incoming from other incident angles larger $-0.2° > \theta$ or $\theta > 0.2°$.
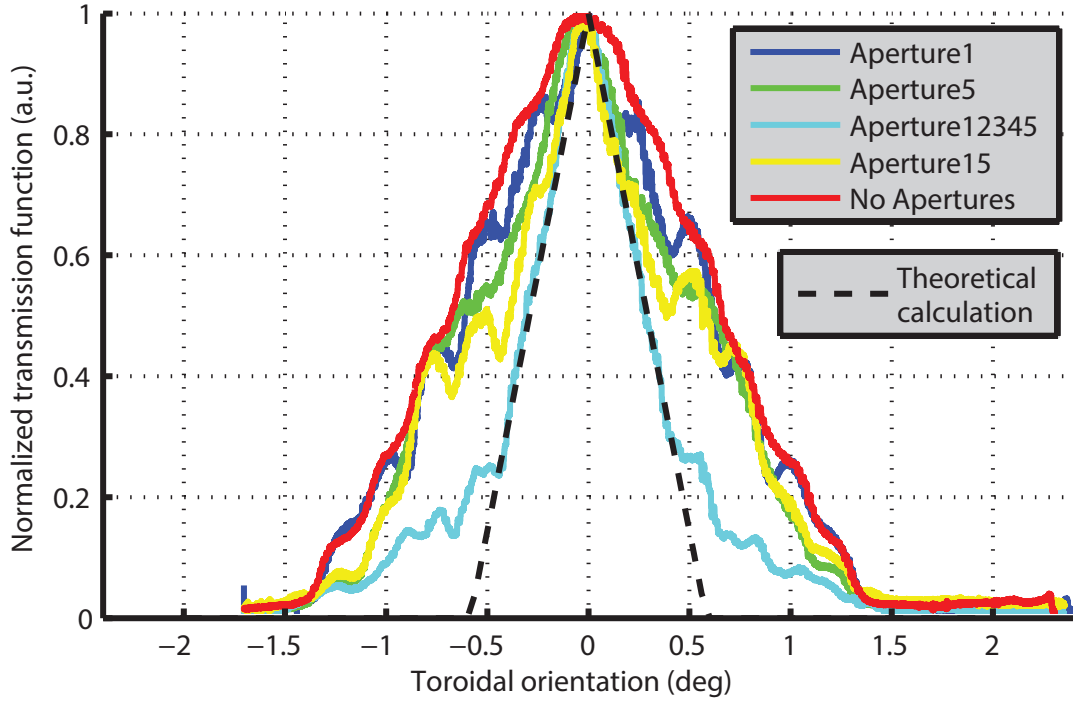
**Figure 4.6:** Normalized toroidal transmission function of a collimator with a small viewing cone (BL0001). Different aperture configurations: All five apertures (Aperture12345), only the first (Aperture1), only the last (Aperture5), a special combination (Aperture15), without apertures at all (No Aperture) and the theoretical calculation is integrated in the plot.

In poloidal orientation (see Figure 4.7), the transmission is less dependent on the different aperture configurations which is similar to the behavior of the wide aperture set. The configuration without apertures (No Aperture) and the configuration with only the aperture which is the closest to the detector (Aperture1), are both insufficient to define the LOS shape. The most important aperture in this setup is the last aperture (Aperture5), because it filters the poloidal stray light at $\xi = 6°$ and $\xi = -0.5°$. Alternatively, the special configuration (Aperture15) would also be acceptable.

Drawback of a full set of apertures (A12345), are the enhanced reflections around the edges ($\xi = 1.4°$ and $\xi = 3.7°$) of the main LOS. Moreover, the transmission shows a small modulation of the signal edges ($\xi = 2°$ and $\xi = 3.2°$), note the rise and decrease. However, due to its low intensity it has no serious impact on the diagnostic relevant characteristic.

In conclusion, the small aperture version BL0001 has to use toroidal subcollimators and many apertures in order to achieve the narrow toroidal LOS width under the condition of the limited camera length. In poloidal orientation the subcollimators are not needed and more apertures do not necessarily mean a better LOS. However, it is probable that even more apertures will be implemented in the future (see collimator design model '13 in Chapter 2.5.1) combined with modifications of the apertures which will reduce the additional unwanted signal power, in particular in poloidal orientation (see Section 4.1.3.4).
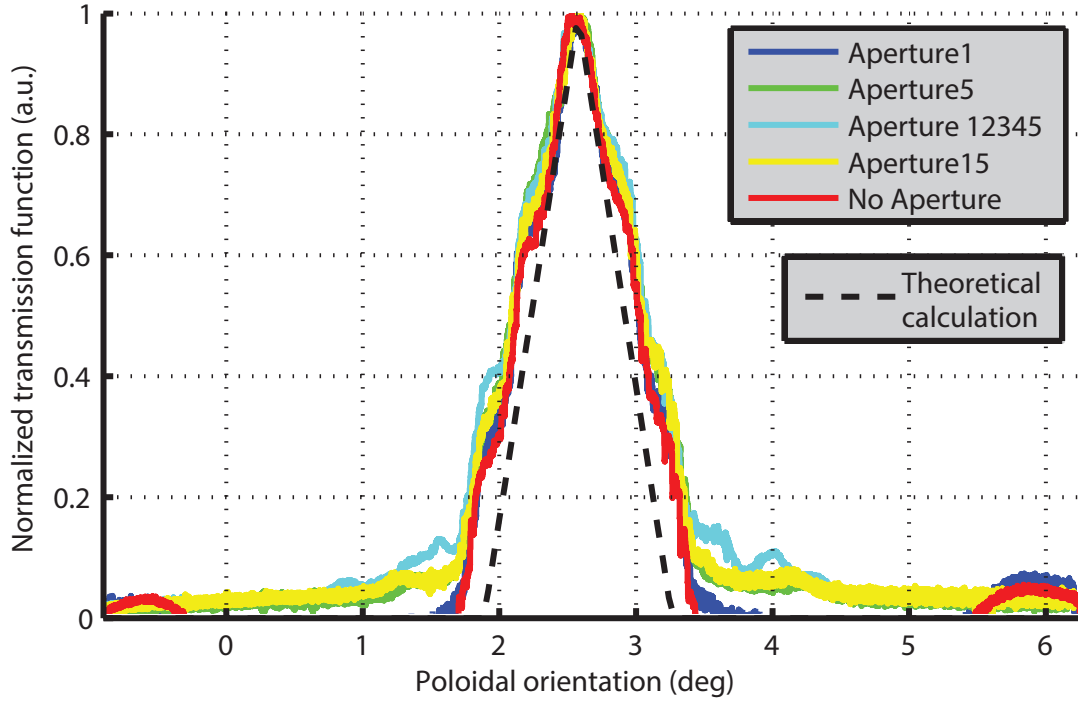
**Figure 4.7:** Normalized poloidal transmission function of a collimator with a small viewing cone (BL0001). Different aperture configurations: All five apertures (Aperture12345), only the first (Aperture1), only the last (Aperture5), a special combination (Aperture15), without apertures at all (No Aperture) and the theoretical calculation is integrated in the plot.

### 4.1.3   Optical properties of the of '12 collimator prototype

Apart from the apertures defining the principal LOS shape, the camera body construction has also an impact on the LOS characteristics due to facilitating or avoiding reflections towards the detector. In the following sections different camera parts have been studied, whether and to what extent they have influence on the LOS transmission.

#### 4.1.3.1   Transmission modulation due to the microwave filtering grid

The top plate version ITERBolo-6 of the '12 ITER bolometer prototype camera contains a grid with a thickness of 5 mm in order to filter ECRH stray radiation from the detector. More details and the necessity for the installation of a microwave grid in the optical path of the bolometer camera has been explained previously in Chapter 2.5.3.

The measurement of Channel 4 ($\xi_{max}^4 = -5.15°$) in poloidal orientation with and without the microwave filtering grid can be seen in Figure 4.8: ITERBolo-9, which has the same top plate opening dimensions is compared with the top plate ITERBolo-6. Both configurations are considered as a wide viewing cone. The figure on the left shows the bolometer bridge voltage as measured and the figure on the right shows the normalized signals. The top plate containing the microwave filtering grid shows signal variations in form of a continuous amplitude modulation ($-6° < \xi < -4°$). About 20% amplitude modulation (from the maximum to the minimum),

with regard to the global signal amplitude, can be calculated. The modulation can also be recognized at the edge of the main LOS at poloidal angels left of $(-7° < \xi < -6°)$ or right of the center $(-4° < \xi < -3°)$, where it can only be noticed as small waves.
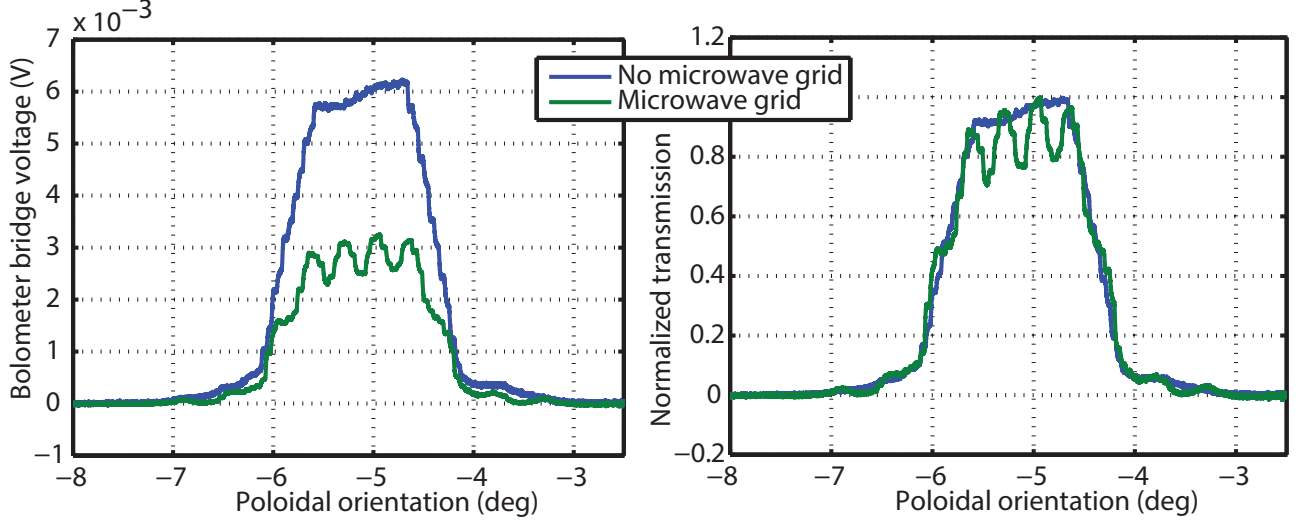


**Figure 4.8:** Poloidal transmission function of a wide viewing cone equipped with a top plate with (ITERBolo-6) and without (ITERBolo-9) an integrated microwave filtering grid. A constant signal modulation introduced by the microwave grid can be identified but the main trapezoidal signal characteristic is not altered. The figure on the left shows the bolometer bridge voltage as measured and the figure on the right the normalized signals.

The modulation has a constant frequency during the complete transmission measurement. There are about 3.5 oscillations per degree. However, it should be mentioned that such a modulation does not influence the accuracy of the overall measurement system. The bolometer diagnostic performs a line integrated measurement over the whole LOS and the spatial accuracy is defined by the maximum poloidal LOS width (for a camera performing tomography of a poloidal cross section). The modulation does not influence the orientation of the LOS or the main characteristic. Only a slight enhancement of the LOS edges can be seen ($\xi = 3.7°$ and $\xi = 1.3°$). But as they are generating not more than 1% of additional power, they can be neglected.

However, the absolute bolometer bridge voltage signal shows a difference with respect to the maximum transmission values. The grid masks half of the aperture entrance and thus reduces the effective area of incident radiation. Comparing the one dimensional Etendue $(E_i = \int_{-\infty}^{\infty} K_i(\xi)\, d\xi)$ by integrating over the voltage values (without unit) ITERBolo-6 amounts to $E_i = 159.6$ and ITERBolo-9 to $E_i = 77.3$. Thus, the microwave grid filters 52% of the light yield. The differences are due due to the modulation of the signal, in particular at areas of $\xi = -5.8°$ and $\xi = -4.5°$.

The decreasing of the maximum light yield is not optimal, because the poloidal opening of a bolometer camera with a microwave grid has to be twice as large as one without in order to achieve the same light yield. The decrease was expected, but the Etendue value has to

be known exactly, otherwise it will result in an systematic error in the calculation of the total absorbed power. In the case of deriving the orientation of the transmission, this effect has to be taken into account as well. Instead of taking the maximum of the signal as measure, the signal main emphasis will have to be calculated from two dimensional measurements. Alternatively, in order to remove the modulation from the LOS characteristics completely, it could be tried to place the microwave filtering grid in an aperture closer to the detector, e.g. integrated into Aperture 1 to reduce the influence.

### 4.1.3.2 Reflections due to the channel walls

Next, the influence of the channel walls separating the channels is examined. Originally, they have been introduced to reliably avoid channel cross talk. The fact that channel borders close and parallel to the channels can have a negative effect could be shown in the figure of the narrow viewing cone 4.5. In order to check if they are really necessary, the collimator housing has been modified.
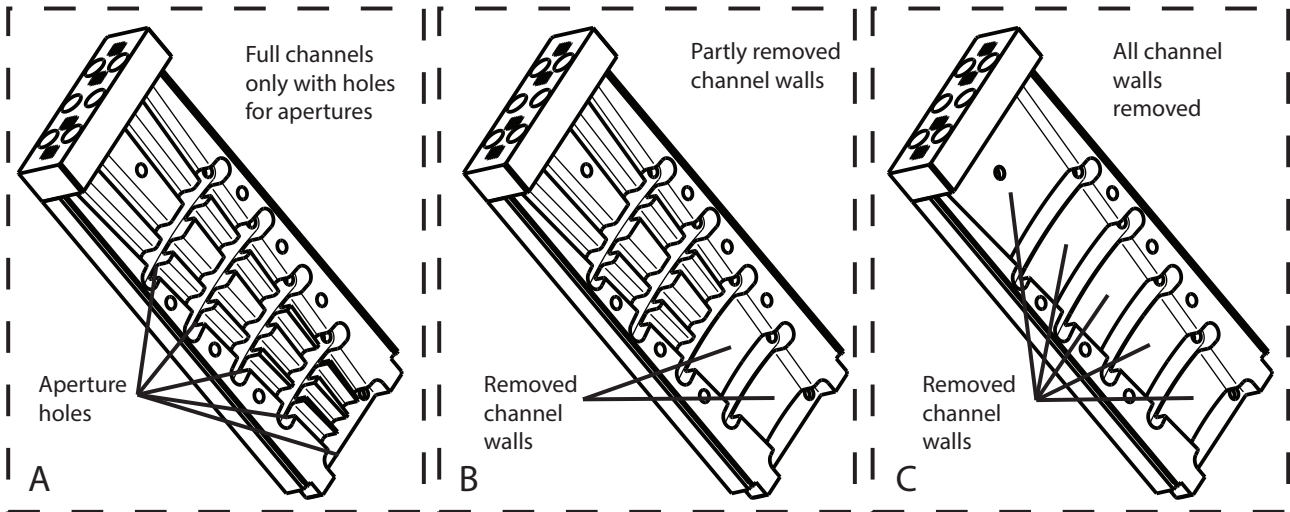


**Figure 4.9:** Three different collimator housing versions: Subfigure A shows the collimator with full channels, only interrupted for the aperture sinks (as shown in Figure 2.11). Subfigure B shows an interim version with partly removed channel walls and in the last version of the collimator, Subfigure C, all channel walls have been removed.

Figure 4.9 shows the evolution of the collimator housing. The version on Subfigure A has continuous channels and corresponds to the one presented in Chapter 2.5.1. In the version of Subfigure B, the channel borders have been partly removed (from the first to the second aperture sink). In Subfigure C the channel borders have been completely removed, only about 5 mm long parts towards the top have been left in order to fix the position of the top plate. In this isometric CAD figure, the remaining material is hidden under the top plate, but it can be seen in Figure 4.11 of the following section which shows a photo of the collimator.

Figure 4.10 shows the poloidal transmission measurement of the three different collimator housing versions, here for Channel 2 equipped without any apertures in order to emphasize the re-
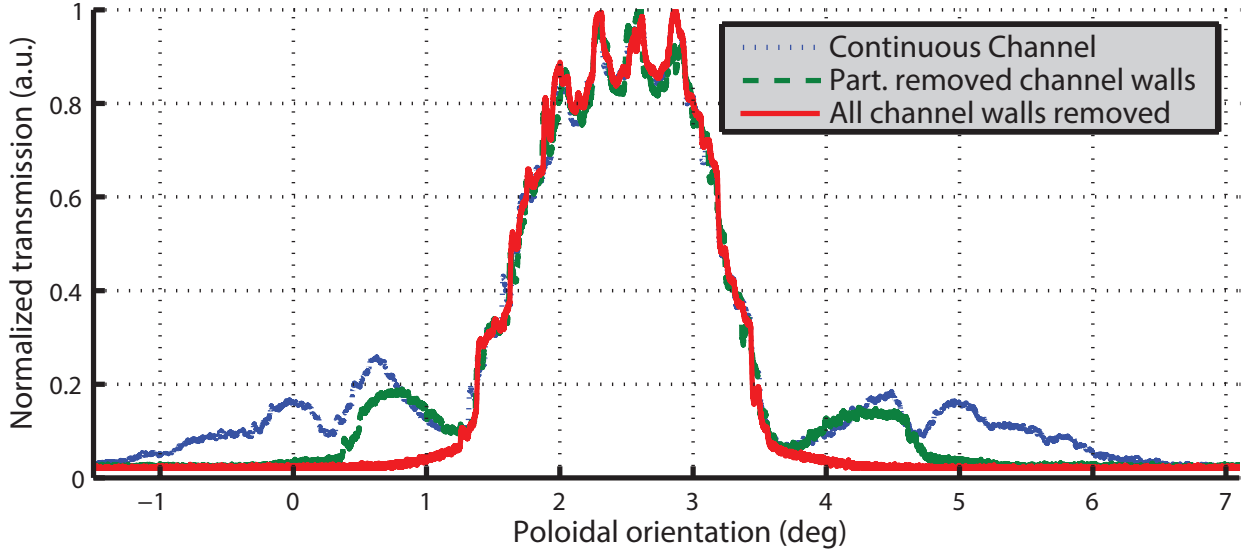
**Figure 4.10:** Normalized poloidal transmission measurement of Channel 2 of a wide viewing cone (BL0005). The transmission of three different collimator housing versions of Figure 4.9 is compared. Enhanced reflections can be identified at the edge of the LOS for the collimator including the channel walls.

flections and to simplify the analysis. For this measurement, the top plate version ITERBolo-8 has been used. It is equipped with a microwave filtering grid, thus the modulations can be seen again (see Section 4.1.3.1). Here, they do have no impact on the conclusions.

The comparison shows that the channel walls have a negative impact on the transmission by introducing reflections which significantly broaden the signal. The original version shows two reflection peaks on both sides of the LOS ($\xi = 0°$, $\xi = 0.7°$ and $\xi = 4.4°$, $\xi = 5.1°$), the version with the partly removed channel walls only one peak ($\xi = 0.8°$, $\xi = 4.3°$) and with all removed channel walls no peak.

This behavior can be explained by tracing the radiation beam outside of the main LOS center ($1.4° < \xi < 3.6°$). Radiation with an incident angle slightly steeper strikes firstly the channel wall at the bottom of the collimator (close to the detector). For steeper angles the point of reflection is moving upward, but only as long as the channel wall exists. In a simplified scheme, removing a part of the channel border removes the equal amount of reflections.

However, only the channel walls in the middle of the collimator can be removed. Figure 4.12 shows a measurement of Channel 1 (in contrary to Channel 2 shown previously) in the collimator version with the partly removed channel walls (Subfigure B, Figure 4.9). The same effect can be observed for an angle of incidence of $\xi = 7°$. But on the other side ($\xi < 4°$) the radiation is reflected by the camera housing which has not been modified. Thus, it still shows the two reflections peaks ($\xi = 2.5°$ and $\xi = 3.2°$).

Summarized, Channels 2 and 3 benefit from this situation because they can reach a well defined poloidal LOS characteristic, even without the use of any apertures. Channels 1 and 4 only partly improved as one side still provides reflecting surfaces. The reason is that the channel wall is

aligned parallel with respect to the LOS and that the LOS is too close to the wall. If the wall had a different shape or another angle (see collimator Model '13), those direct reflections would not take place.

Furthermore, these parts should avoid flat structures in order to mitigate direct reflections. If the surface is determined by the manufacturing process, as in our case by the wire erosion process, a regular structuring of the surface, such as fine grooving or a high roughness, should be considered to spread the reflections in different orientations. However, for a configuration with multiple apertures this effect will probably be less significant. Nonetheless, as a general rule, all parts which are not relevant for defining the LOS, needed for the mechanical stability or on the basis of other constraints should be removed or minimized.

### 4.1.3.3   Reflections from the collimator housing

In order to further reduce any generated reflections from the collimator housing an experiment with an anti-reflective coating has been performed. First aim is to roughen the surface, so that the radiation is scattered in multiple directions instead of being reflected back in one specific angle (diffuse reflection distribution instead of specular). Second aim is to enhance the radiation absorption of the used material in order to remove the scattered radiation completely from the camera. For ITER, certain ceramic-based coatings for optical components are already foreseen, e.g. $B_4C$ or $TiO/Al_2O_3$.

But due to the difficult application and limited access of these coatings, a water-based coating named $AquaDAG$®[1], containing a high content of ultra-fine particles of graphite, was applied to evaluate prospects for the development of future ceramic coatings and to evaluate its general necessity. Advantage of this coating is that it is water based, therefore it can be easily applied with a spray gun, also on complex geometries. An image of the two collimator states (with and without the coating) can be seen in the Figure 4.11.

Usually, this coating is used to generate electrically conducting areas in order to avoid build up of static areas and provide electrical screening. But at ASDEX Upgrade and JET this coating has been used successfully in the past for optical components to reduce the scattering of internal stray light. The spectral performance, the refractive index and wavelength range of the coating are not known, but as the coating is based on 18% graphite, its characteristic can be expected to be close to the one of carbon. However, the exact value of the absorption coefficient is difficult to determine. Moreover, the reflections take place at extremely flat angles $(1° - 5°)$ where the reflection coefficient strongly depends on the surface roughness.

Figure 4.12 shows the poloidal transmission measurement of Channel 1, before and after the application of the coating. A wide viewing cone has been used (BL0005) combined with the ITERBolo-8 top plate and no apertures have been integrated. Thus, a lot of stray light and

---

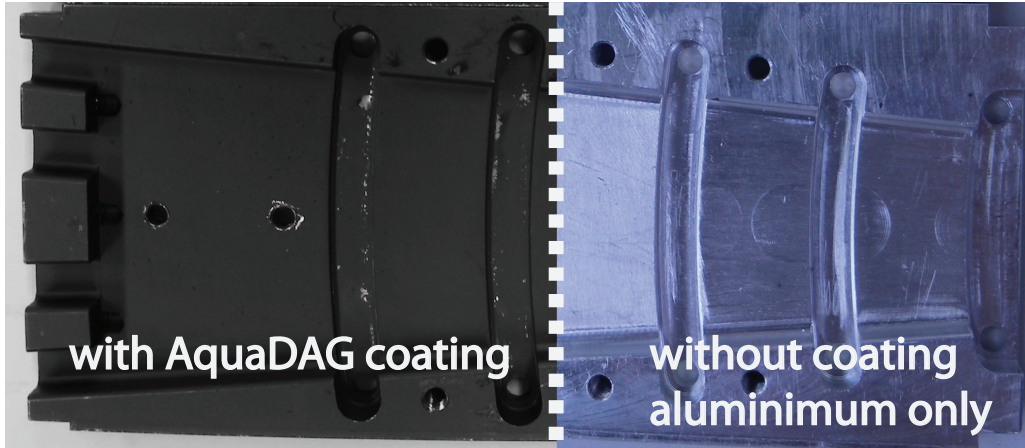[1] *"AquaDAG"*: Abbreviation for *Aqueous Deflocculated Acheson Graphite.*

**Figure 4.11:** Left: Image of collimator coated with graphite based coating AquaDAG. Right: Uncoated, original aluminium collimator body.

internal reflections are generated which allow a clear comparison. The status of the collimator corresponds to the partly removed channels version, see Subfigure B in Figure 4.9. Thus, the reflections are not symmetric (see Section 4.1.3.2).
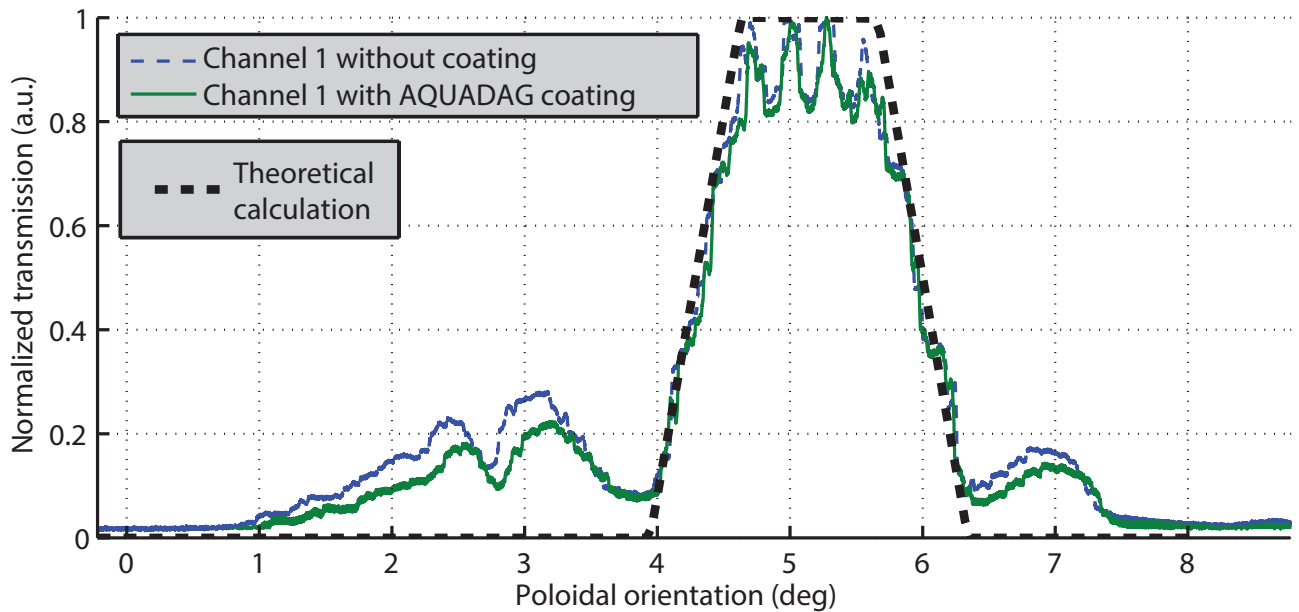


**Figure 4.12:** Normalized poloidal transmission function of a wide viewing cone (BL0005). Unmodified collimator body and collimator body coated with AquaDAG can be compared. Enhanced radiation absorption can be identified at the wall reflections areas ($0.5° - 1.5°$, $4° - 5°$ and $5.5° - 6°$).

The radiation attenuation due to the coating can be seen on both sides of the main LOS ($\xi = 7°$ and $4° > \xi > 1°$). An attenuation of roughly 30% was achieved. The differences in the amplitude of the reflection on each side could be due to the different surface roughness of the two channel borders. Figure 4.10 shows similar amplitude differences.

It has been demonstrated that a coating of the collimator can help to absorb a part of the stray radiation, however, the achieved values are not sufficient. No scattering of the radiation could be observed, only the absorption coefficient of the material has been changed. The shape of the reflections have remained the same, mainly specular reflections take place. A future coating will have to perform much better and should contain larger particles in order to generate a rough surface finish, thus dispersing the reflections in different orientations (diffuse reflection). Moreover, the wear resistance of this coating will have to meet the specific conditions of ITER (see Chapter 1.2). In particular it has to be guaranteed that this coating does not deteriorate with time. In the end, the decision whether or not to apply a coating has to be taken regarding the properties of the final collimator design.

#### 4.1.3.4   Reflections inside the apertures

In this section, a closer look on the aperture optical properties and their influence on the transmission will be taken. The apertures are manufactured via Electric Discharge Machining (EDM) due to the complex shape, the required accuracy and the difficult processing of such a hard material as TZM (see Chapter 2.5.1). Because of the nature of the spark erosion of the EDM process, the final surface characteristics are very smooth. Tracing individual incoming rays with a CAD program[1] suggested that the smooth surfaces inside the apertures, respectively in-between the subcollimator walls, lead to some of the observed reflections. The standard aperture thickness of all apertures of the '12 ITER bolometer prototype is $T_{apertures} = 5\,\mathrm{mm}$.

In order to identify to what extent the aperture thickness contributes to these reflections an aperture set was modified. Aperture version BL0001 was selected because the reprocessing of aperture configurations with subcollimators was considered technically delicate and too risky. The internal material of the aperture was removed which resulted in a "double aperture" integrated in one original aperture part (see Figure 2.12, Subfigure D of Chapter 2.5.2). This aperture was then denominated BL7. All five apertures necessary for the collimator have been adapted.

The measurement results of the toroidal transmission function can be seen in Figure 4.14 and in poloidal orientation in Figure 4.13 for Channel 3. In each plot the original (unmilled) BL0001 aperture version has been added to the plot for comparison. The areas of interest at the edge of the LOS are shown in an enlarged window. An improvement of the characteristic, respectively a reduction of stray light around the edges of the LOS can be identified.
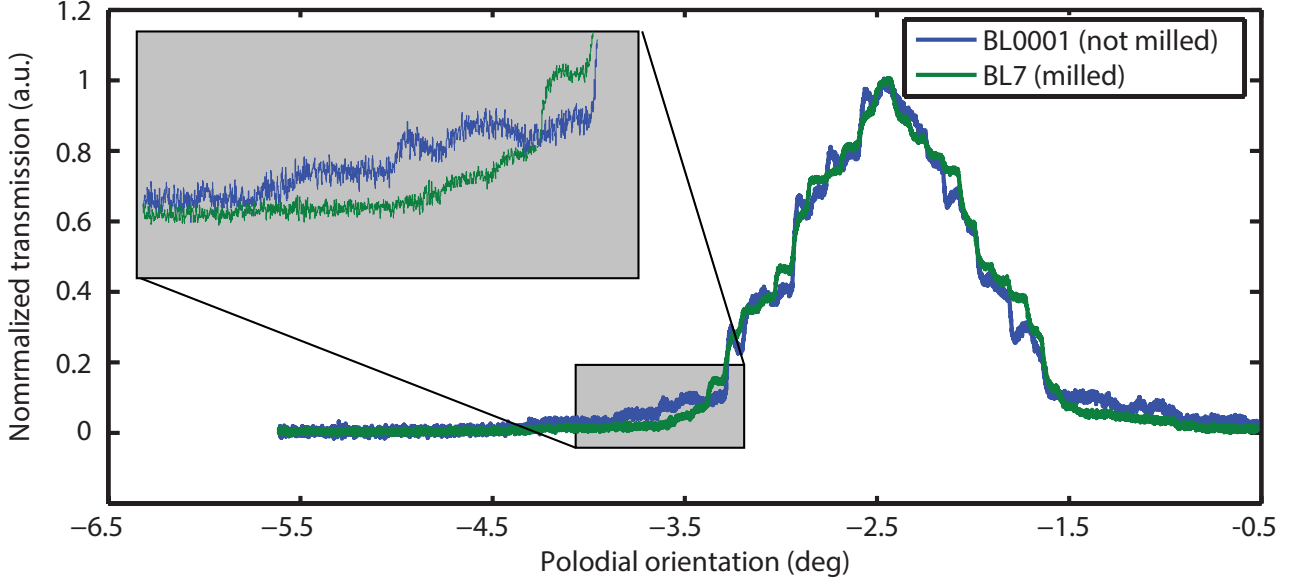
---

[1]CATIA V5 R19.

**Figure 4.13:** Normalized poloidal transmission function of a wide viewing cone (BL0001) of Channel 3. Comparison of the normal aperture version and the milled apertures (BL7). The signal at $\xi = -4°$ and $\xi = -2°$ shows fewer reflections at the edge of the LOS.
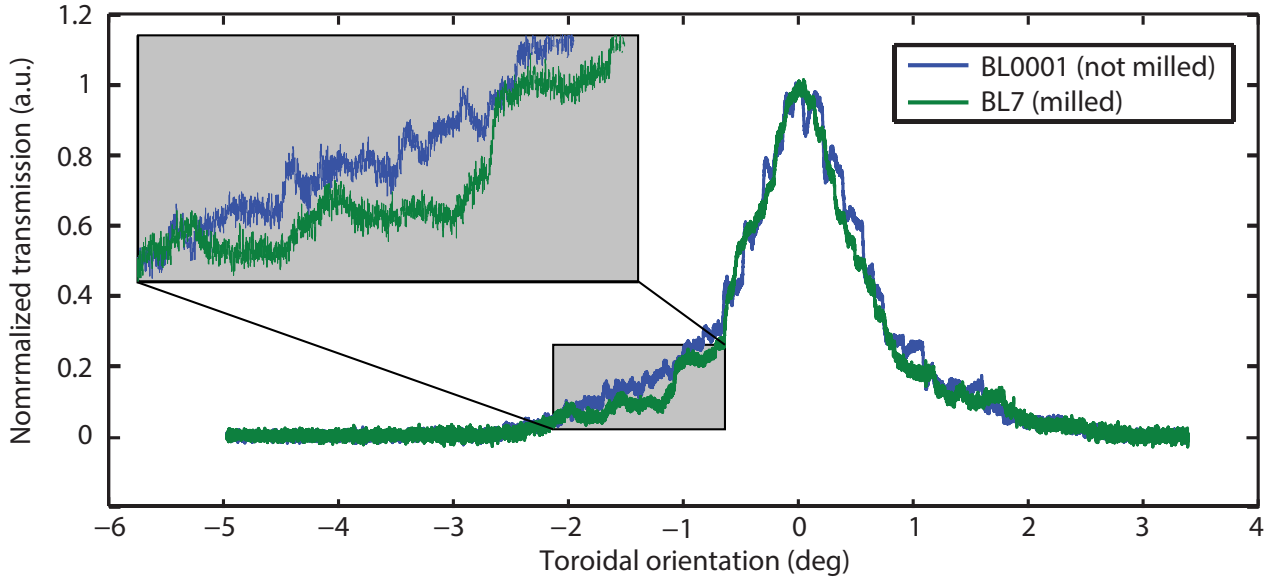


**Figure 4.14:** Normalized toroidal transmission function of a wide viewing cone (BL0001) of Channel 3. Comparison of the normal aperture version and the milled apertures (BL7). The signal at $\theta = -5°$ and $\theta = -2°$ shows fewer reflections at the edge of the LOS.

The difference is in the range of a few per cent. In total 5 apertures have been modified which means 3 mm material per aperture has been removed out of the 5 mm thick apertures which corresponds to a total of 15 mm material removal. Comparing this number with the length of the removed channel borders ($\approx 145$ mm) the fractions as stray light reduction (in %) correspond: $\frac{30\%}{145\,\text{mm}} \simeq \frac{3-4\%}{15\,\text{mm}}$.

From these measurements it can be concluded that the apertures of the collimator should be as thin as possible, subject to the requirement of the minimum thickness allowed by the thermal,

mechanical and manufacturing constraints. Furthermore, every surface which is parallel to the LOS orientation should be avoided as far as possible.

### 4.1.4 Influence of beam focus on transmission measurement

In this section, the influence of a different, non parallel beam focus is analyzed. During the requirements analysis of IBOROB in Chapter 3, the need of a radiation source emitting parallel light, respectively with a lowest possible beam divergence has been mentioned. How the transmission is affected can be seen in Figure 4.15, split into the poloidal orientation on the left and toroidal orientation on the right. Here, the measurements are not normalized to their respective maximum. Multiple measurements have been performed from a closed to an open focus ($\varnothing_1 \approx 1\,\text{mm}$, $\varnothing_2 \approx 8\,\text{mm}$, $\varnothing_3 \approx 18\,\text{mm}$, $\varnothing_4 \approx 27\,\text{mm}$) and even a diverging laser beam ($\varnothing_5 \approx 40\,\text{mm}$), see the legend in the figure. For all measurements of this figure, the large aperture set (BL0005) with the microwave grid top plate has been used (compare Figure 4.4 and Figure 4.5).
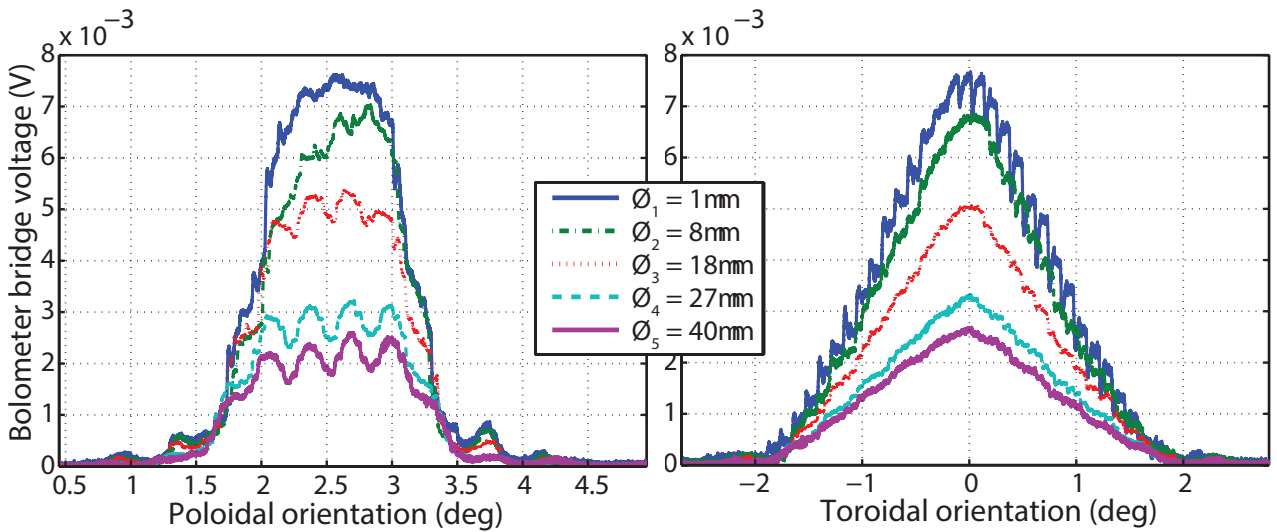


**Figure 4.15:** Poloidal and toroidal transmission of the bolometer bridge voltage. The laser focus has been gradually changed from a maximum possible focus to a diverging beam. The microwave grid modulation in the poloidal orientation gradually disappears for a stronger focus, in the toroidal orientation mainly the amplitude increases.

The poloidal transmission shows an increase of amplitude the more the laser is focused. This is due the increased power entering into the collimator camera and is as expected. The modulation due to the microwave grid gradually disappears with each focus change. Firstly the relative amplitude of the signal decreases (from $\varnothing_4$ to $\varnothing_3$), then the identification gets difficult $\varnothing_2$ and finally the characteristics disappears completely ($\varnothing_1$) from the signal shape.

This can be explained theoretically: In the IBOROB laboratory setup the distance between the beam expander lens and top plate is approximately 600 mm, the lens diameter has 27 mm. Therefore, the beam is fanned out of $\arctan(\frac{27\,\text{mm}}{600\,\text{mm}}) \approx 2.5°$. The measurement then corresponds

to a signal convolution of a 2.5° fanned out Gaussian shaped function with the original signal, as a change of focus does not change the beam profile leaving the beam expander.

The resulting signal is filtered like a first grade low-pass filter and the modulation disappears. Moreover, the focusing introduces additional reflections at the border of the main LOS which do not exist for the parallel incident radiation ($\xi = 3.7°$). The defocused, respectively diverging laser beam ($\varnothing_5 \approx 40\,\text{mm}$) has the largest amplitude modulation.

The toroidal transmission shows the same increase of amplitude. The LOS characteristic is not altered. The maximum focused laser beam ($\varnothing_1 \approx 1\,\text{mm}$) shows a new modulation with a high frequency of $\approx 0.13°$. This is due to the positioning inaccuracy of the robot which is in the same order of magnitude. Small positioning inaccuracies now have a large impact on the measured transmission signal.

### 4.1.5  Influence of beam shift on transmission measurement

The laser beam is supposed to be oriented onto the center of the bolometer aperture. However, the only possibility to check if the setup is correct is by eye and through the laser protection glasses which results in a certain degree of uncertainty. Goal of this section, is to investigate the influence of a constant laser positioning inaccuracy on the transmission measurement

Therefore, multiple one dimensional toroidal measurements of ITERBolo-9 and BL0005 with a laser beam shifted gradually (1 mm steps) in the toroidal plane have been performed. The laser was shifted from an offset of $\Delta_{tor} = -5\,\text{mm}$ to $\Delta_{tor} = 5\,\text{mm}$ offset. The bar-graph in Figure 4.16 shows the maximum transmission values in relation to the different laser offset positions. The signals are normalized to the maximum transmission value ($\Delta_{tor} = 0\,\text{mm}$). In parallel, a calculation (simulation) was performed based on the one dimensional convolution of a Gauss-function (Laser diameter $\varnothing = 27\,\text{mm}$) having the same offset values with a rectangular function (Toroidal aperture opening of BL00005 $d_t = 4\,\text{mm}$) .

The simulation shows a symmetric decrease of the maximum transmission values for both offset directions, which is as expected. This is in contrast to the measurements, which are displaced to the left in the bar-graph and correspond approximately to a shift of $\Delta_{tor} = -0.8\,\text{mm}$. Figure 4.17 shows the normalized transmission measurements from both extreme values and the center value. Here, the effect on the transmission characteristic can be analyzed. The trapezoidal signal changes into a form of a breaking wave, for $\Delta_{tor} = -5\,\text{mm}$ into the positive toroidal orientation and for $\Delta_{tor} = 5\,\text{mm}$ in the negative orientation.

The signal decrease and increase towards its maximum is enhanced on its respective side. Here, the effect is relatively small, in particular considering that an offset of 5 mm is a worst case deviation for the ITER prototype measurements conducted in the laboratory. However, for larger aspect ratios of aperture and laser beam and more difficult measurement environments
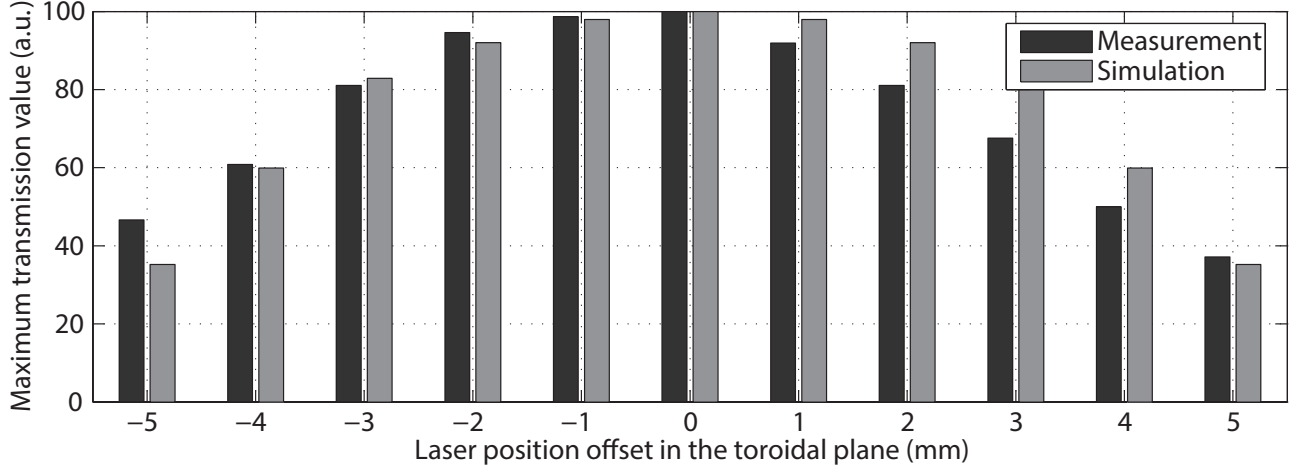
**Figure 4.16:** The bar-graph shows the transmission values of different laser offset positions. The signals are normalized to the maximum of the value with no offset (0 mm). The measurements can be compared with a simulation of the laser offset.
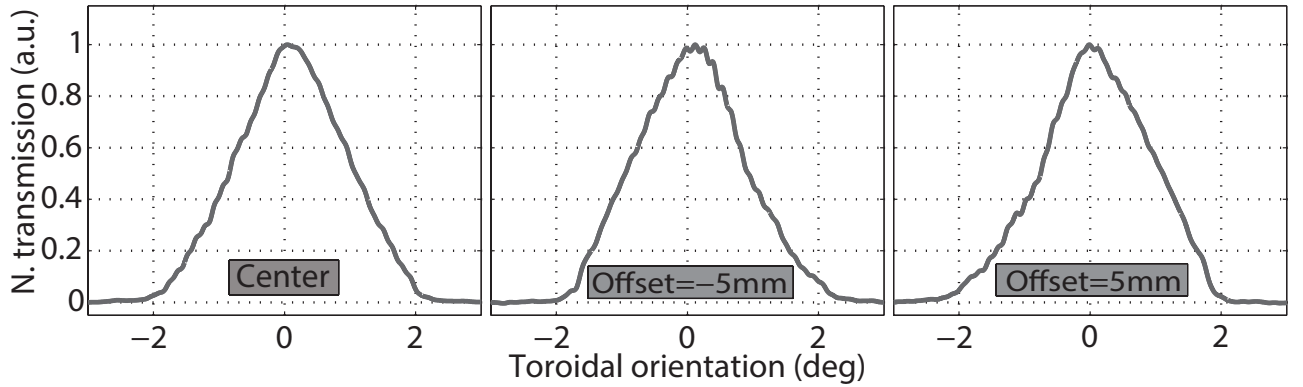


**Figure 4.17:** One dimensional toroidal transmission measurement with an offset in the toroidal plane. The plot on the left shows the original trapezoidal characteristic, the transmission with the offsets are changing to a breaking wave form.

this effect will be enhanced, see the results in the following AUG bolometer measurements, e.g. Figures 4.23 and 4.24.

The radiation source setup could be improved if the beam expander ratio to the maximum aperture opening (poloidal and toroidal orientation) would be so large, that inaccuracies of the laser positioning on the aperture center or the Gaussian beam shape cannot influence the transmission measurement. A larger beam expander (50x) combined with a more powerful laser ($\approx 1\,\mathrm{W}$) should be sufficient. Alternatively, a laser providing a top-hat beam profile could be combined with the existing beam expander. More laser power would also improve the overall signal quality because the DAQ could be operated in its optimal operation range. For the measurements presented here, the AD converters have been working only within 30% of their capacity which can be seen in Figure 4.15. The maximum bolometer bridge voltage $Max\,[U_{bolo}(\varnothing_4 \approx 27\,mm)]$ reaches $3\,\mathrm{mV}$ for a $10\,\mathrm{mV}$ A/D operation range.

## 4.2 ASDEX Upgrade bolometer measurements

For demonstrating whether the developed measurement procedures really are suitable for the operation in a tokamak environment IBOROB was operated in ASDEX Upgrade during a regular shutdown period to measure the characteristics and orientation of the integrated bolometer cameras. This section presents the results and integration challenges of this first setup.

### 4.2.1 Integration of IBOROB in ASDEX Upgrade

Tokamak experiments with the size of ASDEX Upgrade alternate regularly between an experimental campaign and a shutdown phase. During the years 2013-2014 an eight month shutdown of ASDEX Upgrade took place to perform regular maintenance of the vessel and to conduct major upgrades. Many scientist want to work with the experiment, therefore the access inside the vessel in this period is chronologically organized. IBOROB was assigned a time slot of one day shift and two weeks of night shifts because the whole vessel is blocked for other work due to the usage of the Class 3B laser source (see Chapter 3.2.2). As a security measure, all remaining open ports had to be closed or blocked during the operation of IBOROB. Thus, apart from the first day, the measurements were usually configured in the afternoon and run over night. The next morning the measurement had to be finished in order not to interfere with other work being conducted in the vessel. During the day, the robot had to be moved in a parking position very close to the inner wall not to obstruct other work.

Two persons are needed for the complete installation of the robot including the mounting device. The LWR is inserted in a special folded position, forming a U-shape in order to fit through the A-Port. Mounting the LWR in the straight position, which is the standard transport alignment from the manufacturer is not possible due to space restrictions. A plastic sledge padded with foam is used to transport the robot through the A-Port, minimizing damage risks and non-uniform loads on the multiple axis due to protective reasons. This is particular important because the vessel is too small allowing the straight position which is necessary for the axis readjustment with the vernier scale of certain axis. A metal floor plate is inserted in the divertor area thus allows the freedom of movement in the vessel and the manual transport of IBOROB to its position in the torus. At first, the mounting device is connected to the inner vessel wall, with a few PFCs being partly removed to allow the access to the screw holes, and then the LWR is installed.

### 4.2.2 Determining the optimal position in the experiment

Before inserting such a complex device in the vessel, an extensive testing of the IBOROB functionality had to be performed in advance. The robot can generate powerful forces, therefore

it must be ensured at all times that the robot does not damage other components in the experimental vessel or itself during the operation. The KUKA LWR is very sensitive, any collision usually causes a complete halt or even a mechanical damage to the brakes or engines of the robot.

Standard security measures in robotics, such as defining prohibited zones for the TCP or a representative point in the center of the payload and limiting axial angles have been implemented in the control algorithm (see KUKA LWR manual [132]). However, the space is limited to such an extent in the vessel, that if too stringent security settings were defined in the internal control algorithms, the robot would be limited too much and would not be able to perform the measurement task. For instance, the divertor width is only about twice as large as the laser and beam expander length. Moreover, defining a safe distance from the vessel wall is possible for the TCP but not for each axis. Thus, it can not be guaranteed that one axis moves in an unwanted direction while e.g. folding the robot arm (see Chapter 3.3.1).

Finally, the axes limitations strongly depend on each other. A disproportionately complex trajectory analysis of the many possible solutions would have been necessary to asses all these parameters [135]. Because the robot will only have to perform a limited amount of movements (due to the limited amount of cameras) and in order to ensure that everything will work well, the movements and different available positions have been tested within a spare replica of an octant of ASDEX Upgrade, which generates a realistic simulation of the vessel internal environment. For most of the new extensions of the experiment, especially the ones with large geometrical properties, this is a crucial test for qualification of the engineering feasibility. It consists of an empty ring representing two sectors of the torus. Depending on the situation, users can add additional components.

Here, several camera mock-ups have been placed in the test octant including the FAROArm (see Chapter 3.4.1) and the IBOROB mounting device (see Chapter 3.2.3) simulating a similar assembly as during the real measurement. The CS calibration procedure has been tested but also e.g. if the measurement arm reaches all necessary points (camera housing edges of all bolometer cameras) from one position. In particular the collision-free path and motion planning, the choice of the axis alignment and the definition of the enfolding direction of the central axis (`A3`) have been assessed. All possible "show stoppers" had to be identified early, since the access periods during the shutdown of ASDEX Upgrade are very limited.

In order to optimally position IBOROB in the limited space between the inner and outer vessel wall, the following four criteria have to be balanced against each other:

- The accessibility of measurable LOS.

- The measurement of different bolometer cameras.

- The achievable measurement accuracy which depends on the position.

- The degree of freedom of the robot with respect to the measurement area.

The changeable parameters are:

- The robot can be mounted in between the Sectors 4/5/6 due to the bolometer positions in Sector 5.

- The four different alignment positions of the robot with the mounting device (90° steps).

- The operational distance between laser and bolometer aperture.

- The total effort relating to the necessary experimental time.

As the measurements will have to be conducted within a given period of time, the driving force behind the choice was mainly to simplify the whole procedure. Based on the above named issues, a single horizontal alignment of the robot to the left (counter clockwise in the torus) in Sector 5 has been chosen in order to reduce the complexity for the first setup. A picture of IBOROB mounted in ASDEX Upgrade aiming on a FHC bolometer camera can be seen on Figure 4.18. The Figure shows one person (center) programming the remote control software (see Chapter 3.3.6) and the other person (right) holding the manual control in order to intervene (with the deadmanshandle) in case the robot shows unplanned behavior. Here, the laptop is connected via a wireless connection to the network of the experimental vessel which in turn is connected with the PXI system running the remote control interface.

An installation of IBOROB in Sector 6 would allow a good access of the FLX and FHC cameras but would provide only a very limited access to the FVC camera. For a position in Sector 4 the situation would be even worse, consisting of the entire loss of access to the FLX camera. Therefore, the position in Sector 5, radially in front of the FHC camera, is optimal. However, the FHS camera is excluded for all settings. This camera is located too close to the mounting position on the inner heat shield and the scanning area wouldn't be sufficient. A complete different design of the mounting device would have been necessary to measure this camera.

The advantage of the sidewise mounting on the inner wall is that the central Axis `A3` can be moved across a wide vertical working range, from the divertor to two-thirds of the height of the vessel. In particular, axis `A1` can be used over a much wider movement range ($\pm 90°$) than if the robot had been mounted vertically. Moreover, axis `A1` and `A5` are mostly perpendicular to each other, thus optimally aligned to perform a poloidal movement while remaining aligned on the bolometer aperture. The same applies for axis `A2` and `A6` for the toroidal orientation.

### 4.2.3   Motion planning issues

After the choice of the position, the motion planning for each camera has to be developed. Apart from finding feasible paths inside the confined spaces of the experimental vessel, a rectangular measurement field has to be defined in advance (see Chapter 3.4.3) for each camera. Then, for each measurement, the robot has to move from the park position to the start position of the measurement. However, this movement already involves major axis motions so that this step

**Figure 4.18:** Photo of IBOROB operating in ASDEX Upgrade. The laser points on the FHC camera. Two scientist are in the vessel during the installation procedure, one is supervising the manual robot control, mainly due to safety reasons, and the other one controls IBOROB via the remote control interface (see Chapter 3.3.6).

has to be approached gradually or divided into a number of smaller steps in order to avoid vessel collisions.

Moreover, singularities play a significant role for the motion planning of robotic manipulators. They are caused by a particular arrangement of robot axes resulting in unpredictable robot motion or the breakdown of the robot because the control algorithm cannot decide how to continue the motion. Here, due to an additional constraint of the fixed orientation (poloidal and toroidal orientation of the end effector with laser and beam expander) and the constant aiming onto the bolometer aperture, the freedom of the robot is further reduced. Constraint singularities can appear, which makes it particularly problematic. These configurations must be avoided for the faultless operation because if a singularity is present in the actual rectangular measurement field, the kinematic chain degenerates abruptly and a certain position cannot be passed.

From the main robot motion commands (`LIN`, `PTP`, `LIN REL`, `PTP REL` [132]), IBOROB was programmed for the vessel measurements using Point to Point Relative Movements (`PTP REL`) movements. This command constrains the internal robot control algorithm as little as possible, only the start position and the end position at a fixed toroidal or poloidal orientation of the

laser (and beam expander) is set. The rest is left to the robot control algorithms as a freely determinable parameter. For instance, the orientation of the laser axis (Z-Axis in the laser CS, see Figure 3.4) is not constrained, which results in being more fail-safe. However, this can lead to a slight rotation of the laser axis, but due to the rotationally symmetric laser it does not have any influence on the measurement signal. Furthermore, proper rectangular scanning areas cannot be defined exactly (see Figure 4.23), but this has also no implications on the data evaluation.

An example of the measurement movement is shown in Figure 4.19. It shows the toroidal and poloidal orientation of the laser and beam expander in the bolometer CS over time. The data is taken from a section of the movement during the measurement of the FHC camera (see Chapter 4.2.5). Each poloidal step ($\delta_\xi = 0.15°$) is followed by a complete toroidal measurement ($\Delta\theta = 30°$). Then the robot moves back to the initial toroidal position. Subsequently multiple toroidal (one dimensional) measurements of the LOS are recorded. It can be seen, that during the re-positioning of the robot after each toroidal measurement the poloidal alignment is shortly not maintained (blue peaks). This is a typical behavior for a PTP movement.
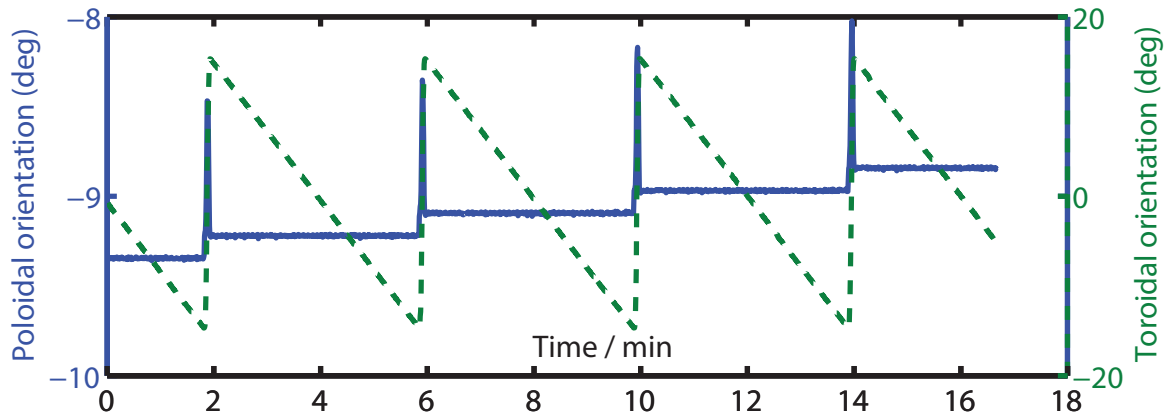


**Figure 4.19:** Toroidal and poloidal orientation during the two dimensional measurement of an ASDEX Upgrade camera. Toroidal (in green on the right axis) and poloidal (in blue on the left axis) orientation in the bolometer CS versus the time. After each toroidal scan of $\Delta\theta = 30°$, a poloidal step of $\delta\xi = 0.15°$ is performed. The spikes in the poloidal orientation are due to the PTP re-positioning.

### 4.2.4 Measurement of global coordinate system alignment

The global alignment of the robot CS in the torus CS has to be absolutely calibrated, in order to make global statements concerning the in-vessel LOS alignment. Therefore, the method described in Chapter 3.4.1.2 is applied. The schematic drawing of all involved components can be seen in Figure 4.20. It shows an isometric view of the vessel. The two large circles on the right represent the inner vessel wall and the reversed C the Sector 5. All three cameras (FHC, FLX, FVC), which could be accessed in the area of Sector 5, are indicated. The IBOROB CS is located in the center of its circular robot foot and the same applies for the FaroArm CS being

in the center of its circular attachment. The origin of the ASDEX Upgrade CS is defined in the center of the circular tokamak vessel. All CS are represented by three arrows, the bolometer cameras, which have multiple apertures, require also multiple CS (compare Figure 2.8).

The calibration movements in order to determine of the orientation of the robot CS are represented by lines forming a cross ($\pm X, \pm Y, \pm Z$). The advantage is that the position of these movements can be freely selected and their exact length is irrelevant. Objective is to derive the orientation and this can be done by connecting the start and end points of these motions. Next step is then to derive a CS from these constructed lines. The origin can be determined from the robot foot position.
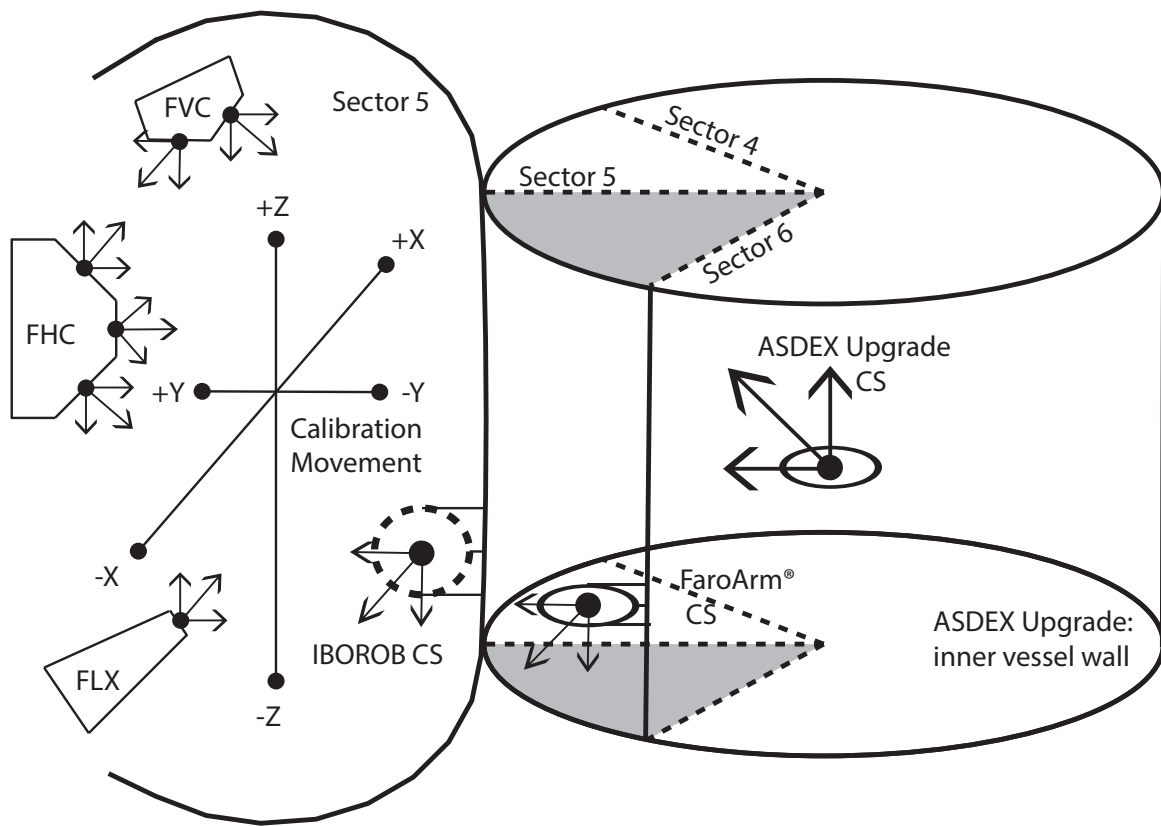


**Figure 4.20:** Isometric view of absolute CS measurement with FaroCam2Measure Software. The CS of IBOROB and ASDEX Upgrade are indicated. The housings of the bolometer cameras FVC, FHC and FLX are shown. Black dots indicate the aperture center.

The FaroArm is connected to the inner heat shield in Sector 6 with a mounting device comparable of the one for the robot. The measuring tip can reach all necessary points from this position. A schematic toroidal view of the relevant Sector 5 boarding Sectors 4 and 6 can be seen in Figure 4.21. The inner vessel wall is on the right and an A-Port, similar to the one used to enter the vessel, is on the left. As shown in the previous figure, the position of IBOROB, the FaroArm and the positions of the measured bolometer cameras are indicated. The approximate toroidal orientation of the bolometer LOS, as derived from theoretical calculations (see Chapter 2.2.3), are indicated in red. The green line is a measured reflection which will be explained in Section 4.2.5.1.
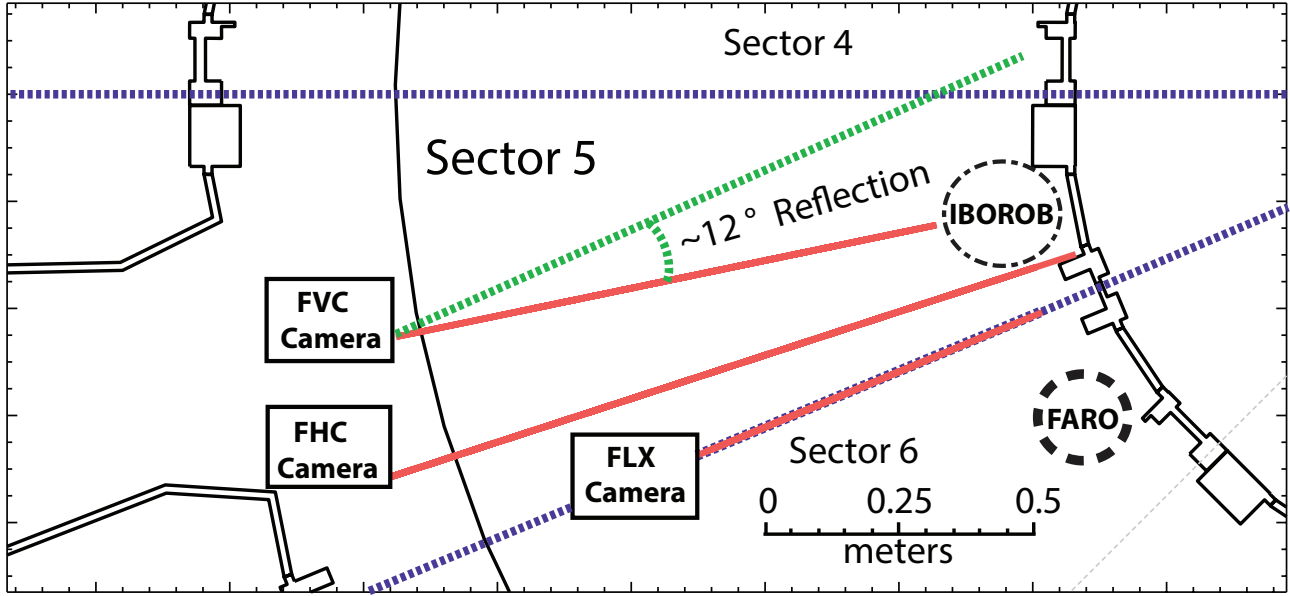
**Figure 4.21:** Toroidal view of Sectors 4,5 and 6 of ASDEX Upgrade. The positions of the three measured bolometer cameras FVC(left), FHC(left) and FLX(middle) are indicated with boxes. IBOROB is mounted via the mounting device (see Chapter 3.2.3) onto the inner heat shield of the vessel (dotted circle on the right). The theoretical toroidal LOS alignment is represented by the red lines. The green line connected to the FVC camera indicates the measured reflection angle. The dotted blue lines indicate the area of Sector 5.

Now, the FaroArm measurement tip is moved manually to all positions which are needed to calculate the position or orientation. Then, the respective positions (X,Y,Z) of the bolometer apertures and detectors can be transformed to the robot CS and then transferred to the control software of IBOROB. The calibration result can be quickly cross checked by pointing the laser CS to a defined position, such as the aperture center of a bolometer camera. If the laser beam is not in the center of the aperture, its is likely that a mistake has been made. Here, an evaluation by eye of the laser center did not show a larger deviation then $1 - 2\,\mathrm{mm}$ which is in the range of the absolute positioning accuracy of the KUKA LWR.

The absolute accuracy of a CMM can vary and usually depends on the stability of the mounting respectively of the amount of force interacting with the measuring arm parts. For our setup in a tokamak this is not optimal, but still a sufficient volumetric accuracy of $0.1\,\mathrm{mm}$ was achieved. This is in the range of normal operating conditions of the FaroArm in ASDEX Upgrade.

The torus system of ASDEX Upgrade is organized in 16 toroidal sectors each one spanning over $\Delta\Phi_{sectors} = 22.5°$. IBOROB is mounted in the center of Sector 5, which corresponds to $\Phi_{Sector5} = 101.25°$ ($4 * 22.5° + 1/2(22.5°)$). The software of the FaroArm calculated the actual position of IBOROB to be at $\Phi_{IBOROB} = 101.7°$. Thus, the position of IBOROB deviated $0.45°$ in toroidal orientation from its expected alignment in the vessel CS. All following required calculations for the coordinate transformations can be done using the features of the FARO Cam2Measure software.

### 4.2.5    Analysis of line of sight characteristics

In this section, the measurement results with IBOROB obtained in the vessel will be discussed. Figure 4.22 shows a poloidal cross-section of ASDEX Upgrade including the central poloidal orientation of the LOS. A CAD drawing of IBOROB has been added into the poloidal cross-section. For better visibility, the robot is shown in a vertical position, instead of the tilted one as used for the measurements (see Section 4.2.2).

The LOS broadening over its length, respectively the viewing cone, is not shown. It shall be noticed, that most of the viewing cones are as wide as the spacing between the LOS. Some channels, which will be mentioned in this work, are additionally numbered in the figure. The LOS marked in red could be reached with IBOROB, whereby the accessible toroidal angle range ($\Delta\theta$) may vary depending on the TCP position. For LOS situated more in the center of the vessel large toroidal ranges ($\Delta\theta \approx 20° - 35°$) are available, for LOS on the top or in the divertor only smaller measurement ranges ($\Delta\theta \approx 5 - 10°$).

The LOS which are passing close to PFCs can not be measured at all due to the size of the laser and beam expander. Finally, the accessibility is a trade-off between scanning many LOS or enabling a broad toroidal scanning range for the specific camera. The following measurement results will be presented:

- **FHC bolometer:** Nine channels could be accessed (Channel 16-23). Channel 20 is expected to be aligned almost horizontally at the poloidal angle of $\xi_{CAD} = 0.35°$. Therefore, this channel and the neighboring ones are the most simple to access due to their position radially in front of the robot. The results can bee seen in Figure 4.23 of Section 4.2.5.3.

- **FVC bolometer:** Channel 84 is a LOS which looks slightly downward in the direction of IBOROB and can also be accessed very well. In particular in toroidal orientation a broad measurement can be achieved ($\Delta\theta = 35°$). Figure 4.25 in Section 4.2.5.1 shows the result.

- **FVC bolometer:** 14 Channels could be measured within two consecutive measurements: Channels 73-86, with a poloidal angle from $\xi_{start} = -80°$ to $\xi_{end} = -20°$. See Figure 4.24 in Section 4.2.5.2 for the results.

- **FLX bolometer:** The camera which observes the divertor is located close to the bottom of the vessel and was difficult to access. Only the first LOS (Channel 102)- counting from top to bottom - could be measured completely, the second LOS (Channel 101) could only be accessed until about the first half of its viewing cone. No results will be presented because they do not contain additional information.
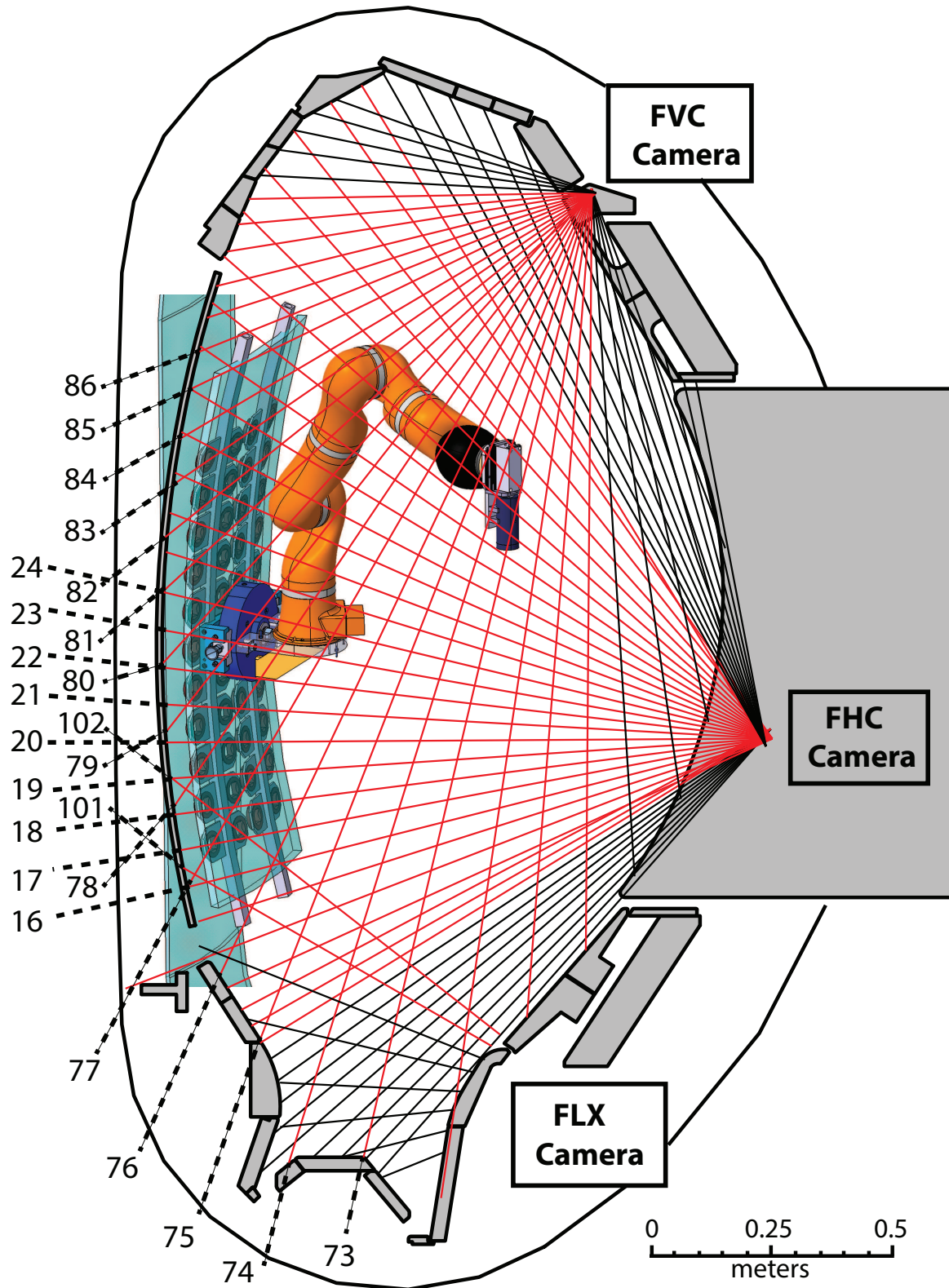
**Figure 4.22:** Diagram of a poloidal cross-section of ASDEX Upgrade with bolometer LOS merged into one poloidal plane including a CAD drawing of IBOROB mounted on the inner heat shield via the mounting device. The positions of the three measured bolometer cameras FVC, FHC and FLX are indicated with boxes. The LOS which were in the measurement range of IBOROB are marked in red. Additionally, relevant LOS channel numbers are indicated and a scaling has been added.

FHC and FVC can be measured with the TCP being in a distance of 300 mm from the camera pin hole. The FLX camera can only be measured in a very short distance of 130 mm due to the limited space available in the divertor. Furthermore, due to the limited time available, the measurement resolution had to be rather low. Therefore, all measurements presented in this section have been conducted with a robot step size (in poloidal and toroidal orientation) of $\delta_{\xi,\theta} = 0.15°$.

The bolometer DAQ at ASDEX Upgrade is usually used during the usual discharge times of 10 s. The developers tested the system during its development only with a data stream length of 30 s [45]. Performing measurements with a duration of multiple hours revealed an error in the analog to digital conversion. After a certain time of running the DAQ, the signal shows jumps at irregular intervals which suggest some kind of bit flipping error or buffer overflow. If the software created this error or if there was a hardware defect in the electronics could not be determined during this work. As a result, some acquired samples had strong signal fluctuations which introduced additional noise in the signal. On some channels it had a strong impact, others remained nearly unaffected (see Figure 4.25). Therefore, the measurement signals acquired with the ASDEX Upgrade electronics show a lower quality compared to the laboratory measurements. Additionally, it shall be noted that based on the experience of the ASDEX Upgrade bolometer operators, the vessel environment always introduced considerably more external noise compared to tests performed in the laboratory. However, the errors acquired here contribute mostly to a visual deterioration of the signal but don't compromise the conclusions based on the LOS assessment.

### 4.2.5.1   Detection of internal camera relflections

In this section, the detection of internal camera reflections with IBOROB will be discussed using the measurement result of the FVC camera Channel 84. One reason that the FVC camera has been selected for this analysis was, because the operators of ASDEX Upgrade were dissatisfied with the accuracy of that camera in the past, but could not identify the exact source of the error. Additionally, this channel could be accessed with maximum toroidal range compared to other channels ($\Delta\theta = 30°$, $\Delta\xi = 5°$).

In Figure 4.23 the two dimensional result of the Channel 84 from the FVC camera is shown in a contour plot. The expected alignment is $\xi_{CAD} = -30.6°$ in poloidal orientation and $\theta_{CAD} = 101.7°$ in toroidal orientation. The measured alignment is $\xi_{MEA} = -29.8°$ and $\theta_{MEA} = 102.6°$. Thus, it shows an error of $\theta_{error} = 0.9°$ and $\xi_{error} = 1°$ from the intended orientation. Furthermore, the maximum transmission values are not symmetrically in the center. This is probably due to a misaligned laser beam - a few mm offset from the center - as shown in Chapter 4.1.5.

This figure shows the DAQ signals from a single channel. A reflection, also known as a ghost image, which is defined in optics as an undesired duplicate image near the desired image, can
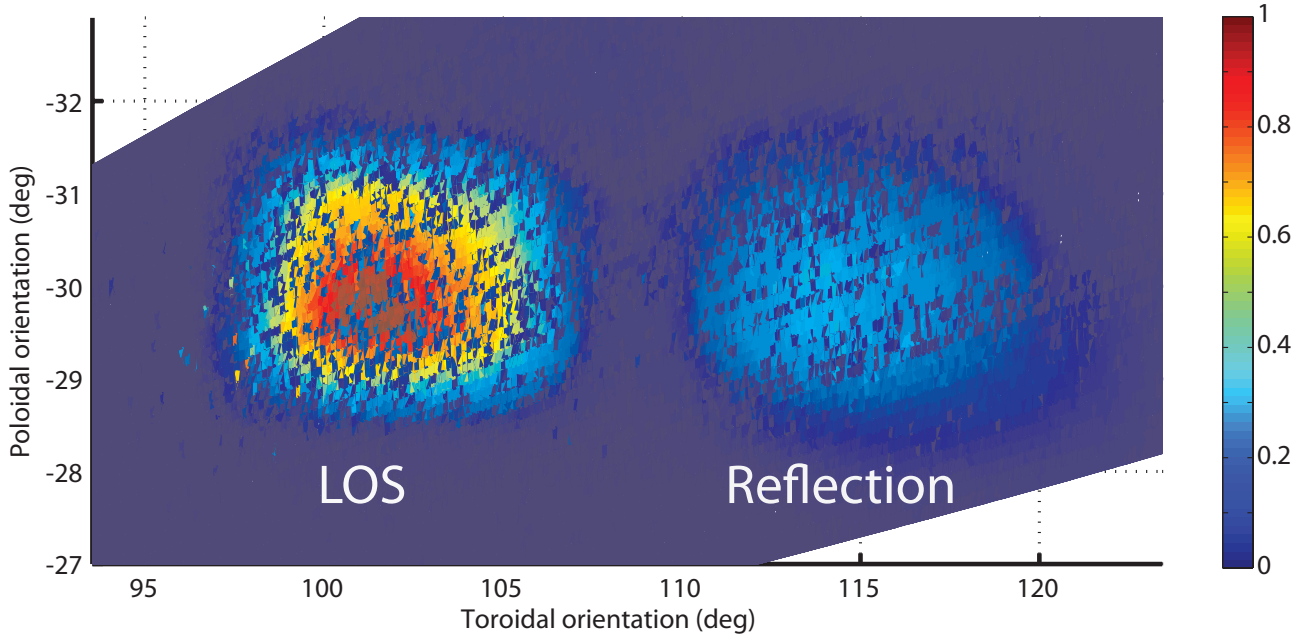
**Figure 4.23:** Contour plot of Channel 84 of the FVC Camera: Internal camera reflection can be identified. They are generated by the camera housing, which is made of reflective stainless steel plates.

be identified at a toroidal angular distance of $\theta_{REF} = 12°$. The poloidal orientation of the reflection is the same.

The reflection has an intensity of $\approx 30\%$ compared to the maximum of the main LOS. It can be expected that this reflection exists at least in the whole visible spectral range due to the similar reflection coefficients in this wavelength range. But in order to make assumptions about its fraction in broader spectral ranges, the specific reflection coefficients of the material, the surface characteristics of the housing material and the spectral power distribution have to be known.

The noise, which can be seen in particular in the signal of the main LOS is due to the DAQ errors. Unpredictable bit-flips are generating high and low signal peaks which are not related to the transmission characteristic. For lower absolute signal powers, e.g. in the reflection, they are less perceptible.

However, it is evident that the toroidal definition of the LOS is not as expected. Due to the curvature of the doughnut-shaped vessel each LOS with such a characteristic will measure an additional radiated power. When evaluating the signals using tomography, this leads to a misinterpretation of the radiation profile. In this context it shall be noted, that it is unwanted to have LOS looking in the toroidal flow direction of the plasma when performing tomography of a poloidal (!) cross-section. Also the effective length of the LOS is extended by 10-15% which results in even more light yield on the detector. The direction of this reflection is also indicated as a dotted green line in the toroidal cross-sectional view in Figure 4.21.

Following conclusions can be drawn: Firstly, due to the similar design of the ASDEX Upgrade cameras, it can be expected that the other LOS suffer from the same reflections in toroidal orientation. Secondly, this may also cover the poloidal orientation for LOS at the edge of the camera housing, depending on the specific camera geometries. Such reflections are not acceptable if the diagnostic should provide reliable data. A broadening of the transmission by 0.5° such as identified in the '12 ITER colllimator prototype deteriorates the measurement accuracy too, but it would be possible to integrate such a characteristic in the reconstruction alogrithm. However, for a reflection which deviates 12° from the intended alignment - due to the symmetric housing probably in both toroidal orientations (for Channel 84 $\approx \theta = 90°$) - a post processing or filtering of the data, even with exact knowledge of the experimental parameters, is almost impossible. Under the assumption of a worst case scenario (depending on the type of experiment conducted in the vessel) this channel could generate measurements several factors above the real value.

In Chapter 2.4.1, the ASDEX Upgrade bolometer camera design has been explained. The camera housing is made from stainless steel plates. In general, metals have a considerable high reflectivity in the visible and NIR spectrum which means that any radiation in this wavelength range will lead to increased stray light. Depending on the geometric conditions, this can lead to reflections in the housing comparable to the reflections due to the channel walls measured from the ITER prototype (see Section 4.1.3.2). Therefore, most of the cameras at ASDEX Upgrade had to be modified. They have been upgraded with custom grooved plate with a rough surface inside the camera housing in order to scatter and disperse the reflected radiation.

### 4.2.5.2 Absolute measurement of poloidal line of sight arangement

In the following, the absolute measurement of multiple LOS of the FVC camera will be presented. The result consists of two separate measurements which have been merged into one data set. During the first (1) measurement Channels 73-81 were measured and in the second (2) measurement, Channels 81-86. The measurements were performed in the two dimensional measurement mode with $\xi_{start}^{(1)} = -80°, \xi_{end}^{(1)} = -40°, \xi_{start}^{(2)} = -45°, \xi_{end}^{(2)} = -20°, \Delta\theta = 10°$.

Then, the two dimensionally acquired data has been integrated in toroidal orientation to generate a projection onto the poloidal plane, similar to the one dimensional measurement results shown from the ITER bolometer prototypes. The measurement result can be seen on Figure 4.24. For a better identification the LOS are marked with different colours and the legend on the top identifies the corresponding channel numbers. Additionally, the expected poloidal LOS alignment from the CAD is indicated with + signs at a value of 50% of the normalized transmissions.

When comparing the orientation of the measurement, it should be noted that Channels 73-76, 77-80, 81-84, respectively and 85-88 are each part of a four channel detector. Thus, slightly
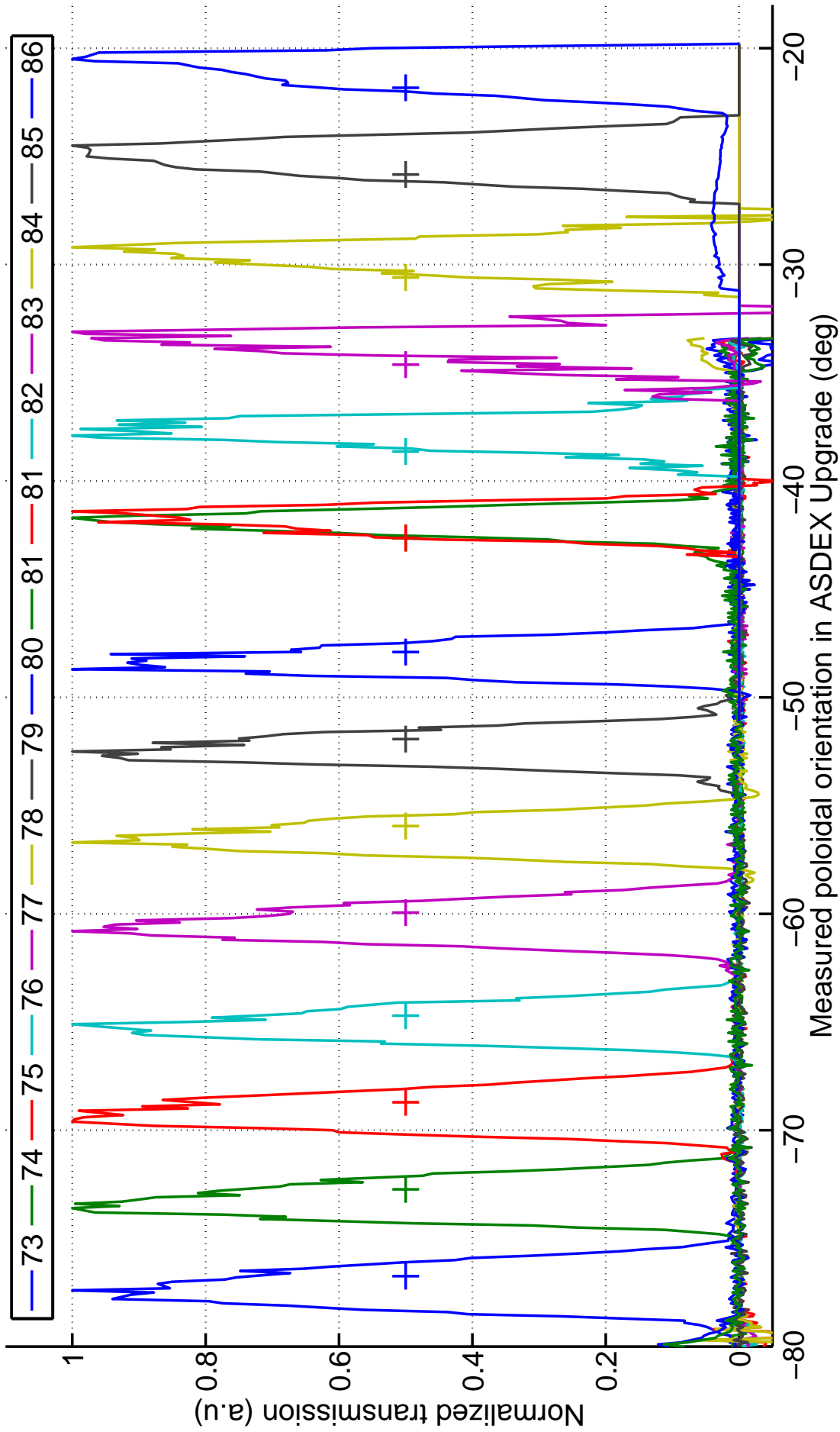
**Figure 4.24:** Measured poloidal transmission of the FVC bolometer camera for Channels 73 - 86. The data consists of two separate measurements. The theoretical expected orientation is indicated as + signs (shown at 50% normalized transmission).

larger gaps between the LOS can be identified between the Channels 76-77 and 84-85 in comparison to the other gaps. The FVC camera consists of multiple trapezoidal camera parts, which are separated by additional supports (see image of construction design of the FHC camera in Figure 2.8) for each adjacent four channel detector. Depending on the type of the support, the border between both camera parts can result in a larger gap, here between Channel 80 and 81.

In order to evaluate the alignment of each LOS quantitatively, the center (of gravity) is calculated by integrating each LOS over its signal shape: $\xi_{MEA} = \frac{1}{W_{LOS}} \sum k_\xi(\xi) \cdot \xi$, with $W_{LOS}$ being the (scalar) total transmission of all the transmission values of each LOS. Here, only transmission values above 20% have been taken into account in order to minimize the influence of the noise. The results are summarized in table 4.2.

**Table 4.2:** Comparison of measured and theoretically expected poloidal orientation of the FVC bolometer camera of ASDEX Upgrade. During the first (1) measurement Channels 73-81 were measured and in the second (2) measurement, Channels 81-86. See Chapter 3.5.2 concerning the measurement uncertainty.

| **FVC** | 73 | 74 | 75 | 76 | 77 | 78 | 79 | 80 |
|---|---|---|---|---|---|---|---|---|
| $\xi_{CAD}$ | $-76.74°$ | $-72.72°$ | $-68.70°$ | $-64.70°$ | $-59.94°$ | $-55.94°$ | $-51.92°$ | $-47.90°$ |
| $\xi_{MEA}$ | $-77.21°$ | $-73.18°$ | $-69.08°$ | $-65.06°$ | $-60.42°$ | $-56.40°$ | $-52.32°$ | $-48.23°$ |

| **FVC** | 81 (1) | 81 (2) | 82 | 83 | 84 | 85 | 86 | |
|---|---|---|---|---|---|---|---|---|
| $\xi_{CAD}$ | $-42.63°$ | $-42.63°$ | $-38.63°$ | $-34.62°$ | $-30.59°$ | $-25.83°$ | $-21.82°$ | |
| $\xi_{MEA}$ | $-41.88°$ | $-41.81°$ | $-37.71°$ | $-33.65°$ | $-29.60°$ | $-25.04°$ | $-21.04°$ | |

Comparing the measured absolute poloidal orientation of the LOS ($\xi_{MEA}$) to the expected values ($\xi_{CAD}$), a maximum difference of 0.99° (Channel 84) can be observed and a minimum difference of 0.33° (Channel 80). The LOS of the Channels 73-80 equally deviate in the negative poloidal direction, for Channels 81-86 they deviate in the positive direction. It is likely that the size of the supports between Channel 80-81 do not exactly correspond to the CAD parameters of the camera design. However, it has to be admitted, that this is a difficult task due to the manual assembly of the camera and supports in the vessel.

But the relative poloidal spacings between each channel within a detector are constant and within the scope of this measurement accuracy. The expected distance between each channel is 4.0°. The measured distances are 4.03° for (Channel 73-74), 4.1° for (Channel 74-75) and 4.02° for (Channel 75-76). These relative values depend only on the detector cover manufacturing accuracy (component can be seen in Figure 2.1 F) and as this component is machined in one piece, it is unlikely to have a large variance in between the four detector openings.

From the measurement of Channel 81, which has been measured twice, the accuracy of the measurement procedure can be cross checked. The measurements have been done during two different nights, thus the robot has been moved in the park position in between. Moreover, the axis of the robot have been oriented in complete different positions, which can be considered as a worst-case scenario for the absolute position accuracy of the robot. However, the difference between both measurements is very small: $\xi_{CAD}^{Channel81(1)} - \xi_{CAD}^{Channel81(2)} = 0.07°$.

Another effect that needs to be discussed in this context is that the LOS shape form the first measurement (Channels 73-81) shows a steeper rise of the transmission than the descent. In contradiction to the second measurement, which shows the opposite: A steeper descend than rise of the signal, in particular for Channels 83-86 (Channel 83 has been excluded for this analysis due to the strong noise). This effect is caused from a constant horizontal shift of the laser center in respect to the pin hole and has been explained in Chapter 4.1.5.

The ASDEX Upgrade bolometer cameras are particularly vulnerable to that effect because the poloidal pin hole width of the ASDEX Upgrade bolometers is larger than the average ITER bolometer apertures. As explained in Chapter 3.2.2, the beam expander generates a beam output of a diameter $\varnothing_{las} = 27\,\mathrm{mm}$. For a poloidal aperture width of $5\,\mathrm{mm}$, positioning inaccuracies will modify the signal shape. However, the center of gravity of each LOS is not affected strongly.

### 4.2.5.3 Two dimensional measurement of line of sight distribution

Figure 4.25 shows a contour plot of a single two dimensional measurement of the FHC camera Channels 16-23. This measurement was conducted with a toroidal and poloidal resolution of $\delta_{\xi,\theta} = 0.15°$ and a scanning area of $\Delta\xi = 30°$ and $\Delta\theta = 12°$ acquiring $\frac{\Delta\xi * \Delta\theta}{(0.15°)^2} = 16\,000$ samples within $5\,\mathrm{h}$. Each channel is marked in the plot. Channels 16, 17, 21, 22, 23 and 24 are fully operational and are used for the evaluation. No bolometer bridge voltage could be measured from Channel 18, respectively no calibration data could be obtained from the LabVIEW program, which suggests that the detector meander is broken. Channels 19 and 20 are strongly perturbed by bit flipping errors of the bolometer DAQ, thus only signals above relative values of 50% have been added to the plot for this channels.

Dotted lines were integrated into the plot to indicate the theoretically expected poloidal orientation ($\xi_{CAD}$) of the detector and camera alignment, exemplary for Channels 17 and 23. All FHC camera channels are supposed to be toroidally aligned at $\theta_{CAD} = 108°$. A comparison of the toroidal orientation from the measurement with the expected one shows a rather good agreement for the Channels 21-24. However, the Channels 16-20 show a constantly increasing deviation from $\theta_{error}^{min} = 0.5°$ to $\theta_{error}^{max} = 2.5°$ from the expected orientation. In this camera, Channels 24-21, Channels 20-17 and Channels 16-12 are grouped in independent detector holders within the camera. Therefore, a small inclination of a few degrees of the four channel detector mounted inside the camera could be responsible for these different deviations.

Finally, only the sum of all influencing parameters can be measured. A dedicated analysis, e.g. separating the individual error sources as performed with the ITER prototypes in the
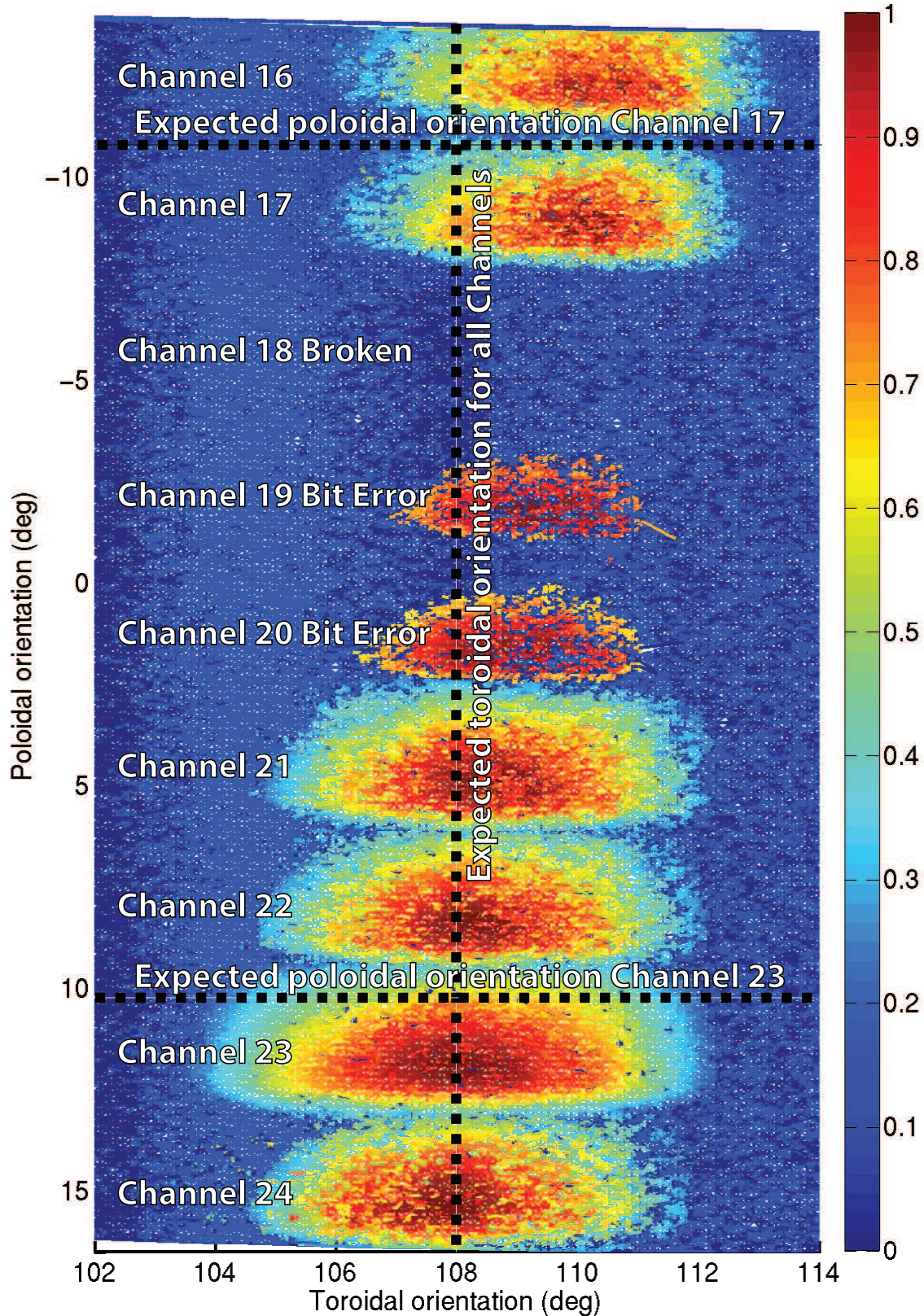
**Figure 4.25:** Contour plot of the calibration measurement of the FHC bolometer camera. Channels 16 - 24 are plotted in the torus CS. Channel 18 is broken. The DAQ in Channels 19 and 20 suffered from many bit errors, thus only values above 50 are plotted. The expected orientations in toroidal and poloidal direction of Channels 17 and 23 are indicated as well.

laboratory, is not possible when performing vessel measurements. A horizontal tilt of the whole camera would only explain an equal misalignment of every channel (see Chapter 2.4 explaining the ASDEX Upgrade camera design). Here, it is probably a combined error of an inaccurately aligned detector within the camera and the camera itself.

Concerning the poloidal orientation, the divergence has a constant value $\xi_{error} \approx 1.8°$, which can be assigned to a horizontal tilt of the camera. Table 4.3 shows a summary of the exact values of theoretically expected and measured orientation. Again, only transmission values above 20% (values with light blue in the contour plot) have been taken into account (values above 50% for Channel 19 and 20) for the center of gravity calculations.

**Table 4.3:** Comparision of measured ($\xi_{MEA}$, $\theta_{MEA}$) and theoretically expected orientation ($\xi_{CAD}$, $\theta_{CAD} = 108°$ for all channels) of the FHC bolometer camera Channels 16-24 of ASDEX Upgrade. The measured Etendue ($Et_{MEA}$) is normalized to Channel 24 and can be compared to the expected value ($Et_{CAD}$). See Chapter 3.5.2 concerning the measurement uncertainty.

| FHC | 16 | 17 | 18 | 19 | 20 | 21 | 22 | 23 | 24 |
|---|---|---|---|---|---|---|---|---|---|
| $\xi_{CAD}$ | $-14.24°$ | $-10.67°$ | $-7.23°$ | $-3.79°$ | $-0.35°$ | $3.22°$ | $6.65°$ | $10.10°$ | $13.53°$ |
| $\xi_{MEA}$ | $-12.47°$ | $-8.91°$ | | $-2.08°$ | $1.67°$ | $4.94°$ | $8.42°$ | $11.97°$ | $15.24°$ |
| $\theta_{MEA}$ | $110.5°$ | $109.9°$ | | $109.3°$ | $109.1°$ | $108.5°$ | $108.2°$ | $108°$ | $107.9°$ |
| $Et_{CAD}$ | 0.863 | 0.892 | 0.927 | 0.948 | 0.955 | 0.970 | 0.992 | 1 | 0.992 |
| $Et_{MEA}$ | 0.668 | 0.705 | | | | 0.922 | 0.964 | | 1 |

From this data, the Etendue of each channel has been calculated by integrating over all transmission values of each respective channel (see Chapter 2.2.3). The reason that the Etendue values are different, is due to different tilt angles of the detector towards the aperture pin hole and due to their different positions in the camera housing affecting the effective aperture size (see Figure 2.7 B).

The challenge for the analysis is, that the measured channels have a different noise level which significantly influences the results when integrating the data. Channel 23 has a much better signal quality then the other channels, which thus results in a much higher Etenude, therefore it was excluded from this calculation. Here, the Etendue values have been normalized to the maximum value of Channel 24 because it has the maximum theoretical Etendue[1] ($Et_{CAD} = 0.992$) from the remaining channels. Comparing the values in the Table 4.3, it can be seen that the measured Etendue represent the theoretical values well, in particular the differences between adjacent channels (2-3%), taking into account the variations of the noise levels. Channel 21, 22 and 24 show the largest Etendue and Channel 16 and 17 show a slight decrease which can also be seen comparing the differences of the geometrical size of the LOS in the plot.

Considering the LOS shape, two differences of the expected characteristics can be recognized: Firstly, the LOS maximums are systematically dislocated in the positive poloidal orientation which suggests that the laser beam was not accurately positioned on the pinhole aperture open-

---

[1] A normalization to Channel 22 results in values differing by 1%

ing (see Chapter 3.2.2), just as the measurement presented in the previous chapter. Secondly, due to the two dimensional visualization as a contour plot, it can be seen that the toroidal width is decreasing in negative poloidal direction forming a trapezoidal shape.

For the bolometer cameras of ASDEX Upgrade can be concluded that the LOS alignment shows deviations in the range of several degrees. This result should be taken as an input value for accuracy considerations regarding the installation of future vessel components. Concerning most diagnostics in a tokamak experiment, the deviations in toroidal orientation are only a minor problem. The impact on the measured quantities (for bolometry the radiated power) will be rather small due to the toroidal symmetry of the vessel. But the deviations in poloidal orientation affect the spatial accuracy of e.g tomography, thus have to be taken into account for the future.

## 4.3   Implications for the bolometer diagnostic of ITER

Misaligned LOS in poloidal or toroidal orientation of $1° - 3°$ are not a serious problem for a medium-size tokamak like ASDEX Upgrade. Certainly, it is difficult to deduce plasma physical phenomena from inaccurate tomographic reconstructions, but the diagnostic is still performing in terms of providing a representation of the total radiated power. However, if this error is extrapolated towards ITER, note that the size of the vessel is increased by a factor of four compared to ASDEX Upgrade, the negative impact of these deviations concerning the spatial resolution of the diagnostic would be intensified. A poloidal misalignment of $3°$ for a camera LOS with a length of up to seven meters looking from the top into the divertor would lead to a misalignment of $36\,\mathrm{cm}$. This means that the reconstructed radiation profile would contain significantly blurred areas because the size of radiating structures is usually in the order of $5 - 10\,\mathrm{cm}$. In particular, misaligned LOS monitoring areas with strong gradients, such as the area around the X-point, would not be resolved properly.

Furthermore, due to the installation constraints of the bolometer cameras in the ITER vessel (see Chapter 1.3.1), the main problem will be a shadowing effect from the BMs. Undetected misalignments could result in a LOS with a channel Etendu of merely half the expected value or in the worst case being completely obscured. This cannot be accepted for a diagnostic which is intended to provide data for the basic machine protection. If partly shadowed LOS remain unidentified the accuracy for the ITER plasma control system will not be reached and dependable tomographic reconstructions will not be possible.

Therefore, there are two options: Either the overall installation accuracy of the ITER components will be one order of magnitude better than that of ASDEX Upgrade ($0.1° - 0.2°$ instead of $2° - 3°$) or a similar LOS measurement system will have to be developed for ITER. Considering that ITER will still be an physics experiment and not a power plant, which means that the vessel will be modified on a regular basis, the latter is highly recommended.

**Essential requirements for a LOS measurement system for ITER**

A LOS measurement system for ITER would be more complex in several dimensions compared to IBOROB operating in ASDEX Upgrade in particular considering the challenges posed by the harsh ITER environment. Firstly, it will be difficult to procure a manipulator directly from the industry which tolerates the radiation environment conditions in the vessel after D-T operation. Thus, a dedicated development will be necessary [137]. Secondly, due to the toroidal distribution of the cameras in the vessel, the whole circular vessel needs to be accessed. This means that the manipulator will have to be able to move independently between different sectors.

A manipulator similar to the Articulated Inspection Arm [138] robot used at Tore Supra[1] or the 10 metre long articulated boom called MASCOT at JET used for the in-vessel inspection [139] would be a good example. If a dedicated system cannot be realized, the LOS measurement device could be integrated on a RH system for ITER already being under development. The In Vessel Viewing System (IVVS) [140], which is an articulated inspection arm with the objective to perform inspection tasks and gather metrology data within a certain spatial accuracy, could be further enhanced to perform this task. Another possibility would be to use the in-vessel transporter of the ITER blanket module maintenance system. This transporter is composed of a vehicle and a rail and could be used as a carrier system for an attached LOS calibration manipulator. Because of the larger vessel size, the calibration movements could then be performed at a larger distance from the detector enhancing the angular accuracy of the transmission measurements. Therefore, the absolute position accuracy requirements of such a manipulator could be lower than for ASDEX Upgrade. However, the accessible positions could be limited by the capabilities of the transporter.

---

[1]Tore Supra is a French superconducting tokamak, situated at the nuclear research center of Cadarache

# 5. Summary and outlook

The research performed in this work consisted of two main tasks: First, the development of an automated measurement system, which allows to measure the LOS characteristics and alignment of bolometer cameras in order to assess and optimize the LOS transmission of different bolometer collimator prototypes currently under development for ITER. Secondly, to prove that the developed measurement device is capable to determine the geometric LOS properties in situ in a tokamak environment with sufficient precision by demonstrating its operation in ASDEX Upgrade.

The developed measurement system named IBOROB is based on a seven axis KUKA lightweight robot with a mounted laser and beam expander serving as radiation source. The required remote control software was realized in a LabVIEW program and allows the real-time monitoring of all processes. It includes the control of the bolometer DAQ, the triggering of the laser and the motion planning of the robot. Several mechanical mounting devices have been manufactured to allow an installation in the laboratory or directly in the experimental vessel. In a fully automated process, the system can determine the two-dimensional transmission function of a bolometer camera at a very high resolution. The results can be interpreted directly, no post processing of the data is needed, the LOS transmission is the direct output from the measurement device. In a global CS, such as the tokamak CS, an external CMM device is required to calibrate the system. Depending on the external constraints, the camera characteristic and alignment can be assessed with a sufficient angular uncertainty of $\Delta \approx 0.1 - 0.2°$ which corresponds to the angular accuracy needed for the alignment of the ITER bolometer components.

IBOROB was first thoroughly tested in a fixed laboratory setup by evaluating its accuracy and developing calibration procedures for its components. Then, the transmission of the ITER collimator camera prototypes was measured, which are currently in the stage of development at IPP. The main objective was to identify the driving design components influencing the LOS characteristics and to validate the design parameters of the camera, in particular to verify how well the theoretically desired transmission can be reached under ITER boundary conditions. In this work, two exemplary camera aperture designs have been built and analyzed with respect to their transmission characteristics.

The first prototype collimator design (Model '11) consisted of channels which were wire eroded over their whole length. This design ensured superior thermal properties advantageous for an operation in ITER, however, the transmission measurements showed that the LOS resulted in being almost twice as large as described by theoretical calculations. Due to the very smooth surface of the channel walls an excessive amount of reflections was generated which broadened the LOS.

Thus, an improved ITER collimator prototype camera version (Model '12) was developed which could be equipped with multiple apertures reducing the potential reflective surfaces. As a result, the transmission characteristics improved. But particular aperture configurations with the objective of achieving extremely narrow LOS widths ($\Delta\theta_{FWHM} \approx 0.6°$) did still not reach the target properties adding about 30% additional stray light. However, the advantage of the new modular design was that each part of the camera could be be inspected individually by comparing different configurations with each other. A measurement campaign was carried out in order to identify each component of the camera having a negative impact on the transmission characteristics. As a result, reflections due to the integrated channel borders in the collimator housing, reflections from the housing itself and reflections inside the apertures have been discovered. Moreover, a signal modulation induced by a necessary microwave filtering grid in the top plate of the collimator could be identified. Finally, all major optical effects influencing the LOS transmission of the bolometer camera design could be determined and characterized. The results have been summarized, measures necessary for the prevention of stray light were derived and a concept for a significantly improved camera design (Model '13) could be developed.

Furthermore, in order to qualify IBOROB as an in situ compatible device being able to operate in a tokamak environment, the device was deployed within a regular maintenance shutdown for the first time in the tokamak ASDEX Upgrade. The alignment and characteristics of multiple LOS from different cameras at different positions of the vessel have been measured. Thus, the accuracy of the camera assembly, the installation and the final orientation in the vessel could be compared with the design values.

It was found that some LOS are deviating up to 2°-3° from their theoretically expected alignment because of tolerances in the camera construction or inaccuracies during the installation. LOS deviations in the toroidal orientation in this magnitude are not a major problem for ASDEX Upgrade due to the toroidal symmetry of a tokamak experiment. However, deviations in poloidal orientation are definitely influencing the spatial accuracy of the bolometer diagnostic and have to be incorporated in the tomographic reconstruction algorithms.

In addition, a systematic problem with the design of the ASDEX Upgrade camera housings has been identified. Measurements covering a wide toroidal range measured a ghost signal under an angle of incidence of 12° with respect to the principal toroidal orientation. The camera construction is being based on plain stainless steel plates and due to the housing geometry it is possible that incident radiation is reflected and reaches the detector. Thus, it is no longer

guaranteed that each channel measures the radiation only along its designated orientation which leads to not acceptable errors of the derivation of the total radiated power. To improve the cameras, all affected housings are now being modified with grooved surface plates clamped on the inside wall of the camera housing with the aim to diffuse and scatter back radiation from unwanted angles of incidence.

As a result of this work, IBOROB is currently being operated as a standard measurement device at IPP assessing each development step or modification of the ITER prototype camera. The assessment of a bolometer camera intended to be used in the stellarator fusion experiment W7-X is planned for the future. Moreover, the bolometer diagnostic in ASDEX Upgrade will be upgraded with a new collimator camera in the divertor region during the next vessel shutdown which would be another task for IBOROB to check if the design properties of this new camera correspond to the requirements.

**Challenges for the future development of the bolometer cameras**

In this work, the optical properties of two ITER bolometer camera prototypes (Model '11 and '12) have been examined. From these outcomes, a new camera prototype was designed (Model '13). Many optical properties of the bolometer cameras are now well understood and the interpretation and analysis of the transmission measurements with IBOROB has been pushed to the limits of what is feasible. However, camera configurations with a narrow viewing cone still have room for improvement concerning the stray light reduction. The final objective would be to obtain a camera with stray light near the noise limit of the diagnostic, a few percent above would also be acceptable. But IBOROB's main task is to evaluate the current state of the camera. The separation and localization of the individual internal optical effects between the camera components is complex and time demanding. Multiple measurements have to be compared with each other to determine the internal sequence of the reflections in the camera. Moreover, it has to be taken into account that the manufacturing and modification of several prototypes is costly.

Therefore, as a proposal for future studies and in order to gain more knowledge about the transmission characteristic of the bolometer cameras which can not be assessed with IBOROB, it would be advisable to perform optical simulations of the transmission measurements with Monte Carlo ray tracing (MCRT) based methods. All simulations have the inherent disadvantage that they strongly depend on the boundary conditions, such as the optical absorption and scattering properties of the camera housing and aperture material.

Here, the results from IBOROB are essential to estimate these parameters by comparing MCRT calculations with corresponding transmission measurements. Once a certain parameter range has been deduced, further modification of the camera design parameters can be performed in order to calculate an optimized configuration. For instance, it could be calculated how much power each aperture is absorbing in the collimator in order to indicate its importance in the camera. Finally, a theoretical model of the camera could be developed allowing the optimization

of the transmission with respect to each camera component. In the end, both approaches, MCRT simulations and the measurements with IBOROB, would efficiently complement each other.

# List of Figures

# List of Tables

# List of Abbreviations

| | |
|---|---|
| AFS | Andrew File System |
| ASDEX | AxialSymmetrisches Divertor-EXperiment |
| AXUV | Absolute eXtreme UltraViolet |
| BM | Blanket Module |
| BRDF | Bidirectional Reflectance Distribution Function |
| BSDF | Bidirectional Scattering Distribution Function |
| CAD | Computer Aided Design |
| CDRH | Center for Devices and Radiological Health |
| CMM | Coordinate Measurement Machine |
| CNC | Computerized Numerical Control |
| CODAC | Control, Data Access and Communication |
| CS | Coordinate System |
| CXRS | Charge Exchange Recombination Spectroscopy |
| DAQ | Data AcQuisition |
| DC | Direct Current |
| DCB | Divertor Cassette Body |
| DEMO | DEMOnstration Power Plant |
| DLR | Deutsches Zentrum für Luft- und Raumfahrt |
| DMA | Direct Memory Access |
| DT | Deuterium Tritium |
| ECRH | Electron Cyclotron Resonance Heating |
| EDM | Electric Discharge Machining |
| ELM | Edge Localized Modes |
| EM | Electro Magnetic |
| EPP | Equatorial Port Plug |

| | |
|---|---|
| EU | European Union |
| F4E | Fusion 4 Energy |
| FPA | Framework Partnership Agreement |
| FPGA | Field Programmable Gate Array |
| FRI | Fast Research Interface |
| FWHM | Full Width Half Maximum |
| FW | First Wall |
| IBOROB | ITer Bolometer Robot test rig |
| ICRH | Ion Cyclotron Resonance Heating |
| ILW | ITER-Like Wall |
| IPP | Max Planck Institut füer Plasmaphysik |
| IR | InfraRed |
| IRVB | Infrared Imaging Video Bolometer |
| IVVS | In Vessel Viewing System |
| JET | Joint European Torus |
| KCP | KUKA Control Panel |
| KRC | KUKA Robot Controller |
| KRL | KUKA Robot Language |
| KUKA | Keller und Knappich Augsburg (*German robot company*) |
| LabVIEW | LABoratory Virtual Instrument Engineering Workbench |
| LHD | Large Helical Device |
| LOS | Line Of Sight(s) |
| LSO | Laser Safety Officer |
| LVD | Low Voltage Directive |
| LWR | Light Weight Robot |
| MATLAB | Matrix Laboratory |
| MCRT | Monte Carlo Ray Tracing |
| MPE | Maximum Permissible Exposure |
| NBI | Neutron Beam Injection |
| NIR | Near-Infrared |
| OPA | Optical Parametric Oscillator |
| PCS | Plasma Control System |
| PFC | Plasma Facing Component |

| | |
|---|---|
| PLC | Programmable Logic Controller |
| PTP REL | Point to Point RELative movements |
| PTP | Point to Point |
| RAFM | Reduced Activation Ferritic/Martensitic |
| RC | Resistor-Capacitor |
| RH | Remote Handling |
| SCADA | Supervisory Control And Data Acquisition |
| S/N | Signal to Noise (ratio) |
| SPS | SpeicherProgrammierbare Steuerung |
| TCP/IP | Transmission Control Protocol / Internet Protocol |
| TCP | Tool Center Point |
| TCS | Torus Coordinate System |
| TEM | Transverse Electromagnetic Mode |
| TZM | Molybdenum-Titanium-Zirconium (*in order of material proportion*) |
| UV | UltraViolet |
| VHDL | Very High speed integrated circuit hardware Description Language |
| VNC | Vertical Neutron Camera |
| VS | Vertical Stability |
| VV | Vacuum Vessel |

# Glossary

| | |
|---|---|
| $Q$ | Ratio of produced fusion power to the net input power |
| $R_{1-4}$ | Wheatstone bridge resistors 1-4 |
| $P_{rad}$ | Radiated power on the bolometer detector |
| $\kappa_{heat}$ | Heat capacity of the bolometer detector |
| $U_{bolo}$ | Bolometer bridge voltage |
| $\tau_{detc}$ | Cooling time constant of bolometer detector |
| $T_{abs,nominal}$ | Detector foil thickness, absolute and nominal value |
| $P_{calib}$ | Power used for detector foil calibration |
| $P_{\Omega-heat}$ | Ohmic heating power during measurement |
| $U_{src}$ | AC source voltage of bolometer DAQ |
| $\omega_{src}$ | Frequency of the source voltage of bolometer DAQ |
| $R_{md}$ | Meander resistance |
| $R_{cab}$ | Resistance of the cables connecting the DAQ |
| $C_{cab}$ | Capacity of the cables connecting the DAQ |
| $g(x,y)$ | Two dimensionsal radiation profile |
| $K(\theta,\xi)$ | Two dimensionsal transmission function |
| $\xi$ | Angle in the vertical plane (poloidal orientation) |
| $\theta$ | Angle in the horizontal plane (toroidal orientation) |
| $I_D(\xi,\theta)$ | Detected intensity in toroidal and poloidal plane |
| $l_\theta(\theta), l_\xi(\xi)$ | Illuminated components of the detector in toroidal and poloidal plane |
| $L_C$ | Collimator length |
| $L_D$ | Distance between detector plane and aperture exit |

| | |
|---|---|
| $y_D^+, y_D^-$ | Y-Positions (poloidal orientation) of the aperture edges (exit) |
| $y_P^+, y_P^-$ | Y-Positions (poloidal orientation) of the aperture edges (entrance) |
| $\alpha_{1-4}$ | Critical angles of theoretical transmission function in poloidal orientation |
| $z_D^+, z_D^-$ | Z-Positions (toroidal orientation) of the aperture edges (exit) |
| $z_{P,i}^-, z_{P,i}^+$ | Z-Positions (toroidal orientation) of the aperture edges (entrance) |
| $\beta_{1-4}$ | Critical angles of theoretical transmission function in toroidal orientation |
| $N_t$ | Number of subcollimators in aperture or top plate |
| $d_p$ | Poloidal aperture opening of top plate |
| $d_t$ | Toroidal aperture opening of top plate |
| $\Delta\theta_{max,FWHM}$ | Maximum and FWHM width of LOS in toroidal orientation |
| $\Delta\xi_{max,FWHM}$ | Maximum and FWHM width of LOS in poloidal orientation |
| $\xi_{max}, \theta_{max}$ | Poloidal and toroidal center and maximum of LOS |
| $\varnothing_{las-in}, \varnothing_{las-out}$ | Laser beam width at the entrance and at the exit of the beam expander |
| $T_{FRI,ImgLab,DAQ}$ | FRI, ImagingLab and DAQ sample time |
| $\delta_\xi, \delta_\theta$ | Robot step size in poloidal and toroidal orientation |
| $\Delta\xi, \Delta\theta$ | Poloidal and toroidal scan width |
| $\Delta_{calib}(A-G)$ | Angular calibration error of laser and beam expander |
| $\varnothing_{calib}(A-G)$ | Diameter of projected circle during laser and beam expander calibration |
| $\Delta_{calib}$ | Angular uncertainty of laser and beam expander after the calibration |
| $D_{calib}$ | Distance during laser and beam expander calibration |
| $t_0, t_e$ | Start time and end time during a measurement |
| $\sigma(\xi/\theta)$ | Measurement uncertainty in poloidal and toroidal orientation |
| $\Delta_{focus}$ | Angular uncertainty between focused and unfocused laser |
| $\Delta_{robot}$ | Angular uncertainty of robot alignment |
| $\Delta_{Faro-(Lab,AUG)}$ | Angular uncertainty of FaroArm measurements |
| $\Delta_{AUG}$ | Total angular uncertainty during ASDEX Upgrade measurements |
| $\xi_{CAD}, \xi_{MEA}$ | Poloidal orientation of LOS, theoretical value and measured value |
| $\theta_{CAD}, \theta_{MEA}$ | Toroidal orientation of LOS, theoretical value and measured value |
| $W_{channel}$ | Distance between the channel walls in the collimator Model '12 |

$\varnothing_{1-5}$          Different laser beam diameters

$\Delta_{tor}$          Toroidal beam shift with respect to the aperture center

$\Delta\Phi_{sectors}$          Toroidal angle range of each sector in ASDEX Upgrade

$\xi_{start}, \xi_{end}$          Poloidal start and end angles for IBOROB

$W_{LOS}$          Integrated (scalar) transmission value of a LOS

$\theta_{error}^{min}, \theta_{error}^{max}$          Minimum and maximum error of LOS alignment

$Et_{CAD,MEA}$          Etendue, theoretical value and measured value

# Bibliography

[1] United Nations, "World population prospects: The 2012 revision", *Press Release from the 13th June 2013*.

[2] U.S. Energy Information Administration, "International energy outlook 2013 with projections to 2040, Report Number: DOE/EIA-0484", tech. rep., 2013.

[3] B. N. Kolbasov, L. El-Guebaly, V. I. Khripunov, Y. Someya, K. Tobita, and M. Zucchetti, "Some technological problems of fusion materials management", *Fusion Engineering and Design, published and available online*, 2014.

[4] H. Tanigawa, Y. Someya, H. Sakasegawa, T. Hirose, and K. Ochiai, "Radiological assessment of the limits and potential of reduced activation ferritic/martensitic steels", *Fusion Engineering and Design, published and available online*, 2014.

[5] A. Bradshaw, T. Hamacher, and U. Fischer, "Is nuclear fusion a sustainable energy form?", *Fusion Engineering and Design*, vol. 86, no. 9, pp. 2770–2773, 2011.

[6] A. Bradshaw and T. Hamacher, "Nuclear fusion and the helium supply problem", *Fusion Engineering and Design*, vol. 88, no. 9, pp. 2694–2697, 2013.

[7] H. A. Bethe, "Energy production in stars", *Physical Review*, vol. 55, no. 434, 1939.

[8] J. Wesson and D. J. Campbell, *Tokamaks*. Clarendon Press, 2004.

[9] F. Jenko, "State-of-the-art turbulence simulations for fusion and astrophysical plasmas with GENE", *SuperMUC Review Workshop 8-9 July 2014, Max Planck Institute for Plasma Physics, University of Ulm*, 2014.

[10] E. I. Moses, "Advances in inertial confinement fusion at the National Ignition Facility (NIF)", *Fusion Engineering and Design, Proceedings of the Ninth International Symposium on Fusion Nuclear Technology*, vol. 85, no. 7-9, pp. 983–986, 2010.

[11] H. Zohm, *Plasmaphysik - Vorlesung an der LMU München*. LMU, 2009.

[12] A. Kaye and the JET Team, "Results of recent deuterium-tritium experiments in JET", *JET–P(98)37*, 1998.

[13] J. Wesson, "The science of JET", *European Fusion Development Agreement*, 2000.

[14] F. Wagner, G. Becker, K. Behringer, D. Campbell, A. Eberhagen, W. Engelhardt, G. Fussmann, O. Gehre, J. Gernhardt, G. v. Gierke, G. Haas, M. Huang, F. Karger, M. Keilhacker, O. Klüber, M. Kornherr, K. Lackner, G. Lisitano, G. G. Lister, H. M. Mayer, D. Meisel, E. R. Müller, H. Murmann, H. Niedermeyer, W. Poschenrieder, H. Rapp, H. Röhr, F. Schneider, G. Siller, E. Speth, A. Stäbler, K. H. Steuer, G. Venus, O. Vollmer, and Z. Yü, "Regime of improved confinement and high beta in neutral-beam-heated divertor discharges of the ASDEX tokamak", *Physical Review Letters*, vol. 49, pp. 1408–1412, 1982.

[15] A. Costley, T. Sugie, G. Vayakis, and C. Walker, "Technological challenges of ITER diagnostics", *Fusion Engineering and Design*, vol. 74, no. 1, pp. 109–119, 2005.

[16] J. Snipes, D. Beltran, T. Casper, Y. Gribov, A. Isayama, J. Lister, S. Simrock, G. Vayakis, A. Winter, and Y. Yang, "Actuator and diagnostic requirements of the ITER plasma control system", *Fusion Engineering and Design*, vol. 87, no. 12, pp. 1900–1906, 2012.

[17] A. E. Costley, "Towards diagnostics for a fusion reactor", *IEEE Transactions on Plasma Science*, vol. 38, no. 10, pp. 2934–2943, 2010.

[18] A. Suarez, R. Reichle, M. Loughlin, E. Polunovskiy, and M. Walsh, "Neutronic analysis for bolometers in ITER", *Fusion Engineering and Design*, vol. 88, no. 6, pp. 1395–1399, 2013.

[19] R. Pampin, A. Davis, J. Izquierdo, D. Leichtle, M. Loughlin, J. Sanz, A. Turner, R. Villari, and P. Wilson, "Developments and needs in nuclear analysis of fusion technology", *Fusion Engineering and Design*, vol. 88, no. 6-8, pp. 454–460, 2013.

[20] V. Barabash, A. Peacock, S. Fabritsiev, G. Kalinin, S. Zinkle, A. Rowcliffe, J.-W. Rensman, A. Tavassoli, P. Marmy, and P. Karditsas, "Materials challenges for ITER - current status and future activities", *Journal of Nuclear Materials*, vol. 367, pp. 21–32, 2007.

[21] F. Genco and A. Hassanein, "Simulation of damage to tokamaks plasma facing components during intense abnormal power deposition", *Fusion Engineering and Design*, vol. 89, no. 4, pp. 335–341, 2014.

[22] R. Reichle, T. Nishitani, E. Hodgson, L. Ingesson, E. Ishitsuka, S. Kasai, K. Mast, T. Shikama, J. Vallet, and S. Yamamoto, "Radiation hardness test of mica bolometers for ITER in JMTR", *Advanced Diagnostics for Magnetic and Inertial Fusion, Springer*, pp. 295–298, 2002.

[23] S. Salasca, B. Cantone, A. Grosman, B. Esposito, F. Moro, D. Morocco, R. Villari, M. Angelone, E. Rincon, and C. Hidalgo, "Results of an integration study of a diagnostics port plug in ITER", *Fusion Engineering and Design*, vol. 88, no. 6, pp. 602–606, 2013.

[24] C. Walker, A. Costley, K. Itami, T. Kondoh, T. Sugie, G. Vayakis, and A. Malaquias, "ITER diagnostics: Integration and engineering aspects", *Review of Scientific Instruments*, vol. 75, no. 10, pp. 4243–4246, 2004.

[25] B. Eren, L. Marot, I. Ryzhkov, S. Lindig, A. Houben, M. Wisse, O. Skoryk, M. Oberkofler, V. Voitsenya, C. Linsmeier, and E. Meyer, "Roughening and reflection performance of molybdenum coatings exposed to a high-flux deuterium plasma", *Nuclear Fusion*, vol. 53, no. 11, p. 113013, 2013.

[26] S. Zinkle, J. Blanchard, R. Callis, C. Kessel, R. Kurtz, P. Lee, K. McCarthy, N. Morley, F. Najmabadi, R. Nygren, G. Tynan, D. Whyte, R. Willms, and B. Wirth, "Fusion materials science and technology research opportunities now and during the ITER era", *Fusion Engineering and Design, published and available online*, 2014.

[27] C. Damiani, M. Irving, and L. Semeraro, "The European contribution to the procurement of the ITER remote handling systems", *Fusion Engineering and Design*, vol. 84, no. 2-6, pp. 646–650, 2009.

[28] J. Snipes, Y. Gribov, and A. Winter, "Physics requirements for the ITER plasma control system", *Fusion Engineering and Design*, vol. 85, no. 3, pp. 461–465, 2010.

[29] A. Costley, "Key issues in ITER diagnostics: Problems and solutions", *Review of Scientific Instruments*, vol. 70, no. 1, pp. 391–396, 1999.

[30] A. E. Costley, "Measurement requirements and the diagnostic system on ITER", *Proceedings of 18th IAEA Conference*, vol. IAEA-CN-77, no. ITERP/09, 2000.

[31] E. Viezzer, *Radial electric field studies in the plasma edge of ASDEX Upgrade*. PhD thesis, Ludwig-Maximilians-Universität München, 2012.

[32] C. Vorpahl, W. Suttrop, M. Ebner, B. Streibl, and H. Zohm, "Deformation measurement of internal components of ASDEX Upgrade using optical strain sensors", *Fusion Engineering and Design*, vol. 88, no. 6, pp. 537–540, 2013.

[33] E. Müller and F. Mast, "A new metal resistor bolometer for measuring vacuum ultraviolet and soft x radiation", *Journal of Applied Physics*, vol. 55, no. 7, pp. 2635–2641, 1984.

[34] K. Mast and R. Müller, "Patent: Strahlungsmessgerät, DE 3408724 C2", 1988.

[35] European Joint Undertaking for ITER and the Development of Fusion Energy ('Fusion for Energy'), "Action plan for the framework partnership agreement (FPA) for diagnostic development and design: Bolometers", 2012.

[36] H. Meister, M. Kannamüller, J. Koll, A. Pathak, F. Penzel, T. Trautmann, P. Detemple, S. Schmitt, and H. Langer, "Reliability issues for a bolometer detector for ITER at high operating temperatures", *Review of Scientific Instruments*, vol. 83, no. 10, p. 10D724, 2012.

[37] M. Merola, D. Loesser, A. Martin, and P. Chappuis, "ITER plasma-facing components", *Fusion Engineering and Design*, vol. 85, pp. 2312–2322, 2010.

[38] S. Kálvin, "Performance analysis and line-of-sight optimization of the ITER bolometer diagnostic", *EFDA Report - Contract 06-1447*, 2007.

[39] A. Encheva, L. Bertalot, B. Macklin, G. Vayakis, and C.Walker, "Integration of ITER in-vessel diagnostic components in the vacuum vessel", *Fusion Engineering and Design*, vol. 84, pp. 736–747, 2009.

[40] P. Lotte, M. H. Aumeunier, P. Devynck, C. Fenzi, V. Martin, and J. M. Travelere, "Wall reflection issues for optical diagnostics in fusion devices", *Review of Scientific Instruments*, vol. 81, no. 10, p. 10E120, 2010.

[41] R. Reichle, P. Andrew, G. Counsell, J.-M. Drevon, A. Encheva, G. Janeschitz, D. Johnson, Y. Kusama, B. Levesy, and A. Martin, "Defining the infrared systems for ITER", *Review of Scientific Instruments*, vol. 81, no. 10, pp. 10E135–10E135, 2010.

[42] C. D. Walcott, *Biographical Memoir of Samuel Pierpont Langley.* National Academy Of Sciences, 1911.

[43] J. M. Gildemeister, A. T. Lee, and P. L. Richards, "A fully lithographed voltage-biased superconducting spiderweb bolometer", *Applied Physics Letters*, vol. 74, no. 6, pp. 868–870, 1999.

[44] R. B. Spielman, C. Deeney, D. L. Feh, D. L. Hanson, N. R. Keltner, J. S. McGurn, and J. L. McKenney, "Fast resistive bolometry", *Review of Scientific Instruments*, vol. 70, no. 1, pp. 651–655, 1999.

[45] L. Giannone, K. Mast, and M. Schubert, "Derivation of bolometer equations relevant to operation in fusion experiments", *Review of Scientific Instruments*, vol. 73, no. 9, pp. 3205–3214, 2002.

[46] H. Hsuan, K. Bol, and R. Ellis, "Measurement of the energy balance in ATC tokamak", *Nuclear Fusion*, vol. 15, no. 4, pp. 657–661, 1975.

[47] M. Di Maio, R. Reichle, and R. Giannella, "Design of a ferroelectric bolometer", *Fusion Engineering, 17th IEEE/NPSS Symposium*, vol. 2, pp. 775–778, 1997.

[48] E. Iborra, A. Sanz-Hervás, and T. Rodriguez, "A new design of a semiconductor bolometer on rigid substrate for fusion plasma diagnostics", *Review of Scientific Instruments*, vol. 64, no. 7, pp. 1714–1717, 1993.

[49] P. Stott, D. Akulina, G. Leotta, E. Sindoni, and C. Wharton, eds., *Diagnostics for Fusion Reactor Conditions.* Commission of the European Communities, Pergamon Press, 1982.

[50] K. Mast, H. Krause, K. Behringer, A. Bulliard, and G. Magyar, "Bolometric diagnostics in JET", *Review of Scientific Instruments*, vol. 56, no. 5, pp. 969–971, 1985.

[51] K. Mast, J. Vallet, C. Andelfinger, P. Betzler, H. Kraus, and G. Schramm, "A low noise highly integrated bolometer array for absolute measurement of VUV and soft x radiation", *Review of Scientific Instruments*, vol. 62, no. 3, pp. 744–750, 1991.

[52] M. Reinke and I. Hutchinson, "Two dimensional radiated power diagnostics on Alcator C-Mod", *Review of Scientific Instruments*, vol. 79, no. 10, pp. 10F306–10F306, 2008.

[53] B. J. Youngblood, "Bolometer diagnostics on Alcator C-Mod", Master's thesis, MIT, 2004.

[54] B. J. Peterson, A. Y. Kostrioukov, N. Ashikawa, Y. Liu, Y. Xu, M. Osakabe, K. Watanabe, T. Shimozuma, and S. Sudo, "Bolometer diagnostics for one- and two-dimensional measurements of radiated power on the Large Helical Device", *Plasma Physics and Controlled Fusion*, vol. 45, no. 7, p. 1167, 2003.

[55] M. Bernert, *Analysis of the H-mode densitylimit and fast edge phenomena with AXUV bolometry.* PhD thesis, Ludwig-Maximilians-Universität München, 2013.

[56] J. C. Ingraham, "Infrared calorimeter for time-resolved plasma energy flux measurement", *Review of Scientific Instruments*, vol. 54, no. 6, pp. 673–676, 1983.

[57] G. Wurden, "A radiation-hard, steady state, digital imaging bolometer system", *Fusion Engineering and Design*, vol. 34, pp. 301–305, 1997.

[58] G. Wurden and B. Peterson, "Development of imaging bolometers for long-pulse MFE experiments", *Review of Scientific Instruments*, vol. 70, no. 1, pp. 255–259, 1999.

[59] S. N. Pandya, B. J. Peterson, R. Sano, K. Mukai, E. A. Drapiko, A. G. Alekseyev, T. Akiyama, M. Itomi, and T. Watanabe, "Calibration of a thin metal foil for infrared imaging video bolometer to estimate the spatial variation of thermal diffusivity using a photo-thermal technique", *Review of Scientific Instruments*, vol. 85, no. 5, pp. 54902–54909, 2014.

[60] H. Meister, L. Giannone, L. D. Horton, G. Raupp, W. Zeidner, G. Grunda, S. Kalvin, U. Fischer, A. Serikov, S. Stickel, and R. Reichle, "The ITER bolometer diagnostic: Status and plans", *Review of Scientific Instruments*, vol. 79, no. 10, p. 10F511, 2008.

[61] B. J. Peterson, H. Parchamy, N. Ashikawa, H. Kawashima, S. Konoshima, A. Y. Kostryukov, I. V. Miroshnikov, D. Seo, and T. Omori, "Development of imaging bolometers for magnetic fusion reactors", *Review of Scientific Instruments*, vol. 79, no. 10, p. 10E301, 2008.

[62] Univ.-Prof. Dr.-Ing. Alexander W. Koch, "Messsystem- und Sensortechnik", *Faschschaft Elektro- und Informationstechnik e.V.*, 2005.

[63] T. Nishitani, T. Shikama, R. Reichle, E. Hodgson, E. Ishitsuka, S. Kasai, and S. Ya-mamoto, "In-situ irradiation test of mica substrate bolometer at the JMTR reactor for the ITER diagnostics", *Fusion Engineering and Design*, vol. 63-64, pp. 437–441, 2002.

[64] K. McCormick, A. Huber, C. Ingesson, F. Mast, J. Fink, W. Zeidner, A. Guigon, and S. Sanders, "New bolometry cameras for the JET enhanced performance phase", *Fusion Engineering and Design*, vol. 74, pp. 679–683, 2005.

[65] D. Seo, B. Peterson, and S. H. Lee, "First results of the resistive bolometers on KSTAR", *Review of Scientific Instruments*, vol. 81, no. 10, pp. 10E128–10E128, 2010.

[66] Y. Duan, L. Hu, S. Mao, K. Chen, S. Lin, and E. D. Team, "The resistive bolometer for radiated power measurement on EAST", *Review of Scientific Instruments*, vol. 83, no. 9, pp. 93501–93501, 2012.

[67] D. Zhang, L. Giannone, B. Klein, and the W7-X-Team, "The bolometry concept for the W7-X Stellarator", *34th EPS Conference on Plasma Phys. Warsaw, 2 - 6*, vol. ECA Vol.31F, no. P-5.111, 2007.

[68] H. Meister and S. Schmitt, "Entwicklung und Test von Prototypkomponenten für die ITER Bolometerdiagnostik - Schlussbericht", tech. rep., Max-Planck-Institut für Plasma-physik, IPP-Report Nr: 4/292, 2014.

[69] L. Giannone, T. Eich, J. Fuchs, M. Ravindran, Q. Ruan, L. Wenzel, M. Cerna, and S. Concezzi, "Data acquisition and real-time bolometer tomography using LabVIEW RT", *Fusion Engineering and Design*, vol. 86, no. 6, pp. 1129–1132, 2011.

[70] D. Zhang, R. Burhenn, R. Koenig, L. Giannone, P. Grodzki, B. Klein, K. Grosser, J. Baldzuhn, K. Ewert, and V. Erckmann, "Design criteria of the bolometer diagnos-tic for steady-state operation of the W7-X stellarator", *Review of Scientific Instruments*, vol. 81, no. 10, pp. 10E134–10E134, 2010.

[71] D. Zhang, H. M. Gianonne, R. König, and R. Burhenn, "Thermal drift study on the bolometer diagositc for staeady-state fusion plasmas", *39th EPS Conference on Plasma Physics and 16th International Congress on Plasma Physics*, no. P5.040, 2012.

[72] D. Zhang, L. Giannone, O. Grulke, M. Piechotka, T. Windisch, A. Stark, and T. Klinger, "Investigation of the neutral gas pressure effect on the metal resistive bolometer", *Interna-tional Conference on Research and Applications of Plasmas*, vol. 993, no. 1, pp. 199–202, 2008.

[73] P. Carvalho, H. Thomsen, R. Coelho, P. Duarte, C. Silva, and H. Fernandes, "ISTTOK plasma control with the tomography diagnostic", *Fusion Engineering and Design*, vol. 85, no. 2, pp. 266–271, 2010.

[74] K. Tahiliani and R. Jha, "Bolometers for fusion plasma diagnostics", *InTech*, 2012.

[75] U. Wenzel, A. Thoma, R. Dux, C. Fuchs, A. Herrmann, S. Hirsch, A. Kallenbach, H. Kastelewicz, M. Laux, F. Mast, and B. Napiontek, "Spatial radiation profiles in the ASDEX Upgrade divertor for detached plasmas", *Journal of Nuclear Materials*, vol. 241 - 243, no. 0, pp. 728–733, 1997.

[76] A. Murari, T. Edlington, J. Brzozowski, E. de La Luna, P. Andrew, G. Arnoux, F. Cecil, L. Cupido, D. Darrow, and V. Kiptily, "JET new diagnostic capability on the route to ITER", *Fusion Engineering and Design*, vol. 82, no. 5, pp. 1161–1166, 2007.

[77] J. Fuchs, T. Eich, A. Herrmann, K. T. Mast, and ASDEX Upgrade Team, "Radiation distribution and energy balance during type-I ELMs in ASDEX Upgrade", *Journal of Nuclear Materials*, vol. 337, pp. 756–760, 2005.

[78] T. Eich, A. Herrmann, G. Pautasso, P. Andrew, N. Asakura, J. Boedo, Y. Corre, M. Fenstermacher, J. Fuchs, and W. Fundamenski, "Power deposition onto plasma facing components in poloidal divertor tokamaks during type-I ELMs and disruptions", *Journal of Nuclear Materials*, vol. 337, pp. 669–676, 2005.

[79] P. B. Snyder, H. R. Wilson, and X. Q. Xu, "Progress in the peeling-ballooning model of edge localized modes: Numerical studies of nonlinear dynamics", *Physics of Plasmas*, vol. 12, no. 5, p. 056115, 2005.

[80] A. Huber, R. Pitts, A. Loarte, V. Philipps, P. Andrew, S. Brezinsek, J. Coad, T. Eich, J. Fuchs, W. Fundamenski, S. Jachmich, G. Matthews, K. McCormick, P. Mertens, J. Rapp, G. Sergienko, and M. Stamp, "Plasma radiation distribution and radiation loads onto the vessel during transient events in JET", *Journal of Nuclear Materials*, vol. 390 - 391, no. 0, pp. 830–834, 2009.

[81] G. Arnoux, B. Bazylev, M. Lehnen, A. Loarte, V. Riccardo, S. Bozhenkov, S. Devaux, T. Eich, W. Fundamenski, and T. Hender, "Heat load measurements on the JET first wall during disruptions", *Journal of Nuclear Materials*, vol. 415, no. 1, pp. 817–820, 2011.

[82] L. Ingesson, B. Alper, B. J. Peterson, and J.-C. Vallet, "Tomography diagnostics: Bolometry and soft-x-ray detection", *Fusion Science and Technology*, vol. 53, no. 2, pp. 528–576, 2007.

[83] L. C. Ingesson and D. J. Wilson, "Optimization of aperture and collimators for multi-channel plasma diagnostics", *Review of Scientific Instruments*, vol. 73/8, pp. 2890–2899, 2002.

[84] C. Fuchs, K. F. Mast, A. Herrmann, K. Lackner, and ASDEX Upgrade Team, "Twodimensional reconstruction of the radiation power density in ASDEX Upgrade.", *Europhysics Conference Abstracts, Proceedings of the 21th EPS Conference on Controlled Fusion and Plasma Physics*, vol. 18B:1308–1311, 1994.

[85] M. Bernert, T. Eich, A. Burckhart, J. C. Fuchs, L. Giannone, A. Kallenbach, R. M. McDermott, and B. Sieglin, "Application of AXUV diode detectors at ASDEX Upgrade", *Review of Scientific Instruments*, vol. 85, no. 3, p. 033503, 2014.

[86] D. Zhang, H. Thomsen, S. Bozhenkov, T. Bräuer, H. Greve, P. Grodzki, H. Jenzsch, R. König, M. Otte, and T. Pedersen, "Optimization of lines of sight for tomographic reconstruction of the bolometer diagnostic at the W7-X Stellarator", *40th EPS Conference on Plasma Physics*, vol. ECA Vol. 37D, no. P5.121, 2013.

[87] L. C. Ingesson, P. J. Böcker, R. Reichle, M. Romanelli, and P. Smeulders, "Projection-space methods to take into account finite beam-width effects in two-dimensional tomography algorithms", *Journal of the Optical Society of America*, vol. 16, no. 1, pp. 17–27, 1999.

[88] R. Pasqualotto, M. Agostini, M. Brombin, R. Delogu, N. Fonnesu, L. Lotto, F. Molon, C. Piron, G. Serianni, and C. Taliercio, "Design of a visible tomography diagnostic for negative ion RF source SPIDER", *Fusion Engineering and Design*, vol. 88, no. 6, pp. 1253–1256, 2013.

[89] L. C. Ingesson and R. Reichle, "Lines of sight for ITER bolometers", *JET-R(98)03*, 1998.

[90] L. C. Ingesson, C. F. Maggi, and R. Reichle, "Characterization of geometrical detection-system properties for two-dimensional tomography", *Review of Scientific Instruments*, vol. 71, no. 3, pp. 1370–1378, 2000.

[91] H. Meister and S. Kalvin, "Optimisation of design parameters for bolometer cameras". submitted to Fusion Engineering and Design, 2014.

[92] H. Meister, F. Penzel, L. Giannone, M. Kannamüller, A. Kling, J. Koll, and T. Trautmann, "Development of an automated method for in situ measurement of the geometrical properties of the ITER bolometer diagnostic", *Fusion Engineering and Design, Proceedings of the 26th Symposium of Fusion Technology (SOFT-26)*, vol. 86, no. 6–8, pp. 1170–1173, 2011.

[93] L. Tunna, P. Barclay, R. Cernik, K. Khor, W. O'Neill, and P. Seller, "The manufacture of a very high precision x-ray collimator array for rapid tomographic energy dispersive diffraction imaging (TEDDI)", *Measurement Science and Technology*, vol. 17, no. 7, p. 1767, 2006.

[94] M. F. Smith, S. Majewski, and A. G. Weisenberger, "Optimizing pinhole and parallel hole collimation for scintimammography with compact pixellated detectors", *IEEE Transactions on Nuclear Science*, vol. 50, no. 3, pp. 321–326, 2003.

[95] C. Bai, L. Shao, J. Ye, M. Durbin, and M. Petrillo, "Hybrid parallel-slant hole collimators for SPECT imaging", *IEEE Transactions on Nuclear Science*, vol. 51, no. 3, pp. 619–624, 2004.

[96] A. Huber, K. McCormick, P. Andrew, and P. Beaumont, "Upgraded bolometer system on JET for improved radiation measurements", *Fusion Engineering and Design*, vol. 8, pp. 1327–1334, 2007.

[97] B. Reiter, *Radiative Response on Massive Noble Gas Injection For Runaway Suppression in Disruptive Plasmas*. PhD thesis, Ludwig-Maximilians-Universität München, 2010.

[98] R. Reichle, J. Fuchs, R. Giannella, N. Gottardi, H. Jaeckel, K. Mast, P. Thomas, and P. Van Belle, *Bolometer for ITER*. Springer, 1995.

[99] M. González and E. Hodgson, "Radiation resistant alternative substrates for ITER bolometers", *Fusion Engineering and Design*, vol. 66, pp. 881–885, 2003.

[100] T. Shikama, T. Nishitani, T. Kakuta, S. Yamamoto, S. Kasai, M. Narui, E. Hodgson, R. Reichle, B. Brichard, and A. Krassilinikov, "Irradiation test of diagnostic components for ITER application in the Japan Materials Testing Reactor", *Nuclear Fusion*, vol. 43, no. 7, pp. 517–521, 2003.

[101] A. Gusarov, S. Huysmansa, L. Vermeeren, E. R. Hodgson, and M. Decréton, "In situ in-reactor testing of potential bolometer materials for ITER plasma diagnostics", *Fusion Engineering and Design*, vol. 82, pp. 1179–1184, 2007.

[102] A. Gusarov, S. Huysmans, L. Giannone, and H. Meister, "Radiation stability of resistive bolometers intended for operation in the ITER environment", *Fusion Engineering and Design*, vol. 86, no. 6, pp. 1200–1203, 2011.

[103] A. Gusarov, S. Huysmans, M. Gonzalez, and E. Hodgson, "Radiation stability of prototype ITER-type resistive bolometers with improved electrical contacts", *Fusion Engineering and Design*, vol. 87, no. 1, pp. 61–66, 2012.

[104] L. Giannone, D. Queen, F. Hellman, and J. Fuchs, "Prototype of a radiation hard resistive bolometer for ITER", *Plasma Physics and Controlled Fusion*, vol. 47, no. 12, p. 2123, 2005.

[105] H. Meister, M. Willmeroth, D. Zhang, A. Gottwald, M. Krumrey, and F. Scholze, "Broadband efficiency calibration of ITER bolometer prototypes using Pt absorbers on SiN membranes", *Review of Scientific Instruments*, vol. 84, no. 12, pp. 123501–123501–7, 2013.

[106] A. Gusarov, S. Huysmans, M. Gonzalez, and E. Hodgson, "Radiation and temperature resistant electrical contacts for ITER diagnostic components", *Fusion Engineering and Design*, vol. 84, no. 2, pp. 864–866, 2009.

[107] A. Encheva, H. Omran, M. Pérez-Lasala, A. Alekseev, S. Arshad, O. Bede, S. Bender, L. Bertalot, M.-F. Direz, and J.-M. Drevon, "Challenges of ITER diagnostic electrical services", *Fusion Engineering and Design*, vol. 88, no. 6, pp. 1423–1427, 2013.

[108] F. Penzel, H. Meister, L. Giannone, M. Kannamüller, J. Koll, T. Trautmann, and A. W. Koch, "Assessment of line of sight characteristics of ITER bolometer prototype collimators", *Fusion Engineering and Design, Proceedings of the 27th Symposium of Fusion Technology (SOFT-27)*, vol. 88, no. 6-8, pp. 1267–1270, 2013.

[109] M. Joanny, J. Travere, S. Salasca, L. Marot, E. Meyer, C. Thellier, C. Cammarata, G. Gallay, and J. Ferme, "Achievements on engineering and manufacturing of ITER first-mirror mock-ups", *IEEE Transactions on Plasma Science*, vol. 40, no. 3, pp. 692–696, 2012.

[110] C. Liu, R. Nielsen, Y. Li, D. Ryding, and T. Kuzay, "Thermal outgassing studies on machinable tungsten and TZM molybdenum alloy", tech. rep., Argonne National Lab., 1994.

[111] H. Meister, W. Kasparek, D. Zhang, M. Hirsch, J. Koll, and A. Zeitler, "Millimetre wave attenuation of prototype diagnostic components for the ITER bolometers", *Fusion Engineering and Design, Proceedings of the 29th Symposium on Fusion Technology (SOFT-29)*, 2014.

[112] IMAGINGLAB Vision & Robotics, *Robotics Library for KUKA, Toolkit for Directly Commanding and Controlling KUKA Robotics from NI LabVIEW*, 2011.

[113] M. I. A. Lourakis and A. A. Argyros, "SBA: a software package for generic sparse bundle adjustment", *ACM Transactions on Mathematical Software*, pp. 1–30, 2009.

[114] T. Clarke and J. Fryer, "Handbook of practical camera calibration methods and models", *Photogrammetric Record*, vol. 16(91), pp. 51–66, 1999.

[115] Y. V. Filatov, M. Y. Agapov, M. N. Bournachev, D. P. Loukianov, and P. A. Pavlov, "Laser goniometer systems for dynamic calibration of optical encoders", *Optical Metrology, Proceedings SPIE 5144, Optical Measurement Systems for Industrial Inspection III*, pp. 381–390, 2003.

[116] E. Viezzer, T. Pütterich, R. Dux, A. Kallenbach, and the ASDEX Upgrade Team, "Investigation of passive edge emission in charge exchange spectra at the ASDEX Upgrade tokamak", *Plasma Physics and Controlled Fusion*, vol. 53, no. 3, p. 035002, 2011.

[117] V. Amosov, Y. Kashchuk, A. Krasilnikov, A. Kostin, A. Khovanskiy, A. Leonov, N. Rodionov, and R. Rodionov, "Implementation of vertical neutron camera (VNC) for ITER fusion plasma neutron source profile reconstruction", *World Academy of Science, Engineering and Technology*, vol. 7, no. 7, pp. 1236–1243, 2013.

[118] G. Naylor, R. Scannell, M. Beurskens, M. Walsh, I. Pastor, A. Donné, B. Snijders, W. Biel, B. Meszaros, and L. Giudicotti, "The ITER Thomson scattering core LIDAR diagnostic", *Journal of Instrumentation*, vol. 7, no. 03, p. C03043, 2012.

[119] Official Journal of the European Union, "Low voltage directive english directive 2006/95/ec", 2006.

[120] Vereinigung der Metall- und Berufsgenossenschaften, "Berufsgenossenschaftliche Informationen: BGI 534, Arbeiten in engen Räumen", 2008.

[121] FARO EUROPE GmbH Co. KG, "FaroArm® Manual - Includes Quantum, Platinum, Fusion and ScanArm® Models", 2010.

[122] T. Rajna, F. Herold, and C. Baylard, "Reverse engineering process of cryostat components of Wendelstein 7-X", *Fusion Engineering and Design, Proceeding of the 25th Symposium on Fusion Technology (SOFT-25)*, vol. 84, no. 7-11, pp. 1558–1561, 2009.

[123] H. Mönnich, D. Stein, J. Raczkowsky, and H. Wörn, "System for laser osteotomy in surgery with the KUKA lightweight robot – first experimental results", *World Congress on Medical Physics and Biomedical Engineering*, vol. 25, no. 6, pp. 179–182, 2009.

[124] G. Schreiber, A. Stemmer, and R. Bischoff, "The fast research interface for the KUKA lightweight robot", *IEEE Workshop on Innovative Robot Control Architectures for Demanding Research Applications (ICRA 2010)*, 2010.

[125] TOPTICA Photonics AG, *iBeam smart 640-S, Ultra-Compact Diode Laser*, 2010.

[126] Edmund Optics Inc., *NT55-579, 20x Complete Beam Expander*, 2010.

[127] M. Quigley, B. Gerkey, K. Conley, J. Faust, T. Foote, J. Leibs, E. Berger, R. Wheeler, and A. Ng, "ROS: an open-source robot operating system", *ICRA Workshop on Open Source Software*, 2009.

[128] M. Schopfer, F. Schmidt, M. Pardowitz, and H. Ritter, "Open source real-time control software for the KUKA light weight robot", *8th World Congress on Intelligent Control and Automation (WCICA)*, pp. 444–449, 2010.

[129] KUKA Roboter GmbH, "KUKA system software: Operating and programming instructions for system integrators", 2009.

[130] KUKA Roboter GmbH, "Operating instructions of KUKA system KR C2 lr controller", 2009.

[131] F. Penzel, "Realisierung eines Kalibrierprototypen mit rechnergestützter Steuerung und Automatisierung", *Diplomarbeit, TU München, Lehrstuhl für Messsystem- und Sensortechnik, IPP Report ID 478446*, 2010.

[132] KUKA Roboter GmbH, "Lightweight robot 4: Operating instructions", 2009.

[133] K. L. Conrad, P. S. Shiakolas, and T. C. Yih, "Robotic calibration issues: Accuracy, repeatability and calibration", *Proceedings of the 8th Mediterranean Conference on Control and Automation*, 2000.

[134] I. N. Bronstein, K. A. Semendjajew, G. Musiol, and H. Mühlig, *Taschenbuch der Mathematik*. Frankfurt am Main: Verlag Harri Deutsch, 4th ed., 1999.

[135] F. Valente, A. Vale, D. Fonte, and I. Ribeiro, "Optimized trajectories of the transfer cask system in ITER", *Fusion Engineering and Design*, vol. 86, no. 9, pp. 1967–1970, 2011.

[136] D. Fonte, *Motion Planning for a Rhombic-Like Vehicle Operating in ITER Scenarios*. PhD thesis, Instituto Superior Técnico, 2011.

[137] A. Rolfe, "Remote handling on fusion experiments", *Fusion Engineering and Design*, vol. 36, no. 1, pp. 91–100, 1997.

[138] L. Gargiulo, P. Bayetti, V. Bruno, J.-C. Hatchressian, C. Hernandez, M. Houry, D. Keller, J.-P. Martins, Y. Measson, and Y. Perrot, "Operation of an ITER relevant inspection robot on Tore Supra tokamak", *Fusion Engineering and Design*, vol. 84, no. 2, pp. 220–223, 2009.

[139] T. Mindham, G. Sandford, G. Hermon, C. Belcher, and N. Pace, "Developments in remote metrology at JET", *Fusion Engineering and Design*, vol. 86, no. 9, pp. 1855–1858, 2011.

[140] C. Neri, P. Costa, M. Ferri De Collibus, M. Florean, G. Mugnaini, M. Pillon, F. Pollastrone, and P. Rossi, "ITER in vessel viewing system design and assessment activities", *Fusion Engineering and Design*, vol. 86, no. 9, pp. 1954–1957, 2011.

# Acknowledgments

First and foremost, I would like to thank for my doctoral thesis supervisors Prof. Dr.-Ing. A.W. Koch and Prof. Dr.-Ing. U. Fantz for providing me the opportunity to pursue my dissertation at IPP. Furthermore, this thesis would not have been possible without the encouragement and help from my colleagues. There are several people with whom I am indebted for their contribution and help.

Thank you Dr. Hans Meister! Without you this dissertation would not have been possible. Thank you for giving me the opportunity to be part of this great research. Under your guidance, the work at IPP was always interesting, challenging and funny. You gave me the chance to finally become a scientist. Thank you!

Thank you Jürgen Koll, Thorsten Trautmann, Alexander Kling, Mario Kannamüller and Ahsray Pathak (Special thanks for the interesting cultural discussion about India and Germany) for your assistance in mechanical engineering and CATIA related questions. Additionally, I want to thank Alexander Sigalov and Dr. Louis Giannone for their unique assistance in LabVIEW. Big thanks for Till Sehmer. Apart from becoming a friend and office mate you helped us a lot in our research group and were indispensable during the ASDEX Upgrade measurements! I would also like to thank Dr. Matthias Bernert and Dr. Pascal de Marné for reviewing this thesis. A special acknowledgment goes to the complete ASDEX Upgrade Team for their assistance during the measurements in the vessel, especially from Stefan Eder, Wolfgang Zeidner and Gabi Fröhlich.

Finally, I would like to point out the remarkable job done by our students. It is thanks to their diligent work behind the scenes that we are much advanced than expected. Thank you Duc Hay Nguyen, Tuan Nam Le, Sonja Peters, Felician Mink, Anna Gavrilova, Mark Willmeroth, Jacopo Bonaccini.

Life is good :-)